UNIVERSIDADE FEDERAL DE MINAS GERAIS
Instituto de Geociências
Programa de Pós-Graduação em Geologia

Fernanda Moura Costa

CARACTERIZAÇÃO TRIDIMENSIONAL DA REGIÃO DO CAMPO DE BÚZIOS USANDO ANÁLISE MULTIATRIBUTOS SÍSMICOS E DADOS DE POÇOS REVELA IMPLICAÇÕES SOBRE SUA EVOLUÇÃO TECTONO-ESTRATIGRÁFICA

Belo Horizonte
2023

Fernanda Moura Costa

CARACTERIZAÇÃO TRIDIMENSIONAL DA REGIÃO DO CAMPO DE BÚZIOS USANDO ANÁLISE MULTIATRIBUTOS SÍSMICOS E DADOS DE POÇOS REVELA IMPLICAÇÕES SOBRE SUA EVOLUÇÃO TECTONO-ESTRATIGRÁFICA

Dissertação apresentada ao Programa de Pós-Graduação em Geologia da Universidade Federal de Minas Gerais como requisito parcial para obtenção do título de Mestra em Geologia.

Orientador(a): Prof(a). Dr(a). Aline Tavares Melo

Coorientador(a): Prof(a). Dr(a). Tiago Amâncio Novo

Belo Horizonte
2023

M929c
2023

Moura Costa, Fernanda.

Caracterização tridimensional da região do Campo de Búzios usando análise multiatributos sísmicos e dados de poços revela implicações sobre sua evolução tectono-estratigráfica [manuscrito] / Fernanda Moura Costa. – 2023.

142 f., enc. il. (principalmente color.)

Orientador: Tiago Amâncio Novo.

Dissertação (mestrado) – Universidade Federal de Minas Gerais, Instituto de Geociências, 2023.

Área de concentração: Geologia Econômica e Aplicada.

Bibliografia: f. 94-95.

Inclui apêndices e anexos.

1. Geologia estratigráfica – Teses. 2. Bacias sedimentares – Teses. 3. Campos petrolíferos – Teses. 4. Santos, Bacia de – Teses. I. Novo, Tiago Amâncio. II. Universidade Federal de Minas Gerais. Instituto de Geociências. III. Título.

CDU: 551.7(81)

Ficha catalográfica elaborada por Elisabete Quatrini Vieira – CRB-6/2210
Biblioteca "Vitória Pedersoli", Instituto de Geociências da UFMG

UNIVERSIDADE FEDERAL DE MINAS GERAIS

PROGRAMA DE PÓS-GRADUAÇÃO EM GEOLOGIA DO IGC-UFMG

FOLHA DE APROVAÇÃO

Caracterização Tridimensional da região do Campo de Búzios Usando Análise Multiatributos Sísmicos e Dados de Poços revela implicações sobre sua evolução tectono-estratigráfica

FERNANDA MOURA COSTA

Dissertação submetida à Banca Examinadora designada pelo Colegiado do Programa de Pós-Graduação em GEOLOGIA, como requisito para obtenção do grau de Mestre(a) em GEOLOGIA, área de concentração GEOLOGIA ECONÔMICA E APLICADA, pelo Programa de Pós-graduação em Geologia do Instituto de Geociências da Universidade Federal de Minas Gerais.

Aprovada em 26 de junho de 2023, pela banca constituída pelos membros:

Profa. Dra. Aline Tavares Melo – Orientadora
UFMG

Prof. Dr. Gabriel Jubé Uhlein
UFMG

Prof. Dr. Alexandre Uhlein
UFMG

Belo Horizonte, 26 de junho de 2023.

À minha mãe.

AGRADECIMENTOS

Primeiramente, gostaria de agradecer à minha orientadora Aline por mesmo do outro lado do planeta, sempre se fazer presente e ler cada palavra com toda atenção e dedicação do universo geológico, contribuindo sempre com ideias importantes.

Ao coorientador Tiago, por toda contribuição, tanto nas questões geológicas como emocionais, pelo apoio, confiança, disponibilidade e infinitas risadas.

Aos membros da banca Alexandre Uhlein e Gabriel Jubé, pela disposição em avaliar meu trabalho e pelas contribuições técnicas.

À minha mãe Ana Cláudia, pelo apoio e amor incondicional e por me proporcionar sempre as melhores condições de estudo e de vida durante toda a vida. Tudo que sou hoje derivou de você!

Ao meu padrasto Josias, por se interessar verdadeiramente pela minha pesquisa e por sempre trazer questionamentos, críticas e novidades do mundo do petróleo.

Aos colegas da SÍSMICA por todas as discussões e opiniões fundamentais para o desenvolvimento do trabalho.

À minha querida amiga e colega Lia, que além das inúmeras contribuições científicas, me proporcionou grande apoio emocional e muitas risadas.

Ao Tobias, pelas críticas, opiniões e conselhos muito construtivos que foram propulsoras para o andamento da pesquisa. Você foi um exímio coach científico!

Aos colegas e amigos Caique e Mari, pela ajuda e disposição durante o desenvolvimento desta dissertação.

Aos demais colegas da LINHA SÍSMICA por todas as discussões e opiniões fundamentais para a evolução do trabalho.

Ao Leo, por todo amor, carinho, afeto, aconchego, COMPREENSÃO E EMPATIA, e por sempre me dar forças e apoio para continuar.

À Cami, por ouvir todas as lamúrias e pela ajuda com as estruturas mapeadas.

Aos meus queridos amigos Marília, Thaís, Lívia e João, por todo apoio e carinho.

A ANP/BDEP, por fornecer os dados utilizados sísmicos e de poços que serviram como base para esta pesquisa.

A DUG, por disponibilizar a licença acadêmica do *software* DUG Insight fundamental em grande parte do desenvolvimento deste estudo.

A PETROBRAS, pela concessão de apoio financeiro por meio de bolsa de estudos, e ao projeto "Inteligência artificial aplicada à exploração de petróleo na camada pré-sal- Projeto 28184".

À Pro-Reitoria de Pós-Graduação da UFMG (PRPg) e ao Programa de Pós-Graduação em Geologia do Instituto de Geociências (PPG-IGC), por fornecer as condições necessárias para a realização deste trabalho. Também agradeço profundamente ao William por todo apoio, dedicação e prontidão para resolver qualquer problema!

RESUMO

O Campo de Búzios destaca-se como um dos campos de petróleo mais produtivos ao longo da margem leste brasileira. Apesar de haver inúmeras pesquisas focadas nos reservatórios do pré-sal, poucos são os estudos dedicados à caracterização tridimensional de toda a área do Campo de Búzios. Portanto, este trabalho objetiva a caracterização espacial de um volume ao longo do Campo de Búzios utilizando interpretação tridimensional do volume sísmico integrada à análise de atributos sísmicos e de dados de poços. A combinação dessas ferramentas permitiu a compreensão de diversos parâmetros relacionados à evolução tectono-estratigráfica da Bacia de Santos. Na área mapeada, foram identificadas cinco unidades com características sísmicas bem marcadas: Sin-Rifte I, Sin-Rifte II, Pós-Rifte I, Pós-Rifte II, Drifte I e Drifte II. O modelo 3D revelou importantes feições, como a variação de profundidade da unidade Sin-Rifte I e a morfologia bastante heterogênea da unidade Pós-Rifte II. A unidade Sin-Rifte I apresenta maior profundidade em direção a N-NW e menor profundidade em direção a S-SE, devido a um sistema regional de semi-grabens. Esse sistema influencia a geometria e a espessura do pacote pré-sal, uma vez que altos e baixos estruturais são um importante condicionante da acomodação dos sedimentos. A unidade Pós-Rifte I exibe uma geometria predominantemente regular e espessura constante, mas tende a espessar em direção ao S-SE e apresenta uma leve flexura descendente em direção a NE, no sudeste do Campo de Búzios. Em três dimensões, a morfologia complexa da unidade Pós-Rifte II é evidenciada pela variação de espessura e topografia irregular, o que evidencia a intensa halocinese atuante na Bacia de Santos. Acima da camada evaporítica, a espessura da unidade Drifte I é altamente condiconada pela morfologia do sal, com pacotes mais espessos e deformados em áreas em que a seção salina é mais fina. Por sua vez, a unidade Drifte II apresenta espessura relativamente constante, com variações menores próximas às zonas de falha. Comparações com outros campos dentro da Bacia de Santos (Tupi e Sapinhoá/Lapa) revelam diferenças na espessura das camadas, mobilização e rotação dos blocos sin-rifte. A camada Pós-Rifte I (Formação Barra Velha) e o pacote Pós-Rifte II (Formação Ariri) são mais finos e menos mobilizados na área do Campo de Búzios. Além disso, os blocos sin-rifte são menos rotacionados e os refletores internos apresentam menor inclinação na área de estudo quando comparados a esses outros campos. Portanto, essa pesquisa conclui que a menor mobilização de sal, a menor espessura do pacote pós-rifte e a menor rotação dos blocos sin-rifte observadas na área do Campo de Búzios estão relacionados à distância relativa da margem continental e, consequentemente, à quantidade de deslocamento gerada pelo Rifte do Atlântico Sul. Nesse contexto, o Campo de Búzios encontra-se em uma região mais

proximal em comparação com os campos de Tupi e Sapinhoá/Lapa, apresentando características que sugerem um deslocamento menor.

Palavras-chave: caracterização sísmica; evolução tectônica; bacias do tipo rifte; Bacia de Santos; Campo de Búzios.

ABSTRACT

The Búzios Field is one of the most prolific petroleum fields along the Eastern Brazilian Margin. Despite significant research conducted restrictedly on the pre-salt reservoirs, few studies have focused on the three-dimensional characterization of the entire Búzios Field area. Therefore this work aims to spatially characterize a volume along the Búzios Field area using 3D seismic volume interpretation, seismic attributes, and well-log data. The combined use of these tools allowed the understanding of several parameters concerning the tectonostratigraphic evolution of the Santos Basin. Within the mapped area, we identified five units: Syn-Rift I, Syn-Rift II, Post-Rift I, Post-Rift II, Drift I, and Drift II. The 3D model reveals significant features such as the depth variation of the Syn-Rift I unit and the heetrogeneous morphology of the Post-Rift II unit. The Syn-Rift I unit is deeper towards the N-NW and shallower towards the S-SE due to a regional half-grabens system. This system impacts the pre-salt geometry and thickness, as structural highs and lows are relevant factors in sediment accommodation. The Post-Rift I unit has a predominantly regular geometry and thickness but tends to thicken towards the S-SE and exhibits slight downward flexure towards the NE in the southeast of the Búzios Field. In three dimensions, the heterogeneous morphology of the Post-Rift II unit is evidenced by the variable thickness and irregular topography, accounting for the intense halokinesis in the Santos Basin. Above the evaporitic layer, the thickness of the Drift I unit is highly conditioned by salt morphology, with thicker and deformed packages in areas of thinner salt section. On the other hand, the Drift II unit shows relatively constant thickness with minor variations near fault zones. Comparisons with other fields within the Santos Basin (Tupi and Sapinhoá/Lapa) reveal differences in layer thickness, mobilization, and rotation of the syn-rift blocks. The Post-Rift I layer (Barra Velha Fm.) and the Post-Rift II package (Ariri Fm.) are thinner and less mobilized in the Búzios Field area. Moreover, the syn-rift blocks are less rotated, and the internal reflectors have a lower inclination in the study area when compared to these other fields. Therefore, this research concludes that the lower mobilization of salt, the lower thickness of the post-rift package, and the minor syn-rift block rotation observed in the Búzios Field area are associated with the relative distance from the continental margin and, consequently, with the amount of displacement generated by the South Atlantic Rift. In this case, the Búzios Field is located in a more proximal portion than Tupi and Sapinhoá/Lapa fields, exhibiting features suggestive of a lower displacement.

Keywords: seismic characterization; tectonic evolution; rift basins; Santos Basin; Búzios Field.

LISTA DE ILUSTRAÇÕES DISSERTAÇÃO

LISTA DE ILUSTRAÇÕES MANUSCRITO

SUMÁRIO

1 INTRODUÇÃO

1.1 Apresentação

A exploração de petróleo nas bacias da margem leste brasileira tomou novos rumos nos últimos 50 anos. Na década de 1970, alguns projetos levaram a uma investigação sistemática das bacias sedimentares offshore usando conjuntos de dados geofísicos comumente usados por empresas de petróleo. A interpretação foi feita com base em dados geológicos (principalmente resultados estratigráficos de poços exploratórios perfurados pela Petrobras) e geofísicos (principalmente dados sísmicos e de campo potencial) que suportam a interpretação da arquitetura tectônico-sedimentar dos diversos segmentos ao longo da margem continental (Mohriak & Fainstein, 2012). Entre meados da década de 1970 e meados da década de 1980, a Bacia de Campos consolidou-se como importante produtora de petróleo. No entanto, devido à segunda crise do petróleo e à necessidade de aumentar a produção nacional, foi necessário buscar novas fontes de petróleo. Em 1980, foi registrada a primeira ocorrência de petróleo armazenado em arenitos turbidíticos na Bacia de Santos, e a descoberta de um reservatório carbonático na porção sul aumentou a expectativa de um grande produtor de petróleo (Chang et al. 2008).

O cenário brasileiro de exploração de petróleo alcançou uma perspectiva de maior nível com a descoberta de petróleo e gás nas camadas do Pré-sal da Bacia de Santos em 2008 (Papaterra, 2010). Essa bacia, limitada ao norte com a Bacia de Campos e ao sul com a Bacia de Pelotas, tornou-se fronteira da província de exploração de hidrocarbonetos (Fig. 1). Atualmente, a Bacia de Santos é a maior produtora de hidrocarbonetos do Brasil, cujo reservatório é caracterizado pelo volume potencial de reservas, alta produtividade, qualidade do petróleo, baixa exploração e risco de produção (Souza & Sgarbi, 2019). Em 2017, a produção diária de petróleo na Bacia de Santos foi da ordem de um milhão de barris e a produção diária de gás natural foi da ordem de 48,8 milhões de m³ (ANP, 2017). Sua grande extensão e proximidade com a Bacia de Campos, aliadas à escassez de informações sobre a geologia e os sistemas petrolíferos, conferem à Bacia de Santos o título de bacia pouco conhecida e promissora quando comparada a outras bacias brasileiras (por exemplo, as bacias de Campos e Espírito Santo; Chang et al. 2008, Souza & Sgarbi, 2019).

Um dos campos mais promissores da Bacia de Santos é o de Búzios, em que o reservatório carbonático foi responsável por 5% da produção de petróleo do Pré-sal da Bacia de Santos em 2019 (Castro, 2019). Em 2016, sua produção acumulada foi de cerca de 2,47 bilhões de barris de petróleo e 86,47 milhões de m^3 de gás natural (ANP, 2016). Nesse contexto,

minha pesquisa busca caracterizar tridimensionalmente o arcabouço geológico de uma região inserida no Campo de Búzios, Bacia de Santos. A primeira etapa consiste na caracterização tridimensional ancorada na interpretação de inúmeras seções sísmicas ao longo do cubo de dimensões 20 x 36 x 7,995 km, visando extrair padrões sísmicos bem-marcados e coerentes com a estratigrafia descrita na região. Ainda, foram utilizados múltiplos atributos sísmicos e perfis geofísicos para auxiliar na identificação dos horizontes-chave delimitadores desses padrões. A segunda etapa to trabalho consiste na geração do volume 3D representando esses horizontes-chave em profundidade.

1.2 Objetivos

O principal foco do trabalho é a caracterização tridimensional geológica, tectônica e estrutural do Campo de Búzios, visando relacionar as unidades mapeadaes com as unidades estratigráficas e tectônicas da Bacia de Santos. Com isso, espera-se reconstruir a evolução tectono-estratigráfica da bacia no contexto da abertura do Oceano Atlântico Sul, a partir da relação entre as unidades mapeadas e sua resposta sísmica, à luz do mecanismo de rifteamento responsável pela abertura da bacia.

Os resultados obtidos no trabalho são descritos, ilustrados e discutidos na presente dissertação. O trabalho desenvolvido durante a pesquisa foi compilado na forma de artigo científico a ser submetido à publicação no periódico Journal of South American Earth Sciences. O manuscrito será apresentado no Capítulo 4 deste volume.

1.3 Localização

A área de estudo está inserida no Campo de Búzios, Bacia de Santos (Fig. 1), a 180 km da cidade do Rio de Janeiro e a cerca de 2000 m abaixo do nível do mar. O volume usado como base de dados possui dimensões XxYxZ de 20 x 36 x 7,995 km, respectivamente.

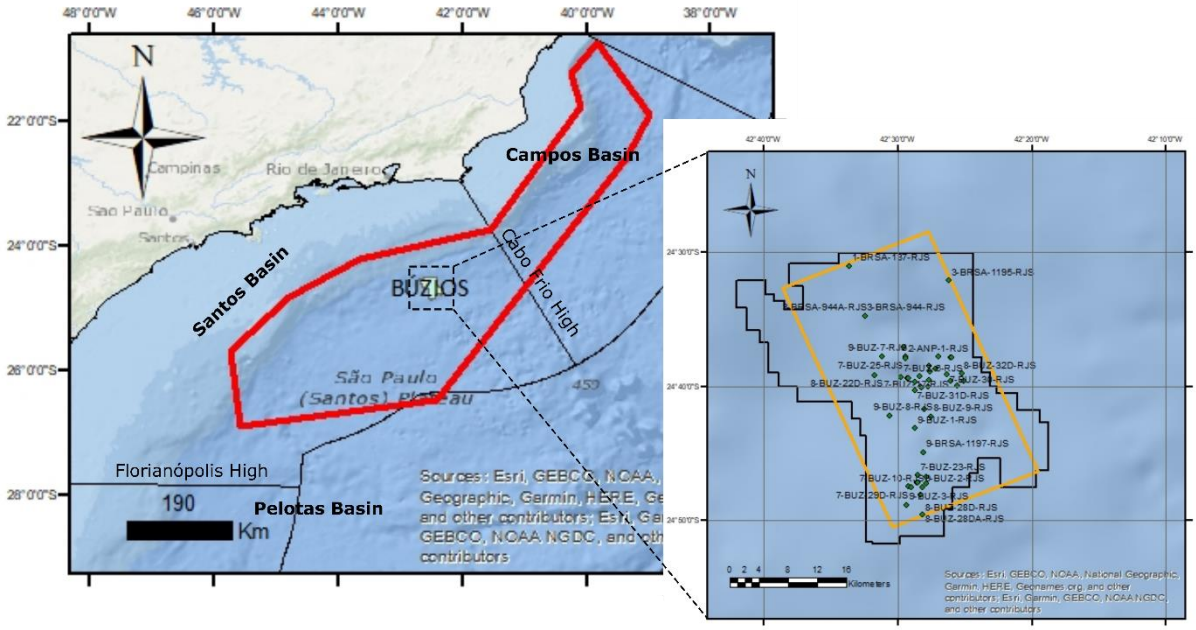

Figura 1 - Mapa de localização do Campo de Búzios (contorno preto) na Bacia de Santos. O polígono vermelho delimita os limites do pré-sal e o polígono laranja delineia a área de estudo. Os pontos verdes representam os perfis de poços públicos disponíveis pela ANP. Fonte: Elaborada pela autora.

2 CONTEXTO GEOLÓGICO REGIONAL

2.1 Bacia de Santos

O desenvolvimento de bacias de margem passiva é atribuído a processos extensionais da litosfera que resultam em rifteamento da crosta e abertura oceânica (Heilbron et al. 2000). Em relação ao Escudo Atlântico do sudeste do Brasil (Fig. 2), as bacias de margem passiva foram geradas a partir da distensão litosférica associada à ruptura do Gondwana e consequente abertura do Oceano Atlântico Sul desde o Mesozóico (Milani et al. 2000). O evento termotectônico, denominado Orogênese Brasiliana no Brasil e Orogênese Pan-africana na África, afetou tanto rochas supracrustais quanto infracrustais, que foram posteriormente recobertas por bacias sedimentares extensionais. Enquanto as bacias intracratônicas do Paraná, Amazonas e Parnaíba representam o estágio intracratônico Paleozóico-Mesozóico, as bacias de Santos e de Campos representam as raízes atuais do processo extensional associado aos riftes Jurássico-Cretáceo (Heilbron et al. 2000). O sistema de riftes São-Paulo-Taubaté-Resende-Guanabara-Barra de São João corresponde às bacias pós-ruptura e aos plutons alcalinos associados, desenvolvidos durante a reativação tectônica no Cretáceo/Terciário (Almeida, 1976 apud Heilbron et al. 2000).

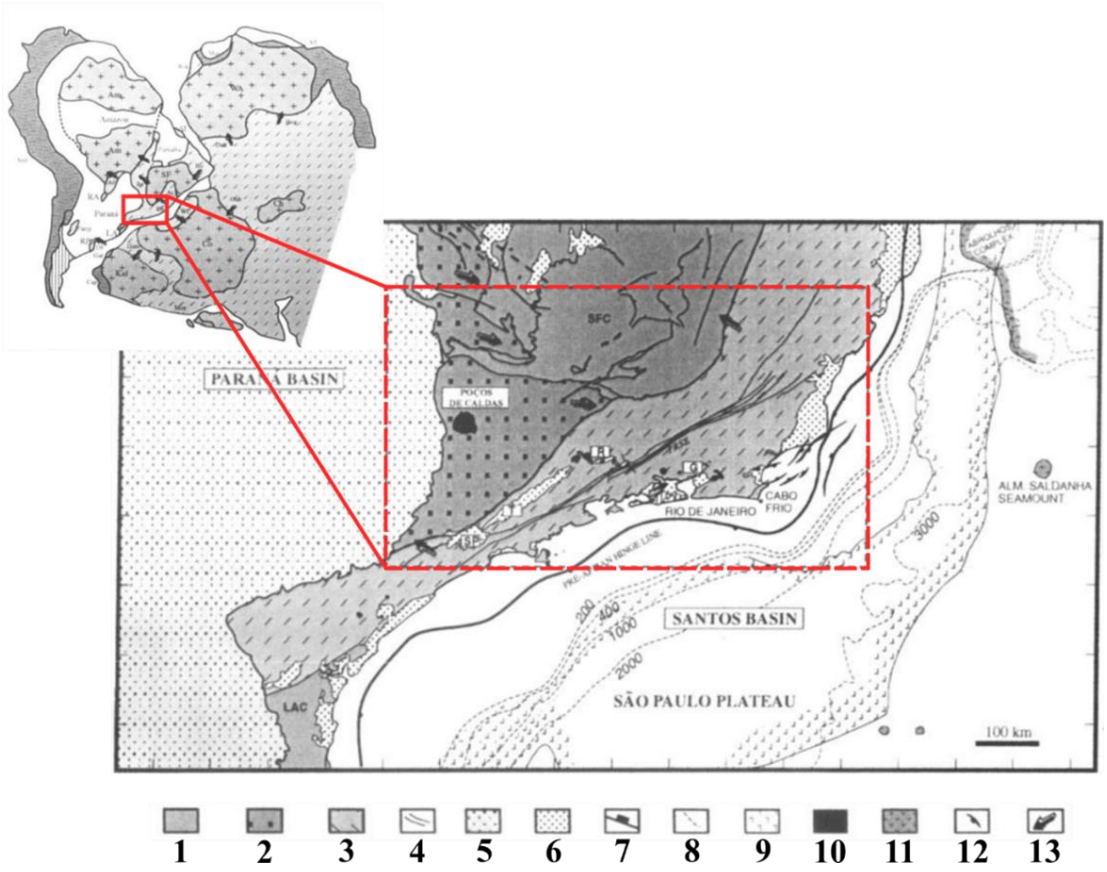

Figura 2 - À esquerda, mapa tectônico esquemático de parte do oeste de Gondwana, simplificado de Trompette (1994), Almeida & Hasui (1984). À direita, mapa tectônico simplificado do sudeste do Brasil, modificado de Heilbron et al. (1995), Campos Neto & Figueiredo (1995). Legenda: 1 - Cráton do São Francisco (CSF) e zona de antepaís das faixas dobradas do Brasiliano; 2 - Faixa Brasília; 3 - Faixa Ribeira; 4 - Zona de cisalhamento do Paraíba do Sul (ZCPS); 5 - Bacia do Paraná; 6 - Cobertura cenozoica e riftes interiores de São Paulo (SP), Taubaté (T), Resende (R) e Guanabara (G); 7 - Linha de dobramento pré-Aptiana; 8 - Contornos batimétricos (profundidade em metros); 9 - Evaporitos Aptianos; 10 - Rochas alcalinas meso-cenozoicas; 11 - Rochas vulcânicas meso-cenozoicas; 12 - Principais falhas normais; 13 - Vergência tectônica dos cinturões de dobras. Fonte: Adaptada de Heilbron et al. (2000).

Nesse contexto, a Bacia de Santos está localizada ao sudeste da margem continental brasileira entre a Zona de Fratura Florianópolis e o Alto de Cabo Frio (Fig. 3), cuja extensão e batimetria correspondem a 350.000 km^2 e 3000 m, respectivamente (Moreira et al. 2007). Mio et al. (2005) descrevem-na como uma bacia de margem passive relacionada à quebra do supercontinente Gondwana no Neocomiano.

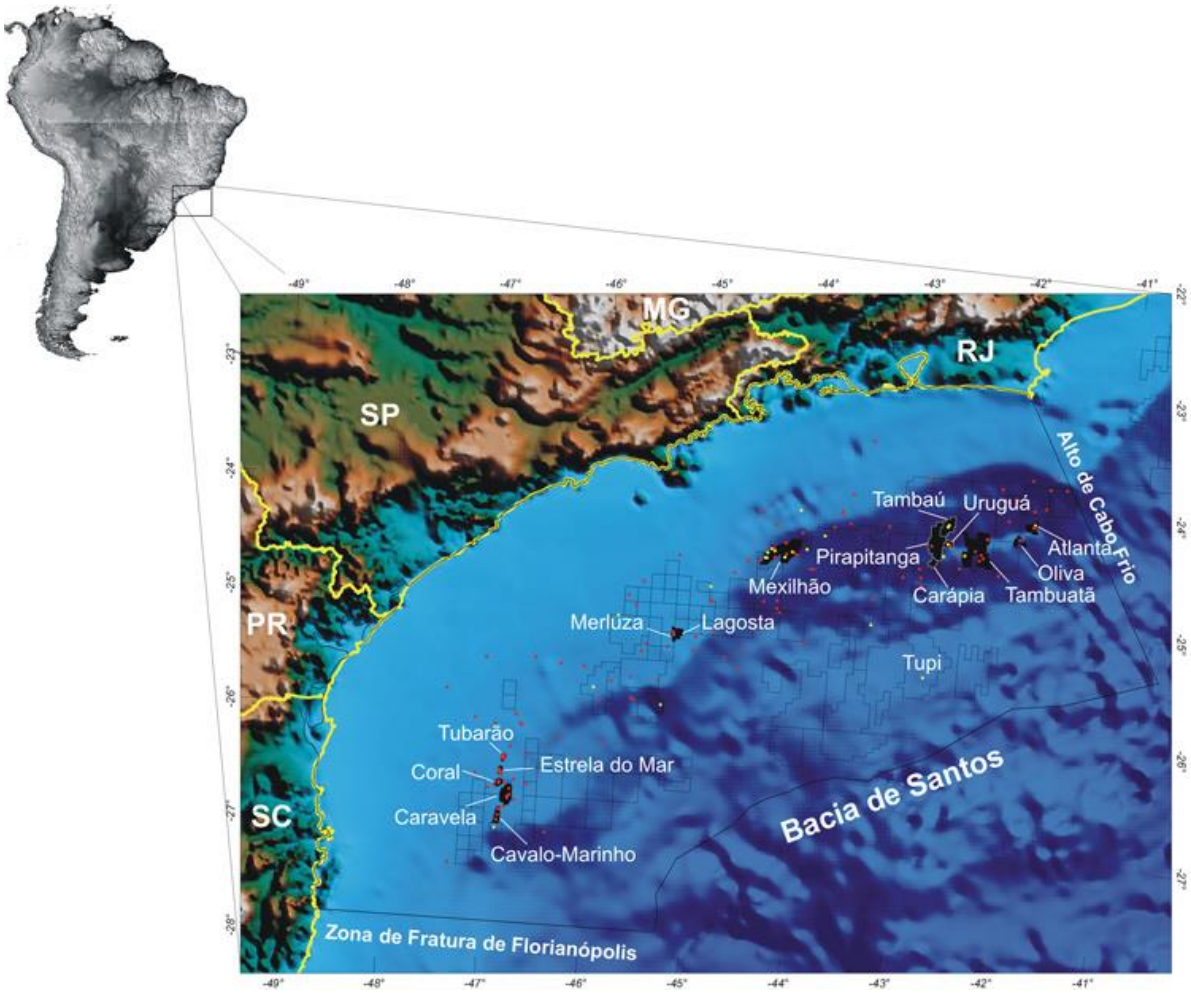

Figura 3 - Mapa de localização da Bacia de Santos e áreas adjacentes. Os polígonos preenchidos correspondem aos campos produtores e os polígonos vazios correspondem aos blocos de exploração. Os pontos vermelhos correspondem aos poços exploratórios públicos e os pontos amarelos aos poços exploratórios confidenciais. Fonte: Chang et al. (2008).

2.1.1 Evolução tectono-estratigráfica

De forma amplamente difundida, a evolução da Bacia de Santos é dividida em três fases principais: rifte, pós-rifte e drifte (Moreira et al. 2007), sendo essas fases associadas a supersequências deposicionais. Essas supersequências são separadas por discordâncias angulares e erosivas, e estão hierarquicamente agrupadas (Mohriak & Fainstein, 2012).

2.1.1.1 Embasamento cristalino e econômico

Em relação ao registro litoestratigráfico (Fig. 4), Moreira et al. (2007) definem a bacia como uma sucessão de megassequências deposicionais sobre o embasamento cristalino Pré-Cambriano do Complexo Costeiro e metassedimentos da Faixa Ribeira. Consiste principalmente de granitos e gnaisses que formam charneira de idade cretácea que limita os mergulhos suaves do embasamento a oeste, dos mais acentuados a leste. Sobreposto ao

Complexo Costeiro, encontra-se o embasamento econômico definido pelos derrames de basaltos continentais da Formação Camboriú.

2.1.1.2 Supersequência rifte

A supersequência rifte está relacionada à separação dos paleocontinentes sul-americano e africano durante o final do Neocomiano e início do Aptiano. Essa fase foi responsável por iniciar a deposição do material lacustre do Grupo Guaratiba, que consiste em cunhas de sedimentos siliciclásticos de granulometria grossa associados a fragmentos de basalto, quartzo e coquinas subordinadas depositados em grabens gerados por falhas normais de alto ângulo (Milani et al. 2000; Rigoti, 2015). Este grupo engloba as formações Camboriú, Piçarras e Itapema do estágio rifte, e as formações Barra Velha e Ariri do estágio pós-rifte.

A Formação Camboriú é constituída por derrames basálticos continentais do Cretáceo Inferior, de granulação fina a média, textura ofítica, compostos majoritariamente por augita e plagioclásio. Esses derrames estão posicionados sob a cobertura sedimentar de praticamente toda a Bacia de Santos e sobre o embasamento do Complexo Costeiro por meio de superfícies discordantes. No limite superior da Formação Camboriú, a Formação Piçarras marca a sedimentação de leque aluvial, com conglomerados e arenitos polimíticos associados a fragmentos de basaltos, quartzo e feldspato na porção proximal e arenitos finos, siltitos e argilitos ricos em talco na porção distal (Moreira et al. 2007).

A fase rifte encerra-se com a deposição da Formação Itapema, caracterizada pela intercalação de calciruditos e folhelhos escuros depositados do Neobarremiano ao Eoaptiano. Seu limite inferior é a discordância intrabarremiano de 126,4 Ma conhecida como pré-Alagoas. A porção carbonática corresponde a fragmentos biogênicos de conchas de bivalves dolomitizadas e/ou silicificadas, informalmente denominadas “coquinas”, análogas à Formação Lagoa Feia na Bacia de Campos. A fácies proximal é representada por leques aluviais compostos por conglomerados e arenitos, enquanto a distal é caracterizada por folhelhos ricos em matéria orgânica (Moreira et al. 2007; Papaterra, 2010).

2.1.1.3 Fase pós-rifte

A supersequência pós-rift representa o estágio transicional entre a deposição continental e marinha, cujo regime tectônico é menos ativo. É composta por fluxos basálticos, carbonatos, arenitos, folhelhos e evaporitos depositados no Aptiano (Rigoti, 2015). Essa fase é representada pelos carbonatos não-marinhos de águas rasas da Formação Barra Velha cobertos pela espessa camada salina da Formação Ariri (Buckley et al. 2015).

Os corpos carbonáticos espessos da Fm. Barra Velha que atingem mais de 500 m de espessura foram depositados a partir do influxo periódico de grandes lagos alcalinos e rasos na bacia (Szatmari & Milani, 2016). Ainda, essa unidade é dividida nos domínios inferior e superior separados pela discordância intra-Alagoas, em que o inferior é composto por calcários microbiais, estromatólitos e lamitos nas porções proximais, e folhelhos nas porções distais. Grainstones e packstones compostos por fragmentos de estromatólitos e bioclastos de ostracodes ocorrem subordinadamente. Esse domínio marca a transição do ambiente continental para marinho raso. Já o domínio superior é composto por calcários microbiais intercalados a lamitos localmente dolomitizados e arenitos e conglomerados (Moreira et al. 2007; Papaterra, 2010). O domínio superior apresenta uma geometria em cunha mais proeminante que o inferior, o que pode representar o aumento aumento da taxa de sedimentação nos estágios finais da deposição carbonática (Buckley et al. 2015).

Os carbonatos da Formação Barra Velha são cobertos pelos evaporitos aptianos da Formação Ariri, que consiste principalmente na intercalação de halita e anidrita (± taquidrita, carnalita, silvinita) (Milani et al. 2000, Moreira et al. 2007). As camadas evaporíticas representam a predominância do mecanismo da halocinese, regime gravitacional complexo que compartimentalizou a bacia em vários componentes tectônicos, como *pillows*, diápiros e muralhas de sal, depressões íngremes, cunhas de subsidência, grabens, grandes dobras e empurrões invertendo localmente as mini-bacias formadas entre os altos salinos (Milani et al. 2000; Mohriak & Fainstein, 2012). Além disso, a tectônica de sal resultou no empilhamento de vários sistemas turbidíticos, que foram amalgamados verticalmente e coalescidos lateralmente, formando cunhas espessas que frequentemente apresentam inversão de depocentro (Mohriak, 2003).

No entanto, Mohriak & Fainstein (2012) dividem a supersequência pós-rifte em duas sequências marinhas e consideram os carbonatos continentais lacustres da Fm de Barra Velha como sedimentos marinhos rasos. A primeira sequência incia-se com uma sucessão sedimentar predominantemente carbonática em uma plataforma de águas rasas de idade albiana, enquanto a segunda representa um aumento da profundidade da água e a substituição dos carbonatos por sedimentos siliciclásticos de águas profundas, marcando um episódio transgressivo.

2.1.1.4 Fase drifte

A última fase da evolução tectônica da Bacia de Santos é corresponde ao drifte (ou deriva) continental responsável pela instalação de uma bacia marinha associada à abertura do oceano Atlântico desde o Albiano (Rigoti, 2015). Essa supersequência é relacionada à

subsidência termal associada à halocinese e está subdividida em três sequências depositadas durante o progressivo aumento da profundidade da bacia: os grupos Camburi, Frade e Itamambuca.

O Grupo Camburi é resultado do aumento do nível do mar e é representado, da base para o topo, pelas formações Florianópolis inferior, Guarujá e Itanhaém inferior (Milani et al. 2000; Moreira et al. 2007; Papaterra, 2010). Logo acima da cobertura evaporítica da Fm Ariri, a Fm. Florianópolis inferior representa a fácies proximal de um sistema de leques aluviais e deltaicos. Essa unidade é composta por conglomerados avermelhados, arenitos e folhelhos (Moreira et al. 2007). Na sequência, a Fm. Guarujá marca a implantação de uma plataforma carbonática durante o Albiano, composta majoritariamente por carbonatos acinzentados. A Fm. Itanhaém inferior é composta por folhelhos radioativos recobertos por margas e calcilutitos de origem marinha distribuídos desde a plataforma até a porção bacinal. Em um contexto de progressivo aprofundamento da bacia, a inundação máxima foi alcançada durante o Neocenomaniano-Turoniano, quando os folhelhos negros da Fm. Itajaí-Açu foram intercalados aos sedimentos pelíticos do topo da Fm. Itanhaém (Milani et al. 2000). Estes folhelhos negros e argilitos representam a plataforma distal e ambiente de talude continental (Moreira et al. 2007).

A sequência intermediária da fase de drifte é representada pelo Grupo Frade depositado entre o Cenomaniano e o Maastrichtiano. Essa unidade é formada, da base para o topo, pelas formações Santos, Juréia e Itajaí-Açu, e o Membro Ilha Bela. O Grupo Frade representa um estágio de regressão marinha onde o limite da plataforma avançou até 200 km costa afora. Entre o Santoniano e o Maastrichtiano, uma espessa cunha de conglomerados avermelhados da Fm. Santos e arenitos e argilitos marinhos rasos da Fm. Juréia foram depositados na Bacia de Santos em resposta ao soerguimento da Serra do Mar (Milani et al. 2000, Moreira et al. 2007). O Membro Ilha Bela consiste em um reservatório turbidítico composto por arenitos imaturos maciços associados à alteração de litoclastos vulcânicos (Chang et al. 2008).

O Grupo Itamambuca representa o fim da fase drifte e engloba as formações Ponta Aguda, Marambaia, Iguape e Sepetiba. Do Paleoceno superior ao Eoceno inferior, os arenitos avermelhados da Fm. Ponta Aguda foram depositados em um contexto de sistemas aluviais e fluviais, enquanto os siltitos, arenitos e folhelhos da Fm. Marambaia foram depositados em uma plataforma distal e ambiente de talude. O Membro Maresias pertencente à Fm. Marambaia consiste em arenitos resultantes de densas correntes de turbidez fortemente canalizadas e relacionadas a importantes escavações no talude e na plataforma (Milani et al. 2000).

Durante o Cenozóico, a evolução tectônica da Bacia de Santos foi marcada por uma progradação de sedimentos siliciclásticos das formações Iguapé e Sepetiba, que se inclinavam sobre o sistema de taludes continentais da Formação Marambaia. Essa sequência final corresponde a um sistema progradante com expressivo desenvolvimento de clinoformas de talude e avanço da quebra da plataforma. Durante a deposição dessa sequência, ocorre significativo vulcanismo extrusivo de caráter basáltico-alcalino na bacia (Milani et al. 2000; Moreira et al. 2007).

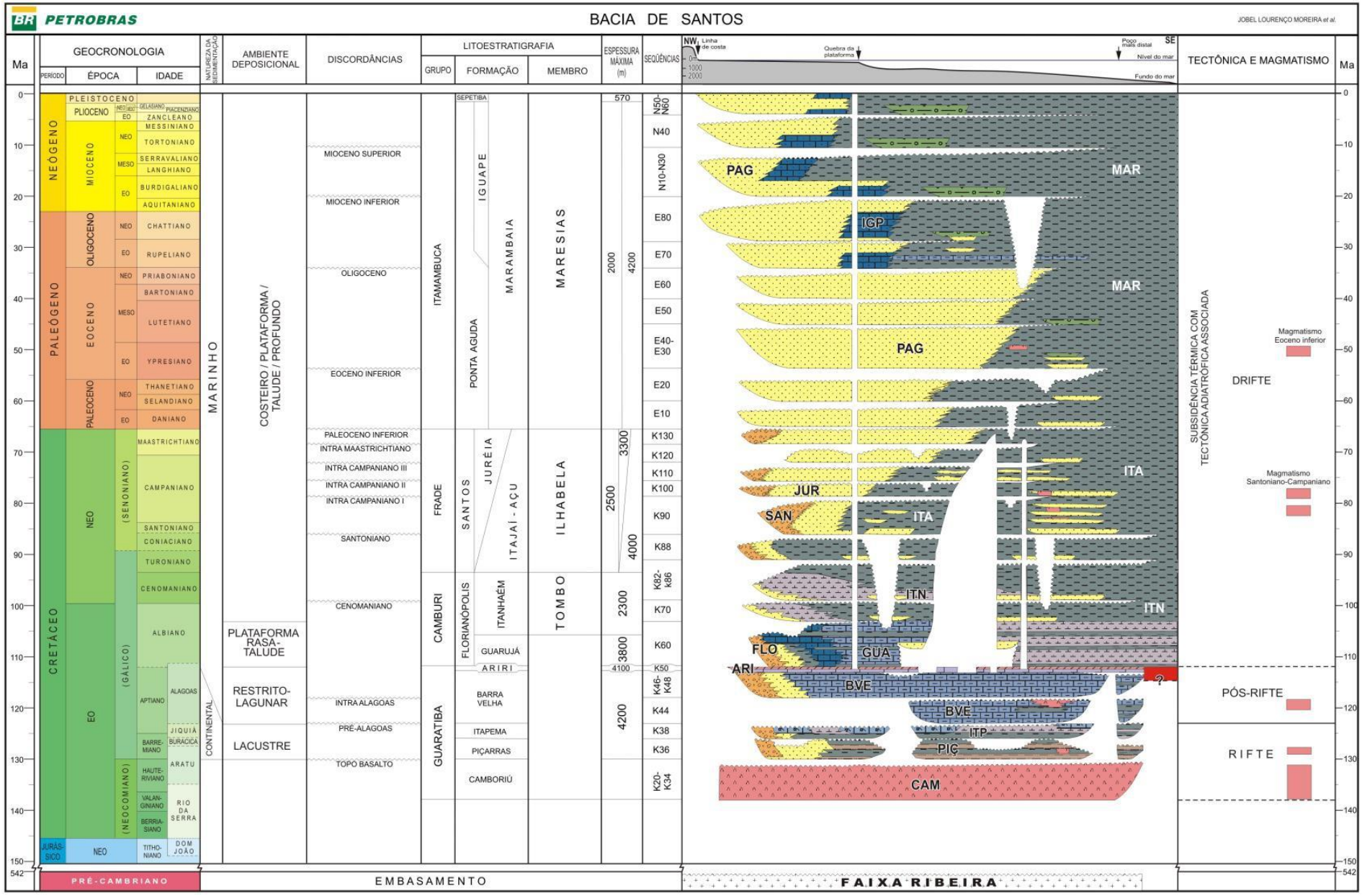

Figura 4 - Carta cronoestratigráfica da Bacia de Santos. Fonte: Moreira et al. (2007).

2.1.2 Campo de Búzios

O Campo de Búzios está localizado na porção central da Bacia de Santos (Fig. 5), no litoral sudeste do Brasil, a aproximadamente 180 km da cidade do Rio de Janeiro. Representante da seção pré-sal da bacia (sistema Piçarras-Itapema/Barra Velha), é atualmente um dos campos de petróleo mais produtivos do país, com uma extensão de 852 km^2 e ca. 1.900 m de elevação batimétrica (ANP, 2016, 2019). As rochas reservatório estão posicionadas entre 5.000 e 6.000 m abaixo do nível do mar e consistem em sedimentos carbonáticos biogênicos in situ e/ou retrabalhados da Formação Barra Velha e fragmentos bioacumulados de bivalves (“coquinas”) da Formação Itapema (ANP, 2016).

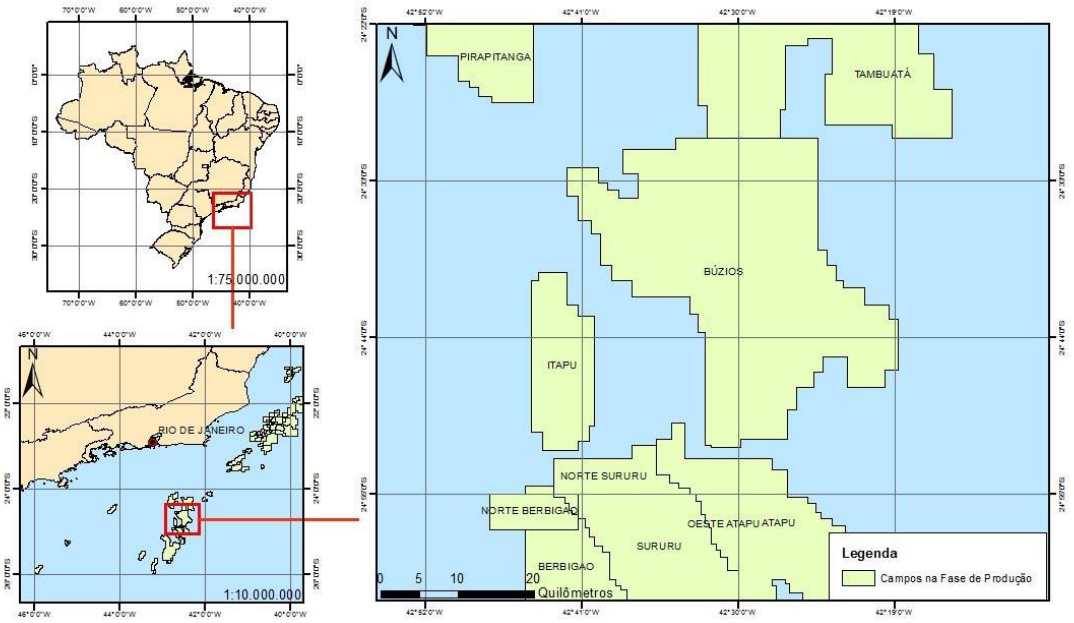

Figura 5 - Localização do campo de Búzios. Fonte: ANP (2016).

Na área do Campo de Búzios, a mega-sequência rifte tem início com a extrusão dos basaltos continentais da Formação Camboriú, que podem estar intercalados com rochas vulcanoclásticas, conforme evidenciado nos registros de perfil composto (3-BRSA-1053-RJS). No parágrafo seguinte, a geologia do Campo de Búzios é sintetizada de acordo nas descrições apresentadas em Tavares dos Santos & Gordon (2021). Essa mega-sequência é fortemente influenciada pela tectônica e divide-se em sequências superior e inferior. A sequência inferior é formada pela Formação Piçarras, que apresenta o maior desenvolvimento de cunhas sedimentares com espessamento em direção aos hanging-walls das falhas normais, atingindo espessuras de até 2.200 m. A sequência

superior corresponde à Formação Itapema, que inclui a "seção de coquinas" da Bacia de Santos, composta por um pacote espesso (até 300 m) de ruditos de bivalves e, em menor quantidade, grainstones bioclásticos, packstones, wackstones, mudstones e folhelhos depositados em ambientes de alta energia.

Em relação à mega-sequência pós-rifte, os carbonatos da Formação Barra Velha, no Campo de Búzios, ocorrem em várias fácies, como argilas ricas em Mg (estevenita), *shrubs*, esferulitos e lamas carbonáticas. Esses carbonatos variam em espessura de aproximadamente 200 a 400 m em pontos estruturais elevados (Tavares dos Santos & Gordon, 2021; Ferreira, 2022). As porções basal e superior da Formação Barra Velha são dominadas por sedimentos de lama carbonática, enquanto a porção intermediária é dominada por sedimentação de carbonato *in situ*, com presença de *shrubs* e esferulitos (Ferreira, 2022). As estruturas salinas da Formação Ariri alcançam espessuras de até 2.650 m na parte central do Campo de Búzios, diminuindo em direção ao norte e ao sul, formando janelas de sal (ou cicatrizes salinas). A estratificação de evaporitos tem início com a precipitação de anidrita na base, seguida por um espesso pacote de halita, que representa o depósito evaporítico mais comum.

A mega-sequência drifte na área de Búzios tem início com depósitos de carbonato microbiano fino da Formação Guarujá, composta principalmente por carbonatos de grão fino (mudstone e calcilutito) depositados em condições marinhas restritas distais, com espessuras típicas variando de 10 a 30 m. Acima da Formação Guarujá, a Formação Itanhaém é composta por margas e folhelhos intercalados, com expressão local nas proximidades do poço 3-BRSA-1053-RJS. Perfis compostos (3-BRSA-1053-RJS, 3-BRSA-1064-RJS) revelam camadas espessas de arenito intercaladas com folhelhos e margas subordinadas da Formação Itajaí-Açu, exibindo uma sequência de *coarsening-up* com espessura de até 430 m. A Formação Marambaia, composta por um pacote espesso de aproximadamente 650 m de folhelhos e arenitos, foi depositada em condições de mar aberto desde o Eodaniano até tempos recentes (Moreira et al. 2007). Estruturalmente, os depósitos pós-sal na área de Búzios são completamente controlados pela halocinese (Tavares dos Santos & Moreira, 2021).

3 ATRIBUTOS SÍSMICOS

Os atributos sísmicos, de maneira geral, são descritos como qualquer informação obtida a partir dos dados sísmicos, seja por medidas diretas ou por raciocínio lógico e/ou baseado em experimentos (Taner, 2001). Tais atributos funcionam como importantes

ferramentas na interpretação sísmica em subsuperfície, uma vez que nos permitem investigar o ambiente deposicional e estrutural, viabilizando a inferência de certas características ou propriedades de interesse e auxiliando na previsão de propriedades litológicas e petrofísicas (Chopra & Marfurt, 2007).

Todos os atributos sísmicos são dependentes uns dos outros, sendo apenas maneiras distintas de apresentar e estudar uma quantidade limitada de informações básicas. Essas informações correspondem a tempo, amplitude, frequência e atenuação. Resumidamente, atributos derivados de tempo fornecem informações estruturais, atributos derivados de amplitude fornecem informações sobre a estratigrafia e propriedades do reservatório. Atributos derivados de frequência são pouco compreendidos, no entanto, podem fornecer informações estratigráficas e de reservatórios úteis adicionais. Já a atenuação pode fornecer informações sobre a permeabilidade. Quando combinadas informações de amplitude e frequência, os atributos são denominados híbridos (Brown, 2011). Cada um desses atributos está relacionado entre si, em que alguns possuem maior ou menor sensibilidade à determinada característica.

Os atributos podem ser classificados de acordo com várias propriedades, podendo ser geométricos, físicos, refletivos, transmissivos, instantâneos e uma série de outra categorias (ver Brown, 2011). Nesta dissertação, focaremos em quatro desses atributos: amplitude (ou envelope) instantânea, fase instantânea, sweetness instantânea e semblance (similarity), uma vez que foram os que melhor discriminaram as unidades sísmicas descritas no capítulo 4 deste volume.

3.1 Atributos instantâneos

Os atributos são ditos instantâneos quando computados amostra por amostra e representam variações instantâneas de parâmetros diversos. Valores instantâneos de atributos como envelope do traço e suas derivadas, frequência e fase podem ser determinados a partir de traços complexos (Taner, 2001). O conceito de traço complexo ou sinal analítico *F(t)* é detalhadamente descrito por Taner et al. (1979). De maneira resumida, o traço complexo é calculado a partir da soma do traço sísmico convencional *f(t)* e do componente complexo *jf*(t)* denominado quadratura ou conjugado, sendo $j = \sqrt{-1}$ (Fig. 6). O traço sísmico convencional corresponde à parte real do traço complexo, facilmente calculada sob condições usuais, e a quadratura do traço ou conjugado $f^*(t)$ corresponde à parte imaginária do sinal, como mostrado na equação 1.

$$F(t) = f(t) + jf^*(t) \quad (1)$$

Dessa maneira, a parte real *f(t)* pode ser obtida em função da amplitude *A(t)* e da fase *θ(t)* em função do tempo, segundo a equação 2. Já a parte imaginária *f***(t)* da equação 1 pode ser determinada a partir de uma operação de convolução linear (*) sobre a parte real ou também em função de *A(t)* e *θ(t)* como mostrado na equação 3. As equações infracitadas foram extraídas de Taner et al (1979).

$$f(t) = A\,(t) \times cos\theta\,(t) \quad (2)$$

$$f^{*}(t) = A\,(t) \times sin\theta\,(t) \quad (3)$$

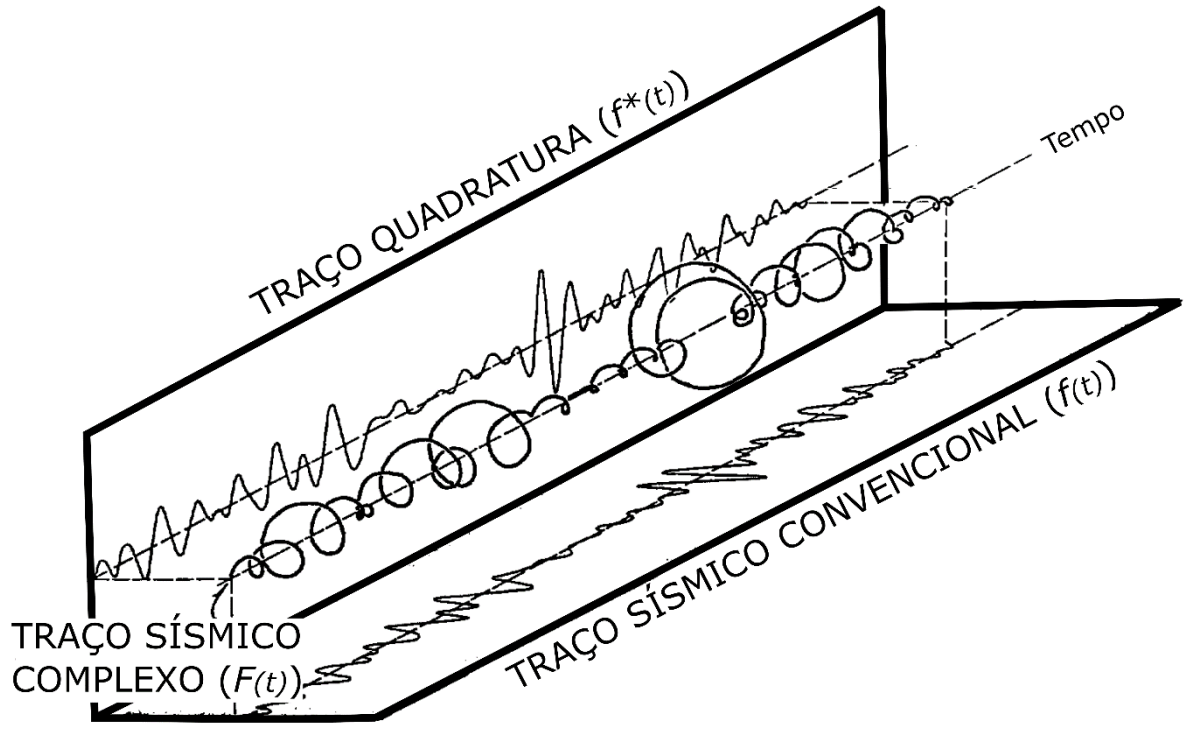

Figura 6 - Diagrama isométrico representando os componentes do traço complexo. Fonte: Adaptado de Taner et al. (1979).

3.1.1 Amplitude instantânea

Amplitude instantânea A(t), também chamada de envelope do traço sísmico, pode ser obtida a partir da equação 4:

$$A(t) = \sqrt{[f^{2}\,(t) + f^{*2}\,(t)] = \,|F(t)|} \quad (4)$$

Analisando a equação 4, oberva-se que a amplitude instantânea equivale ao módulo do traço complexo *F(t)*. Altos valores de amplitude instantânea geralmente estão associados a grandes variações litológicas, ressaltando descontinuidades, limites de sequências, possíveis acumulações de hidrocarbonetos e variações laterais da espessura de camadas (Taner et al. 1979).

3.1.2 Fase instantânea

A fase instantânea $\theta(t)$ ressalta a continuidade lateral de eventos e pode ser obtida a partir da equação 5:

$$\theta(t) = \left[\frac{f^*(t)}{f(t)}\right] \quad (5)$$

Ainda, esse atributo relaciona-se com a o componente da fase de propagação de onda e permite a visualização detalhada de elementos estratigráficos (Taner, 2001). Nos displays de interpretação sísmica (e.g., softwares), a fase correspondente a cada pico, vale ou zero-crossing (mudança de polaridade) do traço real é atribuído é mesma cor, de modo que qualquer ângulo de fase é seguido traço a traço (Taner et al. 1979). Amplitude e fase instantânea estão relacionadas segundo a equação 6:

$$f(t) = A\,(t) \cdot cos\ cos\ \theta \quad (6)$$

3.1.3 Sweetness instantânea

Sweetness $S(t)$ ressalta grandes diferenças de impedância acústica e é derivado da razão entre a amplitude instantânea e a raiz quadrada da frequência instantânea, vide equação 7 extraída de Oliveros & Radovich (1997).

$$S_{(t)} = \frac{A(t)}{\sqrt{\theta(t)}} \quad (7)$$

É caracterizado por realçar a presença de bright spots em reservatórios espessos, visto que a sua resposta sísmica apresenta uma anomalia de amplitude e de baixa frequência. A partir da definição matemática de Sweetness, observa-se que regiões contendo altas amplitudes e baixo conteúdo de frequência apresentarão altos valores de S(t), enquanto em trechos com baixas amplitudes e alto conteúdo de frequência exibirão baixos valores, como, por exemplo de finas camadas de folhelho (Barbosa, 2022).

3.2 Semblance (similarity)

Apesar de não ser classificado como instantâneo, semblance também é um atributo derivado da análise do traço complexo e, assim como a fase instantânea, é um bom indicador da continuidade lateral de eventos. Valores próximos a zero representam defasagem entre traços vizinhos, enquanto valores próximos de 1 indicam elevada continuidade. É definido como a potência da soma dividida pela potência média dos componentes da soma (Taner et al. 1979; Sheriff, 2002). Consequentemente, podemos

calcular o coeficiente semblance (Sc) para uma série temporal complexa a partir da equação 8, extraída de Sheriff (2002).

$$Sc(k) = \frac{\sum_{J=k-N/2}^{k+N/2} \left(\sum_{i=1}^{M} f_{ij}\right)^2}{M \sum_{J=k-N/2}^{k+N/2} \sum_{i=1}^{M} (f_{ij})^2} \quad (8)$$

Na equação 8, f_{ij} é a j-ésima amostra do i-ésimo traço, M é número de canais somados, N é a janela de amostragem centrada em k. Basicamente, o atributo semblance trata-se da energia do empilhamento normalizada pela energia média dos componentes do empilhamento. Isso é equivalente ao valor de defasagem zero da autocorrelação não normalizada do traço somado, dividido pela média dos valores de defasagem zero das autocorrelações dos traços componentes (Sheriff, 2002).

4 MATERIAIS E MÉTODOS

4.1 Banco de dados

Os dados utilizados neste trabalho consistem em um recorte de 715 km^2 no levantamento sísmico migrado em profundidade pós-stack 3D (PSDM) R0276_BS_500_FRANCO_FLORIM_PSDM disponibilizados pela ANP, e perfis de raios gama, densidade, P-sônico e de resistividade de quarenta poços inseridos no Campo de Búzios (tabela 1). O software DUG Insight (v.4.7, 2020) foi usado para visualização sísmica, interpretação e análise dos perfis de poço. As curvas de raios-gama (GAPI), densidade (g/cm^3), perfil sônico (μs/ft) e resistividade (ohm.m) referentes aos 40 poços disponíveis encontram-se nos anexos 1 a 40 desta dissertação.

Tabela 1 - Poços disponibilizados pela ANP e utilizados na etapa de interpretação sísmica. Os seis poços selecionados para a estatística estão destacados em amarelo.

Nome do poço	UWI/API	Elevação Kelly Bush (m)	Elevação Ground Level (m)	Superfície X	Superfície Y	Máxima profundidade medida (m)
1-BRSA-137-RJS	74316019886	18	1,672	-42.55998065814433	-24.51671291317345	3,447
2-ANP-1-RJS	74316024408	25	1,894	-42.49048544076047	-24.62928055532876	5,857
3-BRSA-944A-RJS	74316025644	26	1,862	-42.54103544800331	-24.57843086038591	5,980
3-BRSA-1053-RJS	74316026207	25	2,024	-42.47555682393628	-24.785289901081573	5,905
3-BRSA-1064-RJS	74316026527	32	2,032	-42.46743528575678	-24.69515112492476	9,995
3-BRSA-1184-RJS	74316027143	33	2,011	-42.426693744292955	-24.665332440909335	5,887
3-BRSA-1195-RJS	74316027230	31	1,769	-42.436309377560264	-24.53497634760014	5,870
7-BUZ-6-RJS	74316027807	NaN	NaN	-42.496081159358965	-24.654787636026796	9,995
7-BUZ-10-RJS	74316028876	31	NaN	-42.48676931791169	-24.790950378085835	5,781
7-BUZ-12-RJS	74316028858	32	2,005	-42.4347491506658	-24.660217443537874	6,000
7-BUZ-13DA-RJS	74316028953	32	1,957	-42.47121379631443	-24.668011390731216	3,341
7-BUZ-14-DA-RJS	74316028949	28	2,017	-42.48821649990071	-24.65696040360413	5,845
7-BUZ-14-RJS	74316028923	18	2,018	-42.487723209024	-24.656934101011746	6,000
7-BUZ-17-RJS	74316028972	26	NaN	-42.473671477660226	-24.654369743327184	5,818
7-BUZ-23-RJS	74316029195	25	2,014	-42.475723307793075	-24.776901012656058	6,000
7-BUZ-25-RJS	74316029161	28	18,730	-42.49102509762984	-24.631581569144963	6,000
7-BUZ-29D-RJS	74316029212	32	2,029	-42.48362051922617	-24.792169968830983	5,928
7-BUZ-30-RJS	74316029245	26	NaN	-42.43913885464536	-24.651284741236026	5,906
7-BUZ-31D-RJS	74316029238	25	2,041	-42.479234409440885	-24.671928065650732	5,870
8-BUZ-5-RJS	74316028013	24	1,942	-42.49291016127509	-24.61777637579738	5,930
8-BUZ-9-RJS	74316028837	32	2,032	-42.45926968117557	-24.70418310818524	6,039
8-BUZ-15-RJS	74316028893	25	1,938	-42.46145579945681	-24.640652302794983	6,000
8-BUZ-20-RJS	74316029016	33	2,018	-42.46490570067129	-24.778487163343254	6,084
8-BUZ-21D-RJS	74316029028	33	1,987	-42.417846887373045	-24.659927752583737	5,974
8-BUZ-22D-RJS	74316029035	28	NaN	-42.52977949264656	-24.65280282056695	6,250
8-BUZ-26-RJS	74316029174	33	2,043	-42.47214086668865	-24.801462495482713	7,000
8-BUZ-27D-RJS	74316029193	32	1,958	-42.463044160061614	-24.667097262462935	6,004
8-BUZ-28DA-RJS	74316029281	25	2,061	-42.46955502308596	-24.82557110896927	6,215
8-BUZ-28D-RJS	74316029265	31	2,061	-42.46948643454043	-24.826021225616312	10,000
8-BUZ-32D-RJS	74316029239	25	1,972	-42.42120580122564	-24.65075247156573	3,346
8-BUZ-32DA-RJS	74316029273	26	1,972	-42.42120580122564	-24.65075247156573	6,053
9-BRSA-1159-RJS	74316026869	32	1,955	-42.4600799995	-24.647949999700003	7,000
9-BRSA-1191-RJS	74316027198	28	2,013	-42.4790793832449	-24.660929558780772	9,995
9-BRSA-1197-RJS	74316027235	NaN	NaN	-42.4683046134405	-24.74836304122807	9,995
9-BUZ-1-RJS	74316027546	27	2,022	-42.47831550579738	-24.718212803759656	7,000
9-BUZ-2-RJS	74316027694	31	2,034	-42.46929053802175	-24.791538034727143	6,288
9-BUZ-3-RJS	74316027970	24	2,049	-42.48966404664351	-24.814122768316746	6,135
9-BUZ-4-RJS	74316027752	33	1,912	-42.44966387405744	-24.629701431097995	10,000
9-BUZ-7-RJS	74316028107	26	1,946	-42.51971545034773	-24.62932289649435	6,197
9-BUZ-8-RJS	74316028360	25	2,030	-42.51121449968252	-24.702924036081864	5,850

4.2 Interpretação Sísmica

Para a interpretação de dados sísmicos, é necessário que o intérprete tenha bom domínio da geologia local e regional e das estruturas presentes. Deve-se, principalmente, entender a natureza dos dados para que seja avaliada sua qualidade. Para tal, também é necessário conhecer os objetivos do estudo para que sejam eleitos os procedimentos adequados. Como o dado sísmico por si só possui caráter ambíguo, as interpretações foram embasadas por um extenso estudo regional e local para auxiliar a marcação dos horizontes-chave. Além disso, os dados de poços também serviram como guias para a interpretação.

Como o presente trabalho visa a caracterização tridimensional do arcabouço geológico do Campo de Búzios, o processamento adotado baseou-se na visualização dos dados recebidos da Agência Nacional de Petróleo (ANP), seleção e aplicação de atributos sísmicos que melhor ressaltasse as feições de interesse. Toda a etapa de visualização, tratamento e interpretação dos dados sísmicos foi realizada pelo software DUG Insight (version 4.7, 2020).

De maneira prática, a interpretação foi feita com espaçamento entre as seções entre 500 e 2000 m, segundo a malha exibida na figura 7, cobrindo uma área de aproximadamente 715 km^2 e totalizando 17 inlines e 28 crosslines. Primeiramente, foram traçadas as falhas e, em seguida, os horizontes mais bem marcados, de alta continuidade e alta iluminação. Para traçar os horizontes mais profundos e os pouco contínuos, foi necessária a aplicação dos atributos sísmicos, além do volume sísmico e da análise dos perfis geofísicos de poços.

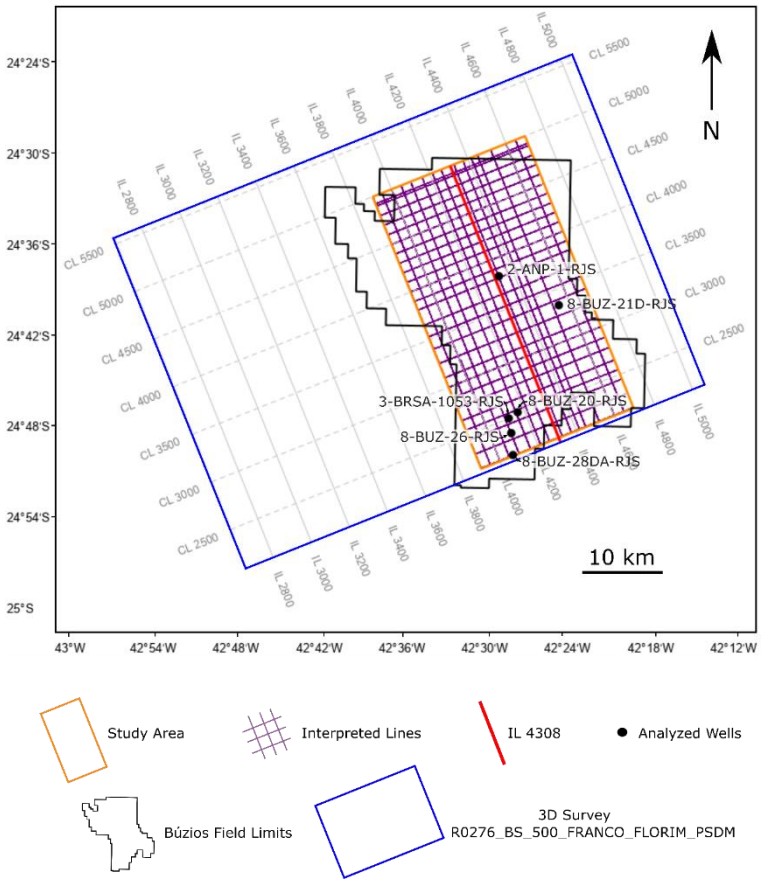

Figura 7 - Mapa de localização da área de estudo e banco de dados utilizados para este trabalho. Fonte: Elaborada pela autora.

4.3 Dados de poços

Uma vez processados os dados sísmicos, iniciou-se a etapa de tratamento e entendimento dos dados de poços. A grande maioria dos perfis de poços recebidos encontram-se no formato DLIS (*Digital Log Interchange Standard*), que é incompatível com o software utilizado. Portanto os perfis foram convertidos do formato DLIS para LAS (*Log ASCII Standard*) utilizando a ferramenta Schlumberger Log Data Toolbox (Toolbox 2.3, 1999-2007). Após esse procedimento, inciou-se a etapa da padronização das curvas de interesse, ajustando a classe de cada curva, escala dos tracks, cores, entre outras. As curvas analisadas foram de densidade (g/cm^3), raios gamma (GAPI), perfil sônicos P (µs/ft) e resistividade (ohm.m).

A priori, o principal critério para seleção dos poços foi a amostragem vertical, de modo que as curvas cobrissem o maior intervalo possível em profundidade. Em segundo lugar, foi a disponibilidade de perfil composto e, por último, a distribuição geográfica, de modo a cobrir lateralmente toda área de estudo. Dessa forma, dos quarenta poços

disponíveis, seis foram selecionados: 2-ANP-1-RJS, 3-BRSA-1053-RJS, 8-BUZ-20-RJS, 8-BUZ-21D-RJS, 8-BUZ-26-RJS e 8-BUZ-28DA-RJS (Fig. 7).

Os perfis dos poços selecionados foram processados por um tratamento estatístico básico disponível no próprio software de interpretação sísmica DUG Insight (version 4.7, 2020). Neste tratamento, foram calculados os valores máximo, mínimo, média simples e desvio padrão das curvas no intervalo de cada uma das unidades sísmicas descritas.

4.4 Interpolação dos horizontes

A interpolação tridimensional dos horizontes interpretados foi realizada a partir do software DUG Insight. O interpolador do programa preenche o espaço entre as seções interpretadas de acordo com o algoritmo de espalhamento *natural neighbour* (tesselação de Voronoi) segundo a equação 9, extraída de Sibson (1981):

$$G_{(x)} = \sum_{i=1}^{n} \quad w_i(x) f(x_i) \text{ (9)}$$

Na equação 9, $G_{(x)}$ é a estimativa no ponto x, onde w_i são os pesos e $f(x_i)$ são os dados conhecidos no ponto (x_i). Os pesos, w_i, são calculados encontrando quanto de cada uma das áreas circundantes é "roubada" ao inserir x na tesselação. O algoritmo *natural neighbour* consiste em uma interpolação espacial baseada na tesselação de Voronoi, em que é feita a partição de um plano em regiões próximas entre si de um conjunto dado de objetos. No caso mais simples, esses objetos são apenas um número finito de pontos no plano (chamados de sementes, locais ou geradores). Para cada semente, há uma região correspondente, chamada célula de Voronoi, composta por todos os pontos do plano mais próximos dessa semente do que de qualquer outra (Sibson, 1981).

Outros parâmetros utilizados na interpolação são:

a) Strike/dip (peso na direção do strike): 1
b) Direção: 0
c) Raio de busca: 2000 m.

5 DESENVOLVIMENTO E RESULTADOS

5.1 Resultados

A aplicação dos atributos foi de suma importância da identificação de padrões sísmicos, uma vez que apenas a amplitude sísmica não foi capaz de discriminar todas as unidades posteriormente descritas. A partir da interpretação de 45 seções sísmicas, juntamente com os atributos amplitude, fase e sweetness instantâneos e semblance (similarity), disponíveis no software DUG Insight, foram individualizados seis grupos distintos, com características bem marcadas e denominadas unidades A, B, C, D, E e F, que ocorrem em toda a região de estudo. Posteriormente, tais unidades foram associadas respectivamente às fases tectônicas Sin-Rifte I, Sin-Rifte II, Pós-RiftE I, Pós-Rifte II, Drifte I e Drifte II, respectivamente. Todos os resultados e discussões serão apresentados no item subsequente (4.2) sob a forma de artigo científico. Os resultados referentes à estatística dos poços 2-ANP-1-RJS, 3-BRSA-1053-RJS, 8-BUZ-20-RJS, 8-BUZ-21D-RJS, 8-BUZ-26-RJS e 8-BUZ-28DA-RJS serão apresentados nos Apêndices A a G deste volume.

5.2 Artigo submetido

Three-dimensional characterization of the Búzios Field reveals implications on the tectonostratigraphic evolution of the Santos Basin using combined seismic attributes and well-logs analysis

ABSTRACT

The Búzios Field is one of the most prolific petroleum fields along the Eastern Brazilian Margin. Despite significant research conducted restrictedly on the pre-salt reservoirs, few studies have focused on the three-dimensional characterization of the entire Búzios Field area. Therefore this work aims to spatially characterize a volume along the Búzios Field area using 3D seismic volume interpretation, seismic attributes, and well-log data. The combined use of these tools allowed the understanding of several parameters concerning the tectonostratigraphic evolution of the Santos Basin. Within the mapped area, we identified five units: Syn-Rift I, Syn-Rift II, Post-Rift I, Post-Rift II, Drift I, and Drift II. The 3D model reveals significant features such as the depth variation of the Syn-Rift I unit and the heterogeneous morphology of the Post-Rift II unit. The Syn-Rift I unit is deeper towards the N-NW and shallower towards the S-SE due to a regional half-grabens system. This system impacts the pre-salt geometry and thickness, as structural highs and lows are relevant factors in sediment accommodation. The Post-Rift I unit has a predominantly regular geometry and thickness but tends to thicken towards the S-SE and exhibits slight downward flexure towards the NE in the southeast of the Búzios Field. In three dimensions, the heterogeneous morphology of the Post-Rift II unit is evidenced by the variable thickness and irregular topography, accounting for the intense halokinesis in the Santos Basin. Above the evaporitic layer, the thickness of the Drift I unit is highly conditioned by salt morphology, with thicker and deformed packages in areas of thinner salt section. On the other hand, the Drift II unit shows relatively constant thickness with minor variations near fault zones. Comparisons with other fields within the Santos Basin (Tupi and Sapinhoá/Lapa) reveal differences in layer thickness, mobilization, and rotation of the syn-rift blocks. The Post-Rift I layer (Barra Velha Fm.) and the Post-Rift II package (Ariri Fm.) are thinner and less mobilized in the Búzios Field area. Moreover, the syn-rift blocks are less rotated, and the internal reflectors have a lower inclination in the study area when compared to these other fields. Therefore, this research concludes that the lower mobilization of salt, the lower thickness of the post-rift package, and the minor syn-rift block rotation observed in the Búzios Field area are associated with the relative

distance from the continental margin and, consequently, with the amount of displacement generated by the South Atlantic Rift. In this case, the Búzios Field is located in a more proximal portion than Tupi and Sapinhoá/Lapa fields, exhibiting features suggestive of a lower displacement.

KEYWORDS: Seismic characterization, Tectonic evolution, Rift basins, Santos Basin, Búzios Field

5.2.1 Introduction

The exploration of petroleum in the eastern Brazilian margin basins has gained great expression over the last 50 years, especially after the start of hydrocarbon production in the Campos Basin in the late 1970s (Pereira and Macedo, 1990). In the 1970s, some projects led to a systematic investigation of the offshore sedimentary basins using geophysical data. The interpretation was based on geological data (mainly stratigraphical results of exploratory wells drilled by Petrobras) and majorly seismic and potential field data to support the interpretation of the tectonic-sedimentary architecture of the several segments along the continental margin (Mohriak & Fainstein, 2012). Between the mid-1970s and the mid-1980s, the Campos Basin was established as an important oil producer. However, due to the second oil crisis and the need to increase domestic production, it was necessary to search for new petroleum sources. In 1980, the first occurrence of oil stored in turbidite sandstones, in the post-salt section, was registered in the Santos Basin (Fig. 1). In 2005, the discovery of a carbonate reservoir in the deep pre-salt succession at the south portion of the basin increased the expectation of a great oil producer (Chang et al. 2008; Souza & Sgarbi, 2016; 2019). However, characterizing deep water features can be defiant because the mineralogical composition and diagenetic processes can interfere with variations in pore shape and interconnectivity, thus exerting a high influence on the elastic properties of carbonate rocks (Dias et al. 2019).

As a result of the pre-salt discovery in 2005, the Santos Basin gained significant attention and became the focus of numerous studies to support oil and gas exploration. Souza et al. (2007) associated the presence of transversal structures in the north portion of the basin with possible transfer faults by combining 2D seismic, gravity, and magnetic data, integrated with well logs. Assine et al. (2008) defined the depocenter migration of the stratigraphic sequences using seismic sections and well logs, showing how the salt tectonics is intimately related to the evolution of the Neo-Cretaceous progradational

clastic wedges and, consequently conditioning the hydrocarbon migration of the post-salt section in the Santos Basin. Halokinesis also play an important role in controlling the structural styles of petroleum systems. In the Santos Basin, the investigation of the interplay between salt and sediment integrating seismic interpretation, kinematic restoration, and analog modeling led to the conclusion that differential loading was the main driving mechanism to trigger halokinesis (Guerra & Underhill, 2012).

In addition to the seismic interpretation, sedimentary analysis is also performed based on integrating sidewall core samples and well logs. The seismic patterns discrimination is used to characterize the tectonic and depositional evolution of the Barra Velha Formation in a sector of the Outer High of the Santos Basin, leading to the definition of shallowing and flooding upwards cycles responsible for the pre-salt reservoirs deposition (Neves et al. 2019).

Regarding the Búzios Field (Fig. 1), Castro & Lupinacci (2019) proposed a flow of characterization of the pre-salt carbonate reservoirs from well logs aiming to evaluate the Barra Velha and Itapema formations by rock physics crossplots. In this work, the authors also propose segmenting the rift-sag phase into Lower Sag and Upper Sag. Modeling the distribution of petrophysical properties of a reservoir assists in the spatial characterization of these complex deposits. Thus, a model-based inversion of seismic data into an acoustic impedance volume was applied to the evaluation of the relationship between acoustic impedance and porosity showing trends related to Mg-clays contends in the Búzios Field reservoir (Dias et al. 2019).

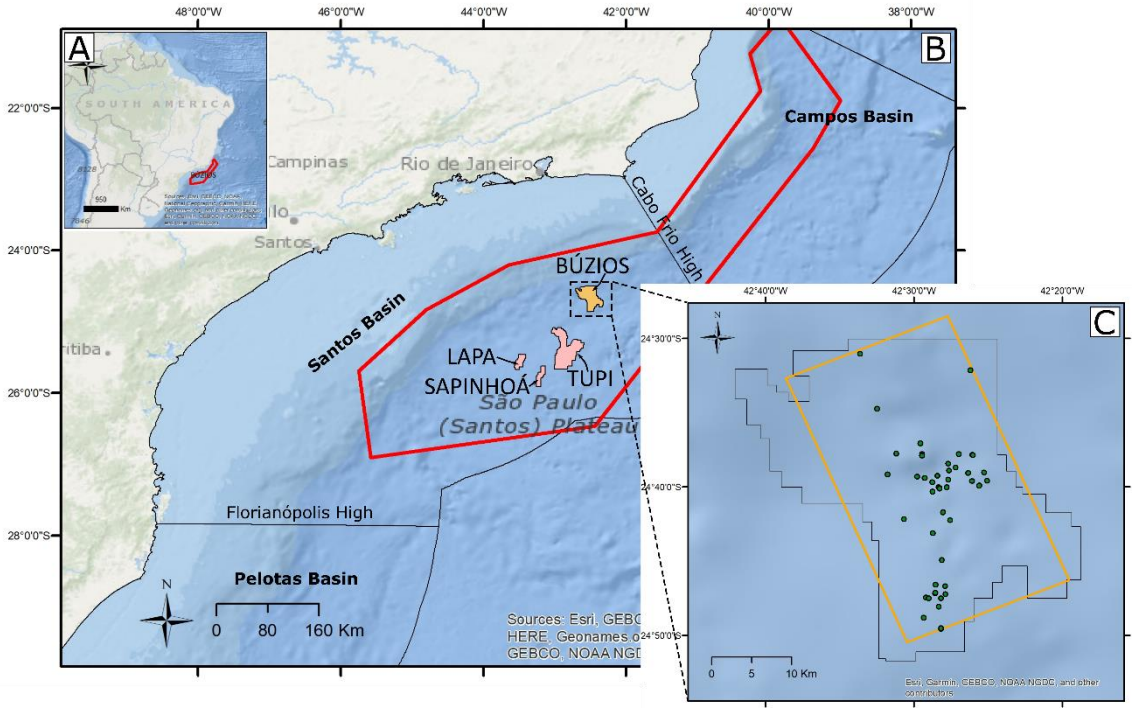

Figure 1 - A) Location of the Búzios Field in the context of South America. The red polygon delimitates the pre-salt limits. B) Location of the Búzios, Tupi, Sapinhoá, and Lapa fields. C) Location of the study area. The orange polygon delineates the study area. Green dots represent the public well-logs available from ANP.

Seismic attributes are important to assist the subsurface interpretation from seismic data and are defined as any measure of seismic data that helps us visually enhance or quantify features of interpretation interest (Chopra & Marfurt, 2007). In a general sense, this definition encompasses all quantities extracted from seismic data by calculations, such as impedance inversion and pore -pressure prediction. The application of seismic attributes is widely used in the characterization of a petroleum reservoir. Thus, these attributes aim to provide accurate and detailed information to the interpreter on structural, stratigraphic, and lithological parameters of the seismic prospect (Taner, 2001; Chopra & Marfurt, 2007).

Summarily, according to Brown (2011), time-derived attributes provide structural information, and amplitude-derived attributes provide stratigraphic and reservoir information. Frequency-derived attributes are poorly understood, however, they could provide additional useful stratigraphic and reservoir information. Attenuation can yield information on permeability. Hybrid attributes are a combination of amplitude and frequency information. Each of these attributes relates to each other, where some attributes have a particular sensitivity to the nature of the reservoir and several others are

better at presenting information or subsurface anomalies that were not initially identified by the conventional data or materials as an indicator of the presence of hydrocarbons (Abdullah et al. (2005) in Pamungkas et al. 2021). In this context, the attributes defined as “instantaneous” are computed sample by sample, and represent instantaneous variations of several parameters. Instantaneous values of attributes such as trace envelope, its derivatives, frequency, sweetness, and phase may be determined from complex traces (Taner, 2001). The calculation of the instantaneous attributes is based on the conversion of the real-valued input traces into complex-valued traces based on the Hilbert transform. The output of this operation is amplitude ("waveform envelope" or absolute value of the analytic signal), phase (the argument of the complex-valued trace), frequency (the scaled time derivative of the instantaneous phase), and sweetness (instantaneous amplitude divided by the square root of instantaneous frequency) (DUG, 2020).

Multi-attribute analyses have been used to characterize pre and post-salt petroleum systems. For example, Silva (2012) applied seismic attributes (instantaneous frequency, RMS amplitude, integrated trace, cosine phase, and amplitude envelope) combined with well data and the inversion techniques for the delimitation and the characterization of a complex reservoir system from the tertiary turbidite channels located in the Lower Basin of Congo. Artificial intelligence can also support the use of seismic attributes in reservoir identification and prediction of the environment of deposition. Obafemi et al. (2020) integrated two lithofacies and fluid-discriminating seismic attributes via an unsupervised artificial neural network to characterize the architecture of deepwater turbidite channels and submarine fan lobes across a hydrocarbon-bearing reservoir within the Frem Field in the Niger Delta. Souza (2021) characterized the southeast portion of the hydrocarbon producer basin of Taranaki, New Zealand. This research is anchored in two independent attributes: curvature and coherence, which proved efficient in delineating structural and stratigraphic discontinuities, such as channels, faults and fractures, and seismic facies. The use of multi-attributes enhances and accelerates the process of seismic interpretation.

In the Campos Basin, Schmidt (2013) employed Maximum Amplitude, Maximum Magnitude e RMS Amplitude to characterize the carbonatic reservoir of the Bonito Field. Considering the heterogeneous carbonatic rocks from the Brazilian pre-salt layers, the amplitude attributes provided the most distinguishable seismic response. To the south of the Santos Basin, the use of instantaneous seismic attributes such as envelope, phase, and

instantaneous frequency has facilitated the interpretation of 2D post-stack seismic sections, leading to the identification of gas hydrate indicators in the Pelotas Basin (Dias et al. 2019).

In the central part of the Santos Basin, multiple seismic attributes combined with machine learning algorithms are used to identify stratifications within the salt layer, showing that the correct facies identification allows adjusting the drilling parameters accordingly to the estimated salt type, minimizing operational problems and economic losses (Mesquita et al. 2021). Ferreira et al. (2021) propose using an unsupervised artificial neural network algorithm to perform seismic facies classification in the Búzios Field. This research was based on a unique combination of stratigraphic and structural attributes: local flatness, principal dip component, acoustic impedance, and RMS amplitude. The latter two attributes were essential for the delimitation of the carbonate platform facies, while the first and second ones were essential to discriminate the debris and build-up facies.

As the vast majority of recent studies focus solely on the reservoir of the Búzios Field, there is a noticeable lack of published research concerning the stratigraphic, geometric, and spatial relationships of the other units that comprise the geological framework of this area. Therefore, this research aims to address this gap by examining the comprehensive geological framework of the region, encompassing various units and their interconnections. This broad approach will contribute to a more thorough understanding of the geological evolution and potential reservoir characteristics in the Búzios Field area. In this case, this study proposes a three-dimensional investigation of the features observed throughout the geological framework of the basin in the Búzios Field area. In this paper, I propose a quantitative and qualitative classification of seismic facies using multi-attribute analysis allied to the integration of well logs in the Búzios Field to characterize three-dimensionally the geological framework of the area within the Santos Basin. The study aims to reconstitute the basin's tectonostratigraphic evolution in the context of the South Atlantic Ocean opening by unraveling the relationship between the geological units and its seismic response. Furthermore, my work intends to three-dimensionally characterize the Búzios field area, relating its observed features with the evolution of the Santos Basin. This research has the potential to contribute to the future development of more concise, predictive, and detailed geological models for oil exploration in the basin.

5.2.2 Location and Geological Framework

The Santos Basin (Fig 1) is a passive margin basin related to the Gondwana breakup event during the Neocominian. The tectonic evolution of this basin is divided into three mega-sequences: rift, post-rift (sag), and drift presented in Figure 2 (Mio et al. 2005; Moreira et al. 2007). The Camboriú, Piçarras, and Itapema formations represent the rift stage, related to the separation of South-American and African paleocontinents during the end of Neocomian and the beginning of Aptian and are responsible for initiating the lacustrine deposition (Moreira et al. 2007).

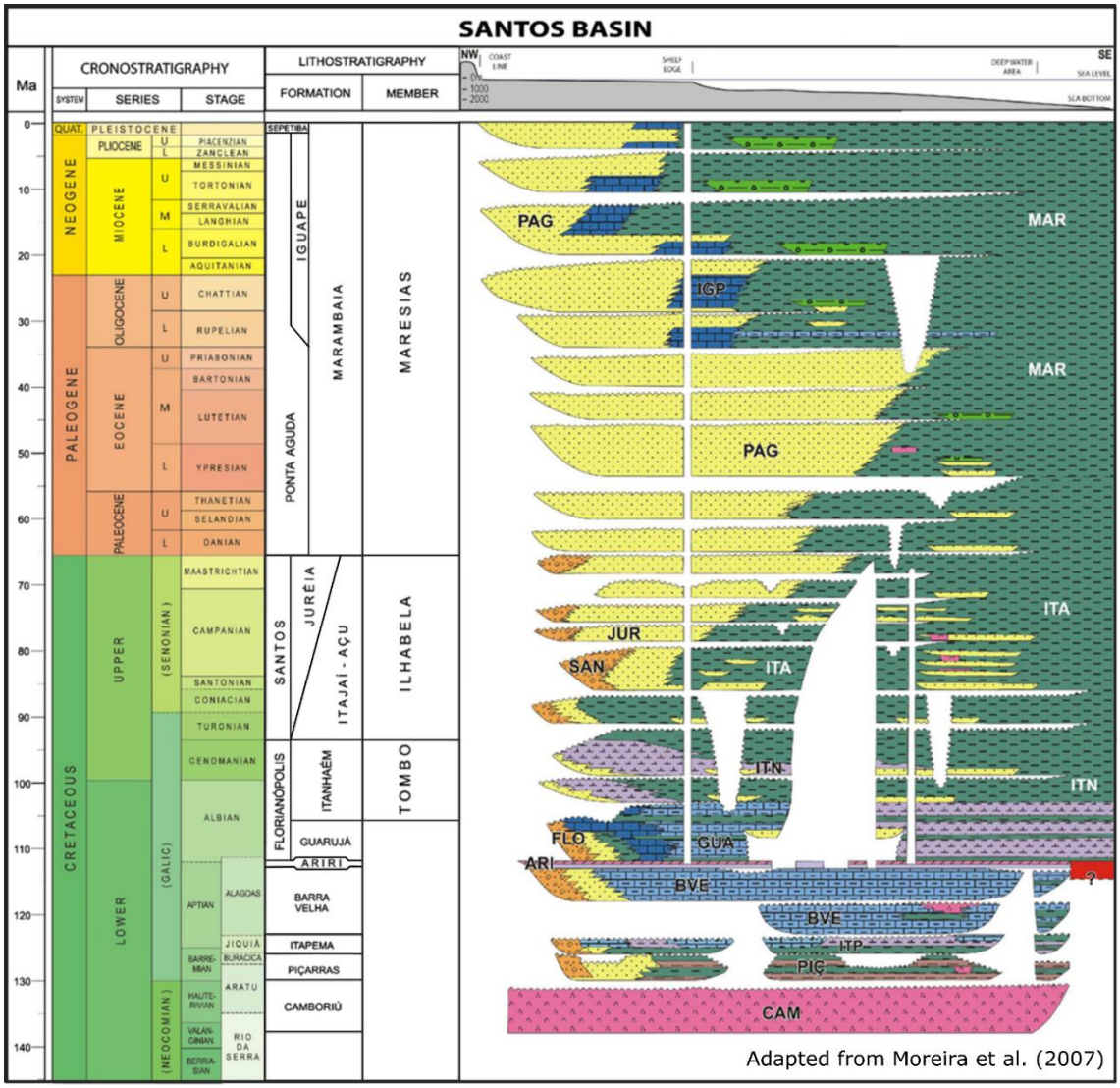

Figure 2 - Simplified stratigraphic chart for Santos Basin. Adapted from Moreira et al. (2007) in Arai & Viviers (2013).

The post-rift or sag sequence represents a transitional stage from continental to marine environment with softer tectonics during the Aptian (Moreira et al. 2007). This transitional stage is represented by the non-marine and shallow-water carbonates of the

Barra Velha Formation and the thick overlying evaporite seal of the Ariri Formation (Buckley et al. 2015).

The last phase of the Santos Basin evolution is the continental drift, responsible for the installation of a well-established basin associated with the opening of the Atlantic Ocean since the Albian (Moreira et al. 2007). This mega-sequence is related to thermal subsidence associated with halokinesis and is subdivided into three sequences deposited during a progressive increase of the basin depth: the Camburi, Frade, and Itamambuca groups. The first one is a result of the rising sea level and is represented by the lower Florianópolis, Guarujá, and lower Itanhaém formations. The Frade Group represents a marine regression stage where the shelf boundary has advanced up to 200 km offshore. The end of the drift phase is marked by the prograding system of the Itamambuca Group with expressive development of clinoforms of slope and the advance of the platform break-up (Milani et al. 2000; Moreira et al. 2007; Papaterra, 2010).

The Búzios Field, located in the central portion of the Santos Basin (Fig. 1), is one of the most productive fields in the area. In the Búzios Field area, the rift mega-sequence begins with the extrusion of the Camboriú Formation continental basalts, which are interlayered with volcaniclastic rocks, as shown in composite log registers (3-BRSA-1053-RJS). The rift mega-sequence is heavily influenced by tectonics and is divided into upper and lower sequences. The lower sequence is characterized by the Piçarras Formation, which exhibits the greatest development of sedimentary wedges with thickening towards the hanging wall, reaching thicknesses of up to 2,200 m. The upper sequence corresponds to the Itapema Formation, which includes the "coquinas section", consisting of a thick package (up to 300 m) of bivalve rudstones and, to a lesser extent, bioclastic grainstones, packstones, wackstones, mudstones, and shales that were deposited in high-energy environments (Tavares dos Santos & Gordon, 2021).

Regarding the post-rift mega-sequence, the carbonates of the Barra Velha Formation in the Búzios Field occur in various facies, such as Mg-rich clays (stevensite), shrubs, spherulites, and fine-grained carbonate muds. These carbonates range in thickness from approximately 200 to 400 m at structural highs (Tavares dos Santos & Gordon, 2021; Ferreira, 2022). The basal and upper portions of the Barra Velha Formation are dominated by fine-grained carbonate mud sediments, while the middle is dominated by in-situ carbonate sedimentation, with shrubs and spherulites (Ferreira, 2022). The salt structures of the Ariri Formation reach thicknesses of up to 2,650 m in the central portion

of the Búzios Field, with decreasing thickness towards the north and south, forming salt windows (or scars). The stratification of evaporites begins with the precipitation of anhydrite at the base, followed by a thick package of halite, which is the most common evaporite deposit (Tavares dos Santos & Gordon, 2021).

The drift mega-sequence in the Búzios area begins with thin microbial carbonate deposits of the Guarujá Formation, which consists mainly of fine-grained carbonates (mudstone and calcilutite) deposited in distal restricted marine conditions with typical thicknesses ranging from 10 to 30 m. Overlying the Guarujá Formation, the Itanhaém Formation is composed of marls and intercalated shales, with a local expression in the vicinity of the 3-BRSA-1053-RJS well. Composite logs (3-BRSA-1053-RJS, 3-BRSA-1064-RJS) reveal thick layers of sandstone interleaved with shales and minor marls from the Itajaí-Açu Formation, exhibiting a coarsening-up sequence up to 430 m thick. The Marambaia Formation, which consists of a thick package (approximately 650 m) of shales and sandstones, was deposited in open marine conditions from Eodanian to recent times (Moreira et al. 2007). Structurally, the post-salt deposits in the Búzios area are fully controlled by halokinesis (Tavares dos Santos & Gordon, 2021).

The pre-salt petroleum system of the Búzios Field is composed of the source shales of the Piçarras Formation, while the reservoir rocks are encompassed by the coquinas from the Itapema Formation and the Barra Velha carbonates. The evaporitic cover of the Ariri Formation works as the seal of the system, while the whole drift mega-sequence consists of the overburden (Chang et al. 2008).

5.2.3 Methods and Materials

The Búzios field is covered by 2,586 km^2 of 3D post-stack depth migrated seismic (PSDM) and there are gamma-ray, density, P-sonic, and resistivity logs from thirty-seven wells (Fig. 3). Our work focused on 715 km^2 of the 3D PSDM seismic and six wells, with depth interval from 2,000 to 9,995 m.

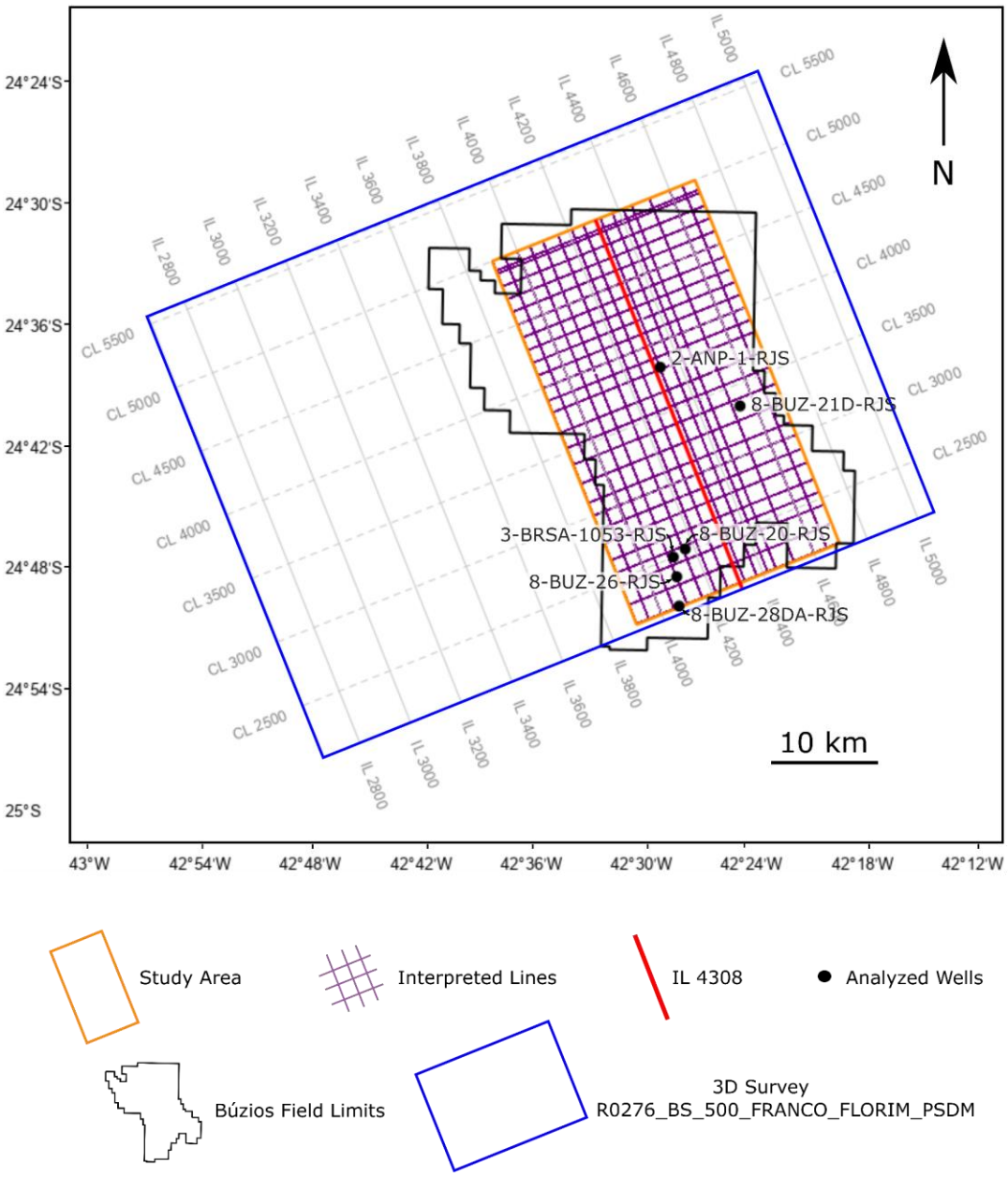

Figure 3 - Location map of the study area and dataset used for this work.

5.2.3.1 Seismic Interpretation

I interpreted five key horizons and the main faults in a grid of 17 inlines and 28 crosslines with spacing varying from 500 m to 2,000 m (Fig. 3). I first traced the faults, then the well-marked horizons with high continuity and high illumination, supporting on the well data. To trace the deepest and the less continuous horizons, it was necessary to use seismic attributes in addition to the seismic images and logs. The attributes used in this work are described below:

- Instantaneous amplitude: attribute sensitive to major lithologic changes and lateral variations in bed thicknesses. It was extracted using the method of complex trace analysis proposed by Taner et al. (1979);
- Instantaneous phase: physical attribute and can be effectively used as a discriminator for geometrical shape classification which works as a good indicator of lateral continuity (Taner, 2001). It can be calculated as proposed by Taner et al. (1979);
- Instantaneous sweetness: highlights large differences in acoustic impedance and is highly sensitive to frequency variation. The attribute was calculated by the ratio instantaneous amplitude over the square root of instantaneous frequency, according to Oliveros & Radovich (1997);
- Semblance (similarity): geometrical attribute which is also used as a good indicator of lateral continuity and bedding similarity (Taner, 2001). It was obtained by the equations presented by Marfurt et al. (1998).

5.2.3.2 Well-log Analysis

Data from forty well logs were organized, processed, and standardized. Most of the available well logs are in DLIS format (Digital Log Interchange Standard), which is incompatible with the software used. Therefore, the profiles were converted from DLIS to LAS (Log ASCII Standard) format. The next step was to standardize the density (g/cm^3), gamma-rays (GAPI), P slowness (μs/ft), and resistivity (ohm.m) curves. They were unified and the class, scale of tracks, and colors of each curve were adjusted.

Six of the forty available well logs were selected to be analyzed (Fig. 3). A priori, the main criteria for wells' selection was vertical sampling so that the curves covered the greatest possible interval in depth. Secondly, it was the availability of a composite profile. In this way, the selected wells were 2-ANP-1-RJS, 3-BRSA-1053-RJS, 8-BUZ-20-RJS, 8-BUZ-21D-RJS, 8-BUZ-26-RJS, and 8-BUZ-28DA-RJS. The curves were processed by a smoothing filter which uses the method of a trimmed mean of the middle N values in the window, where N is the window trimmed by 25%, i.e. the average of the middle 75% of the values, excluding the upper 12.5% and lower 12.5% of the sorted values. The statistical analysis consists of a calculation of maximum and minimum values, the average mean, and the standard deviation of the four curves in the interval of each key seismic unit described in the following section.

5.2.4 Results

My work results are categorized into four sections as described below: seismic pattern identification, analysis of identified structures, well-log analysis, and creation of a three-dimensional model.

5.2.4.1 Recognition and Classification of the Seismic Patterns (Seismic Facies)

To better understand the three-dimensional framework and tectonostratigraphic evolution of the Santos Basin, six seismic units were identified with distinct characteristics throughout the study area (Fig. 4). These units, designated as A, B, C, D, E, and F, were differentiated using the well logs, the seismic amplitude analysis and the instantaneous amplitude, phase, sweetness, semblance (similarity) volumes.

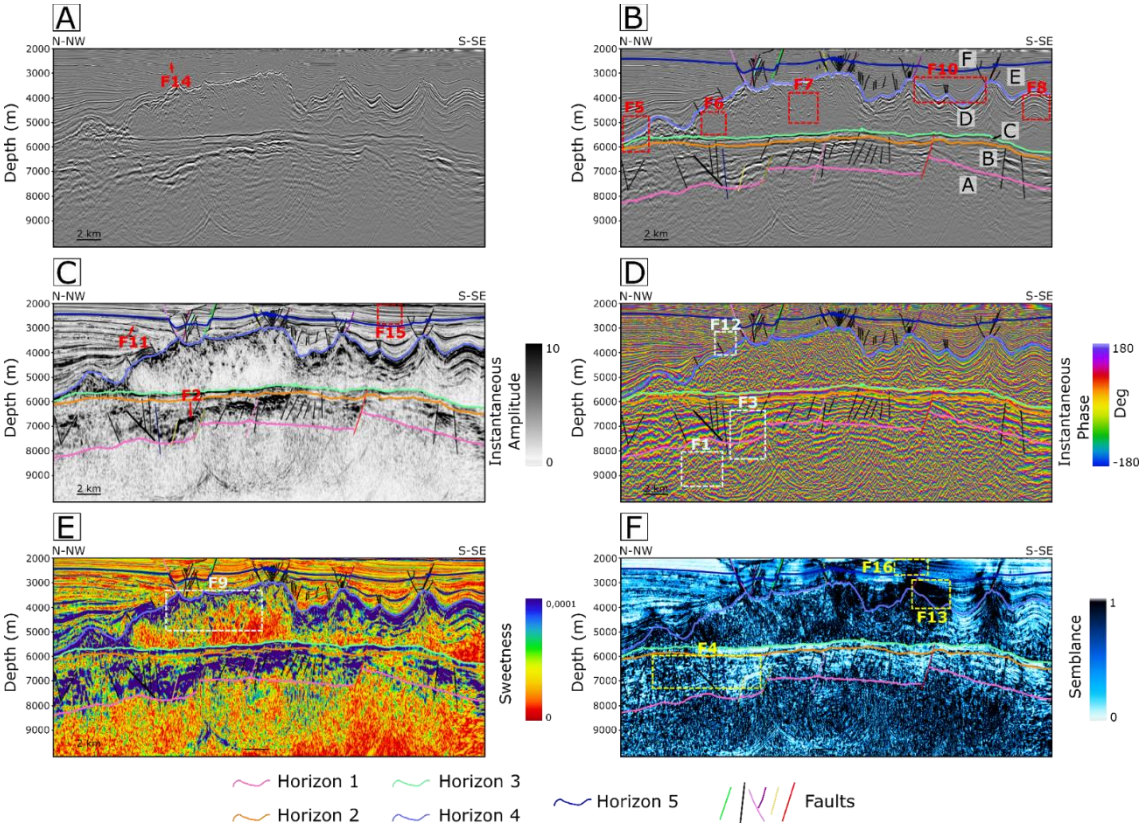

Figure 4 - Results of the seismic interpretation of IL 3408. A) Non-interpreted and B) interpreted seismic line (IL3408). C) Instantaneous amplitude, D) instantaneous phase, E) instantaneous sweetness, and F) attributes for IL4308 are also presented. The dotted boxes highlight important features (F1 to F16) described in the text. Letters A, B, C, D, E, and F refer to the interpreted units.

Unit A is topped by horizon 1 (depicted in pink in Figure 4), which occurs below approximately 5,600 m (with an average depth of 7,500 m). The contact with the overlying Unit B can be either tectonic when the unit is disrupted by normal faults or a lithological unconformity. This unit is mainly characterized by weak or absent reflectors

that lack continuity and illumination, making it challenging to define its boundaries. Consequently, the use of seismic attributes is crucial for accurate delineation (Fig. 4-A and B). The instantaneous amplitude attribute shows a homogeneous white pattern, suggesting a massive composition (Fig. 4-C). The most effective attribute for discriminating Unit A is the instantaneous phase, which reveals a chaotic pattern indicating a lack of lateral continuity (Feature 1 in Fig. 4-D). However, defining the top of this unit posed significant challenges due to the limited seismic resolution at great depths. The instantaneous sweetness attribute indicates values near zero, suggesting the absence of notable structures or lithologic variations (Fig. 4-E). Finally, the semblance attribute displays a dark pattern, indicating high dissimilarity with the surrounding area (Fig. 4-F).

Horizon 2 (shown in orange in Figure 4) delineates the upper boundary of Unit B. This surface occurs between 5,460 m and 7,280 m (with an average depth of 5,950 m). Unit B is characterized by reflectors that range from divergent or oblique parallel to locally chaotic at the footwalls' base, with high amplitude, medium to low illumination, and intermediate lateral continuity (Fig. 4-A and B). It displays a wedge-shaped geometry. In areas where the horsts of Unit A are located, there is a decrease in layer thickness.

Regarding seismic attributes, the instantaneous amplitude does not exhibit a well-defined pattern, but dark features parallel to the base of the unit (horizon 1) are observed, interleaved with a white chaotic region (Feature 2 in Fig. 4-C). The instantaneous phase attribute distinguishes units A and B well, with a change from a chaotic pattern to a divergent and oblique parallel one that evidences good lateral continuity of the reflectors (Feature 3 in Fig. 4-D). Unit B predominantly displays high sweetness (in dark blue) with minor intercalations of low sweetness (in yellow to red) parallel to the top of the unit (horizon 2, Fig. 4-E). Semblance is predominantly high and highlights the reflectors' divergent pattern and inclination (Fig. 4-F).

Unit C is bounded at the top by horizon 3 (shown in green in Figure 4), which occurs between 5,180 m and 6,600 m (with an average depth of 5,700 m). This unit is separated from Unit B by a significant discontinuity, which marks the change in the divergent pattern to a planar-parallel one (Fig. 4-A and B). The surface used as the base marker is a horizon with very high illumination and negative amplitude, where an

onlapping feature is observed. Another important feature is the occurrence of mounds at the top of the unit.

Instantaneous amplitude and sweetness do not provide a clear response for this unit, resulting in a highly homogeneous pattern (Fig. 4-C and E). The instantaneous phase shows a discrete change in pattern compared to Unit B, marked by an increase in bed thickness expressed by the increase of the distance between two consecutive reflectors (Fig. 4-D). Semblance exhibits a gradual change from planar-parallel white to chaotic dark-blue/black patterns toward the N-NW. The white portion of high similarity indicates a homogeneous composition, while the dark portion indicates abrupt structural variation (Feature 4 in Fig. 4-F).

The top of Unit D is marked by Horizon 4 in blue in Figure 4. This horizon ranges in depth from 2,490 m to 6,330 m, with an average depth of 3,550 m. The thickness of this unit decreases towards the NW, resulting in direct contact between units C and F (Feature 5 in Fig. 4-B). The seismic response of this unit is highly heterogeneous, displaying three main patterns: without stratification (Feature 6 in Fig. 4-B), with little marked stratification (Feature 7 in Fig. 4-B), and with well-marked stratification (Feature 8 in Fig. 4-B). The deepest domain lacks stratification and has chaotic to absent reflectors. The intermediate domain typically exhibits a chaotic to wavy seismic pattern with weak stratification, while the shallowest domain has well-marked stratification characterized by wavy to plane-parallel reflectors, high amplitude, high illumination, and low lateral continuity. Generally, the stratification of this unit is parallel to the irregular surface of the top.

Instantaneous amplitude strongly emphasizes Horizon 5, revealing a well-marked dark surface indicating an abrupt lithologic variation (Fig. 4-C). This attribute also confirms the existence of a stratified portion at the top of Unit D, as shown by the alternation of wavy dark and light regions. The domain without stratification is marked by a relatively homogeneous white pattern, resulting in low amplitude envelope values. The instantaneous phase attribute effectively highlights the domain without stratification due to its chaotic pattern and lack of continuity (Fig. 4-D). The domain with well-marked stratification displays intermediate to good lateral continuity. Instantaneous sweetness highlights a chaotic pattern with low to medium sweetness in the center of Unit D, contoured by layers with high sweetness parallel to Horizon 4 (Feature 9 in Fig. 4-E).

Semblance provides visualization of stratified areas adjacent to the top, highlighted by light-blue to white segments in the flanks of antiforms and black in the hinges (Fig. 4-F).

Horizon 5 (dark blue in Figure 4) marks the top of Unit E, which ranges in depth from 2,910 m to 4,290 m, with an average depth of 3,290 m. This unit displays a heterogeneous seismic pattern, characterized by intermediate amplitude and illumination but high lateral continuity (Fig. 4-A and B). Near the base, the reflectors tend to follow the underlying unit topography and fill mini-basins between the Unit D domes (Feature 10 in Fig. 4-B). In these regions, the unit exhibits a wavy pattern with onlapping terminations, where reflectors are thick at the depocentre and thinner as it moves away from the center. On the steepest slopes, Unit E has a chaotic pattern, while towards the top, the reflectors are plane-parallel. Interweaved mound-like features with wavy to plane-parallel internal reflectors (Figure 5) occur in the north portion of the study area. The unit is generally intensely deformed and crossed by multiple sets of normal faults.

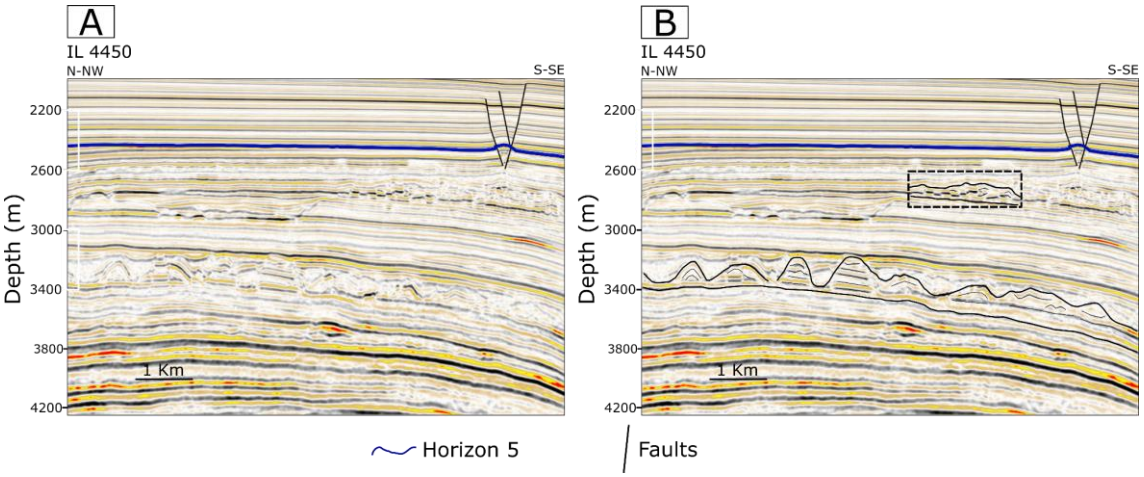

Figure 5 - A) Non-interpreted, and B) Interpreted seismic section showing the mound-shaped features observed in units E and F, exhibiting a wavy to a plane-parallel internal pattern.

The instantaneous amplitude attribute reveals the existence of some expressive surfaces marked by black color parallel to the unit stratification and a mound-shaped feature in the north (Feature 11 in Fig. 4-C). The instantaneous phase attribute effectively enhances the wavy to plane-parallel pattern and high lateral continuity of the reflectors. Next to the base of the hanging walls, this attribute shows a chaotic pattern (Feature 12 in Fig. 4-D). Sweetness shows the intercalation of thick layers of high, medium, and low sweetness at the top and a heterogeneous pattern composed of medium to low sweetness where the mound-like features occur (Fig. 4-E). Semblance also reveals the plane parallel

and wavy patterns, but it highlights little disruption marked by dark patches into the medium to high semblance reflectors (Feature 13 in Fig. 4-F).

Seismic unit F is characterized by a parallel configuration, with well-marked flat reflectors that exhibit a plane-parallel configuration, high illumination, low amplitude, and high lateral continuity (Fig. 4-A and B). It differs from the underlying unit E by the intensity of deformation. An important feature observed throughout the study area is an erosive surface at the top of Unit E at depths lower than 2,500 m (Feature 14 in Fig. 4-A). This surface is curved and locally undulated and is marked by an abrupt disruption of reflectors.

The instantaneous amplitude attribute better discriminates between units E and F, with the latter presenting a homogeneous plane-parallel pattern marked by alternating high (black), medium (grey), and low (white) reflectivity. This attribute also reveals the great lateral continuity and relatively constant thickness of layers (Feature 15 in Fig. 4-C). The instantaneous phase attribute highlights the great lateral continuity and distinguishes units E and F by the decrease of reflector thickness in the latter (Fig. 4-D). Moreover, sweetness shows a distinct intercalation of thin layers of high, medium, and low sweetness (Fig. 4-E). Semblance outlines the plane-parallel pattern predominantly formed by white layers (high similarity), with some dark areas around faults and structural highs of Unit D (Feature 16 in Fig. 4-F). Figure 6 summarizes the six aforementioned seismic patterns, where the main characteristics of each unit are presented with their respective instantaneous amplitude, instantaneous phase, sweetness, and semblance attributes.

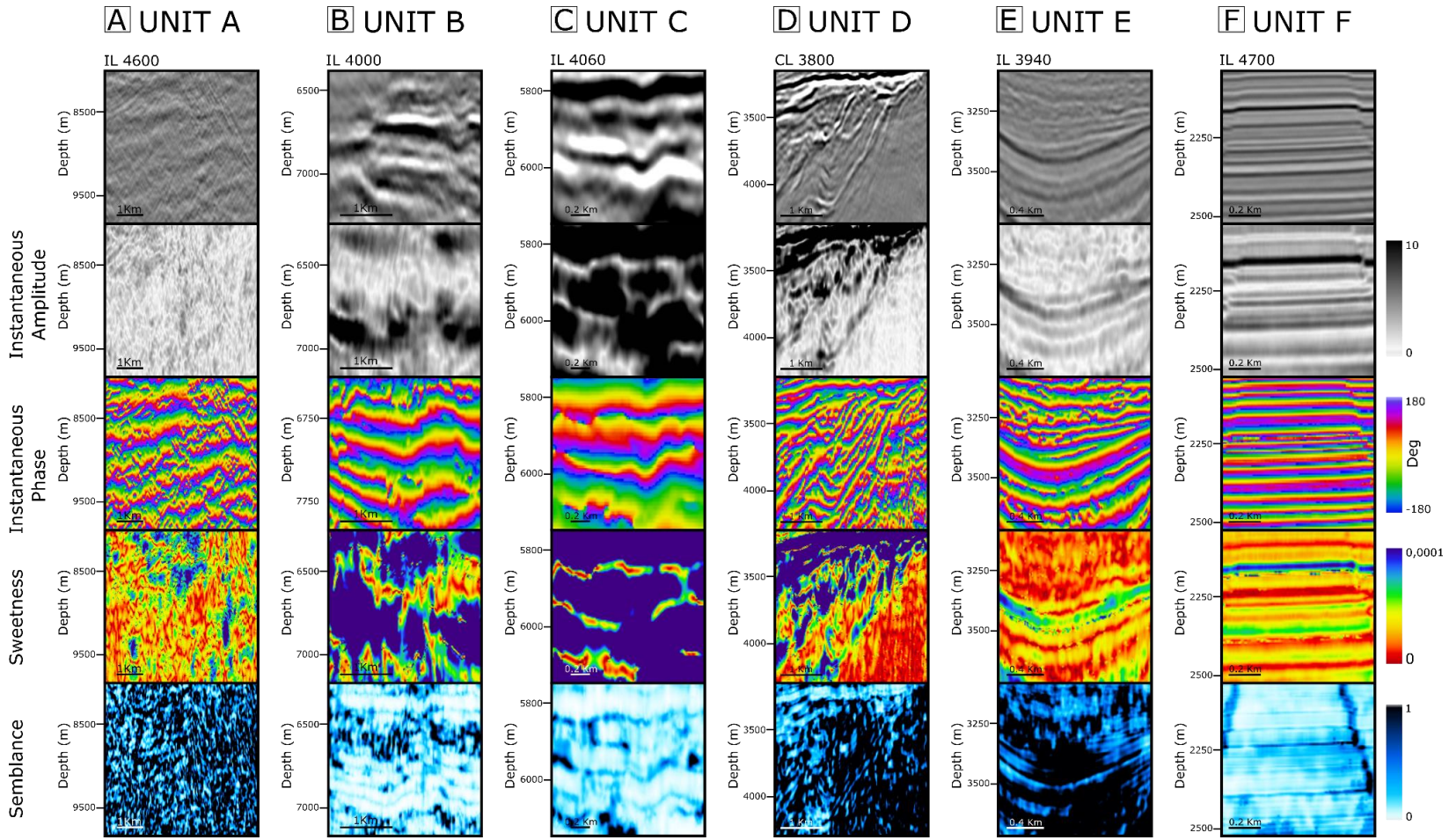

Figure 6 - Summary of the described seismic patterns, showing instantaneous amplitude, instantaneous phase, sweetness, and semblance attributes for units A to F.

5.2.4.2 Analysis of the Identified Structures

The studied area can be divided into two structural domains, deep and shallow ones, separated (Fig. 7 and 8, respectively). Both domains consist of normal faults separated by horizon 3, in which the deep structures display NE-SW azimuth (roughly parallel to the Brazilian coastline) and dip between 50° to 80°, and the shallow structures have E-W to NW-SE azimuth and dip between 30° and 60°.

The deep structures consist of five main normal faults with curved surfaces, which occur below 5,000 m depth. In the 3D model, they are discriminated by different colors: green, pink, red, dark blue, and yellow (Fig. 7). Two main faults are N-S trending (green and pink ones) dipping about 50° to 60° to W and occurs in the central portion of the Búzios Field. In the NE region of the study area, the pink fault is deflected towards NE-SW, and its dip angle decrease. The red fault trends to the NE-SW direction and dips 60° to 80° to NW. The fault represented in dark blue also trends to NE-SW but it dips about 70° to SE. The yellow fault is trending approximately W-E and dips 60 to 65° to the north. All of these faults cross units A and B, and only the yellow one crosses units A, B, and C, reaching the base of Unit D. The set of these structures forms grabens, half-grabens, and horsts. When half-graben geometries occur, the blocks are slightly tilted to NE.

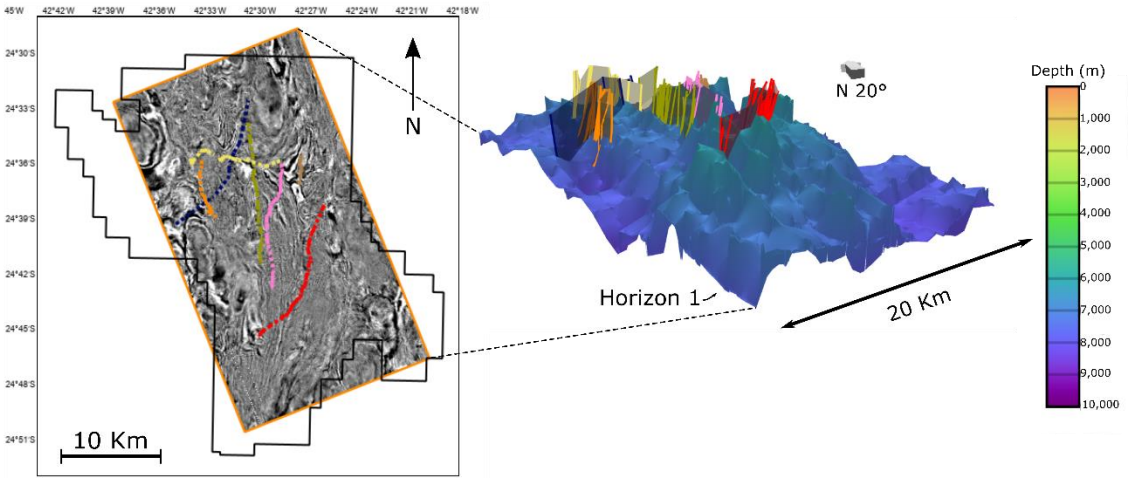

Figure 7 - Set of deep structures. The map on the left represents a depth slice of 6680 m within the study area (orange polygon). On the right, the 3-D visualization of the deep mapped faults and horizon 1.

The group formed by the shallow structures consists of nine major normal faults which occur above 5,000 m depth. The major faults are also discriminated by colors according to Figure 8. The fault colored in pink dips 40°-55°S and has a curved surface, its direction is approximately E-W with a deflection towards NW, where occurs a thick dome from Unit D. The group formed by the parallel normal faults marked in purple, light blue, and light green

has the same E-W deflected to NW trend, but the opposite dip direction (40°-55°N), which may represent a conjugate pair with the pink fault. Other conjugate pairs occur towards S-SE, coinciding with the unit D highs. In the central portion, the conjugate pair formed by the yellow and dark red faults also contours the Unit D domes and has the same E-W deflection around the dome. The dark red fault dips 30° to 50° to the north and exhibits the largest vertical slip up to 600 m (Fig. 9) and outlines the horizon 5 geometry, consequently conditioning Unit E and the lower portion of Unit F thickness. Figure 8 shows this great displacement and the tilting of blocks of units E and F to S-SE. The yellow fault, conjugated to the dark red fault, dips 30° to 45°S. Towards the SE region, a set formed by the parallel dark green and orange faults exhibits a W-E trend and dips about 45° to 60° to the north. At last, the brown fault located at the southern portion of the study area has the same direction and dip as the dark green and orange ones, but a more constrained lateral expression. Additionally, transtractive features (e.g. negative flower structures) were observed at the top of the Unit D highs. In general, semblance is the seismic attribute that better highlights these faults by black lines which mark high dissimilarity.

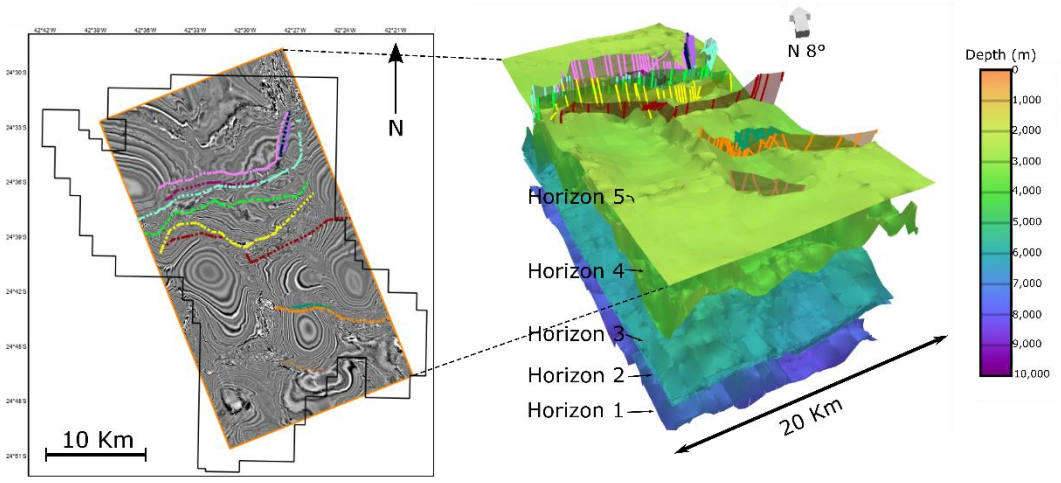

Figure 8 - Set of shallow structures. The map on the left represents a depth slice of 2800 m within the study area (orange polygon). On the right, a 3-D visualization of the shallow structures crossing horizon 5.

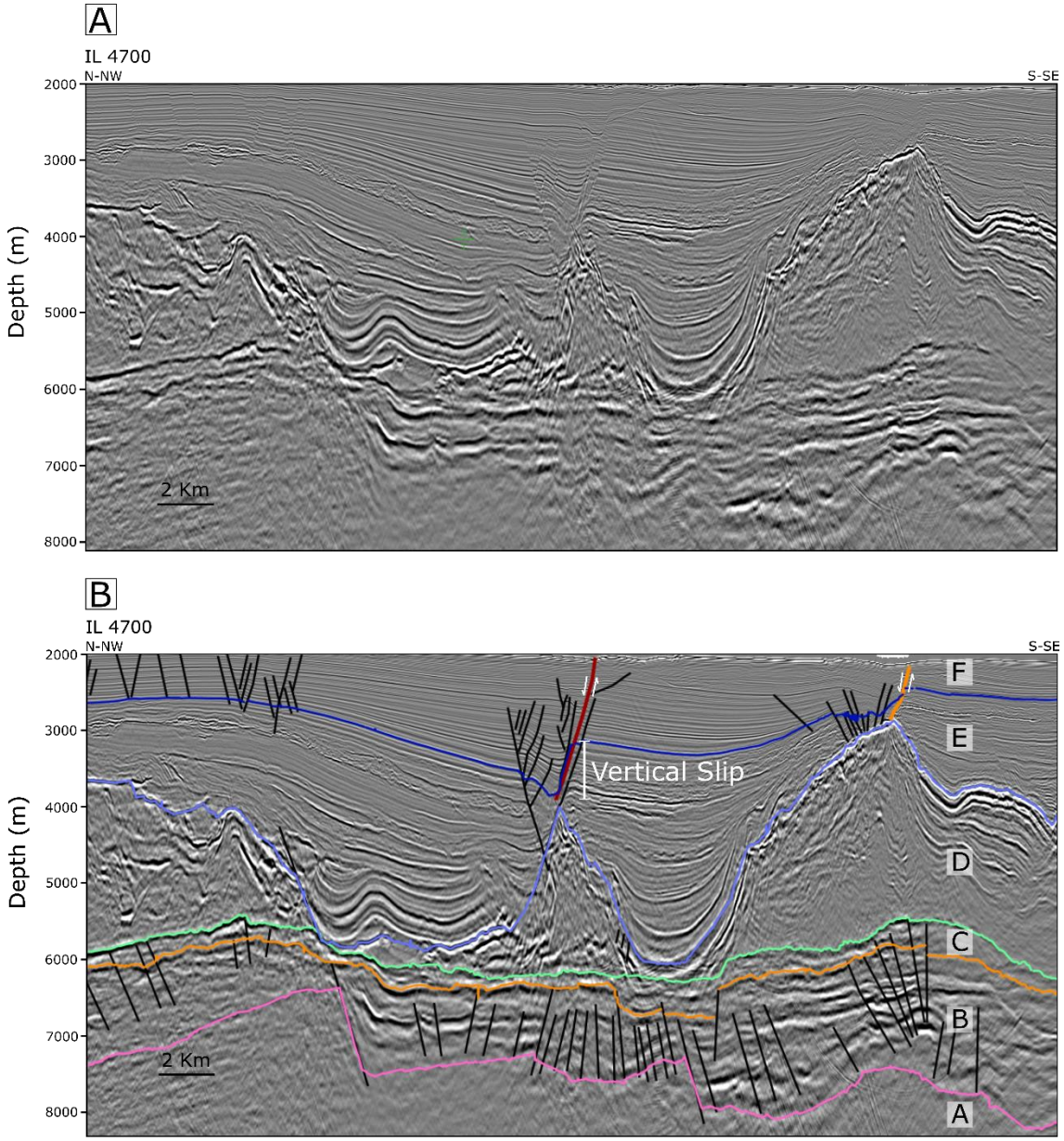

Figure 9 - Region with the largest vertical slip observed. A) Non-interpreted, and B) interpreted seismic section. The white arrows indicate the sense of relative displacement. Letters A, B, C, D, E, and F refer to units A, B, C, D, E, and F, respectively.

Under the surface of erosion observed in Unit F, it is possible to observe other associated structures, such as drag folds that form a synclinal right under the fault plane (pink fault, Fig. 10). The synclinal configures a normal drag in the hanging wall of the normal fault. A detachment surface (green line in Fig. 10) a lot less inclined than the associated fault is formed right below the drag fold.

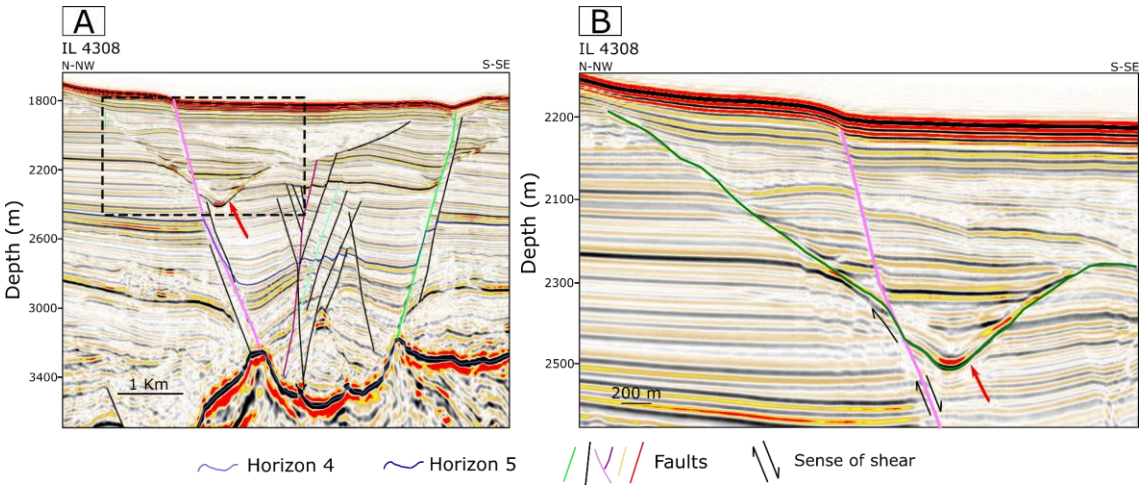

Figure 10 - A) Drag fold formed under the pink fault plane pointed by a red arrow. B) Detailed view of the detachment surface (dark green line in the right figure) formed below the drag fold.

5.2.4.3 Threedimensional Geological Model

After describing these six seismofacies with two-dimensional sections, it is essential to analyze their three-dimensional arrangement to understand and reconstruct the tectonostratigraphic evolution of the Búzios Field and contribute to the understanding of the evolution of the Santos Basin. Starting from Unit A, it is common to observe half-grabens, grabens, and horsts delimited by normal faults. Towards N-NW, this unit is deeper due to the presence of half-grabens constrained by faults dipping to N-NW. The opposite behavior is observed towards S-SE, in which Unit A forms structural highs, shaping the adjacent unit (Fig. 11).

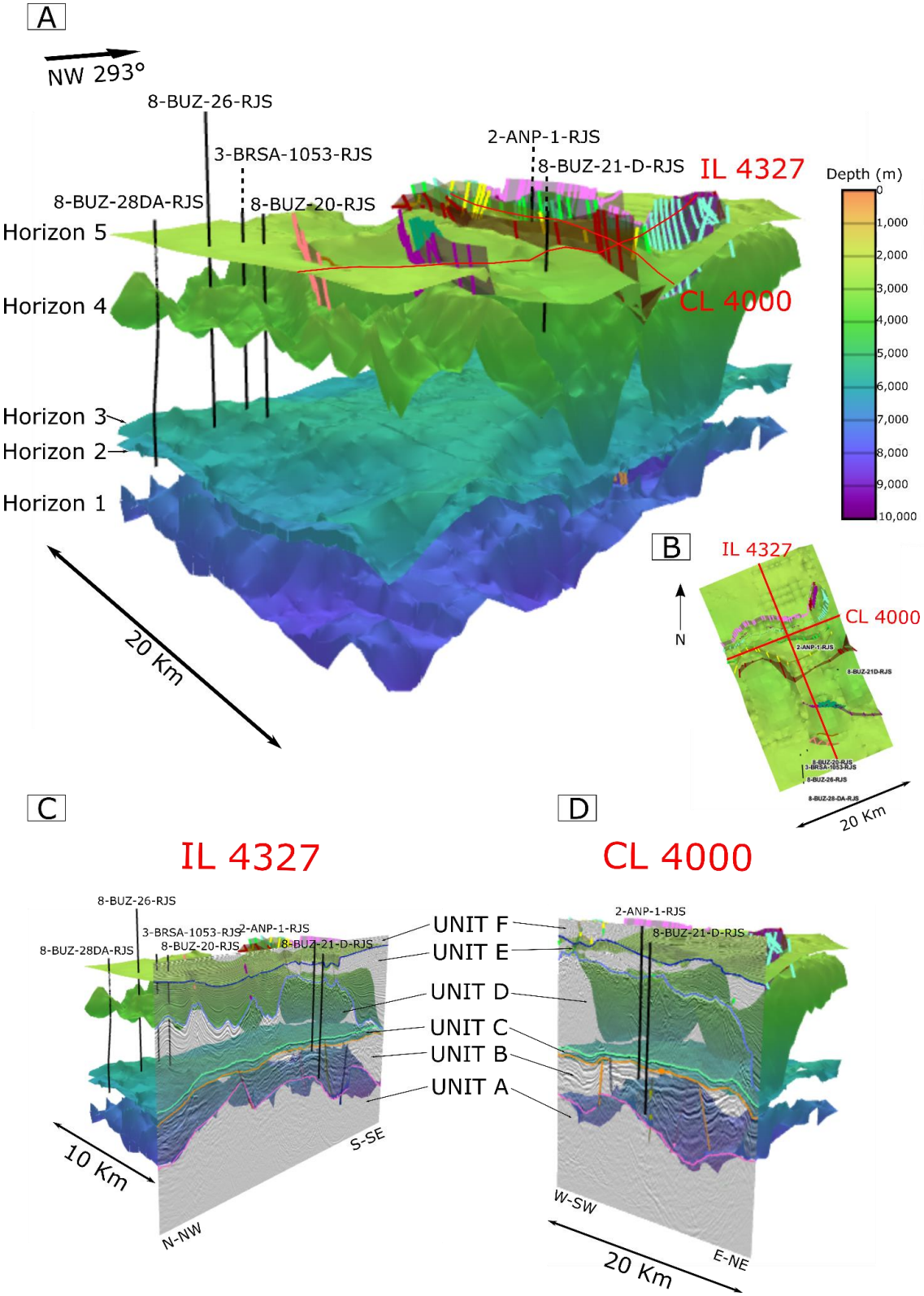

Figure 11 - A) 3D model of the interpreted horizons 1, 2, 3, 4, and 5 in the depth domain. B) Map view with the location of the analyzed wells and the seismic lines IL 4327 and Cl 4000. C) Inline (IL4327) and D) crossline (CL4000) views.

Unit B has a relatively heterogeneous geometry with variable thickness, conditioned by the grabens and horsts formed by Unit A. The isopach map (Fig. 12-A) shows thickness varying from approximately 300 to 2,900 m. The lowest thickness (50 m) is observed in the south portion of the study area, where Unit A forms an expressive horst. There is an expressive thickening towards N-NW, following the topography created by the normal faults that cross units A, B, and the base of Unit T.

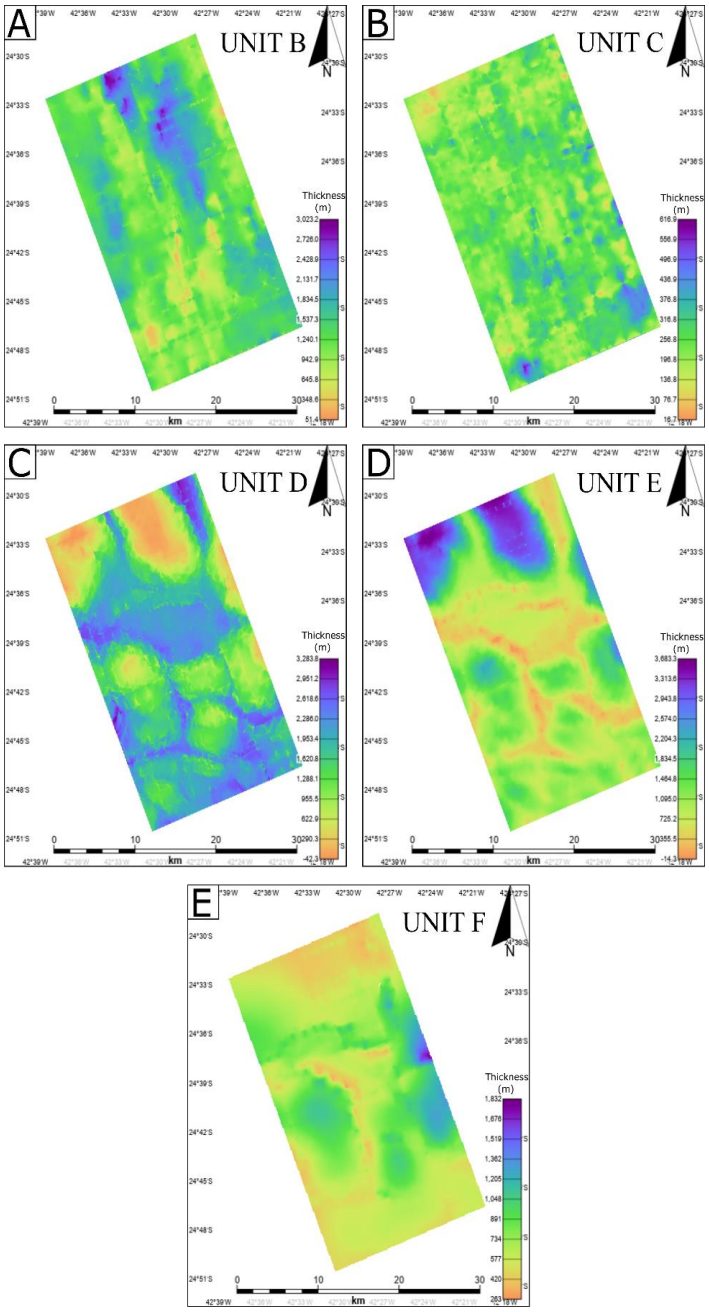

Figure 12 - Isopach maps from A) Unit B, B) Unit C, D) Unit E, D) Unit E, and E) Unit F showing the lateral variation of thickness.

Unit C has a relatively constant thickness, ranging from approximately 50 to 600 m, with an average mean thickness of around 300 m. From the isopach map (Fig. 12-B), it is evident that there is a slight variation in thickness across the study area, with a tendency to thicken towards the S-SE. The top and base surfaces of the unit are mainly regular horizons with a slight downward flexure towards the NE in the southeast part of the Búzios Field. Some of the normal faults described in section 4.2 (this work) cause uplifts of the underlying units A and B, forming structural highs next to the base of the unit.

Unit D exhibits significant variation in thickness and morphologies (Fig. 11 and 12-C). Its thickness ranges from 0 to approximately 3,300 m. In the northern part of the study area, the unit is thin (0 to 300 m) and lies between steep and thick domes and diapirs (with thicknesses of approximately 2,900 m) that form complex ellipsoidal-like morphologies (see Fig. 11 and 12-C). In the north region, it is observed steep relief domes and walls with relatively flat tops with about 12 km of extension, and associated small shallow depressions (Feature 1 in Fig. 13-B). In NW of the Búzios Field, windows (or scars) occur in association with an expressive thinning of Unit D (Feature 2 in Fig. 13-B). Pillows are also observed in the vicinity of these scars (Feature 3 in Fig. 13-B). Towards SE, the unit's topography gets more irregular, with the alternation of thick anticlinals and synclinals features (Feature 4 in Fig. 13-B). In the southeast, gravitational collapse features are observed. Shallow faults described in item 4.2 follow these thin and round-shaped portions. This behavior is consistent across the unit's extensions, although the thickness is less variable towards the S-SE, where domes are less steep and thickness ranges from approximately 800 to 2,700 m. Unit D is considerably thicker in this area, and the topography is slightly less irregular.

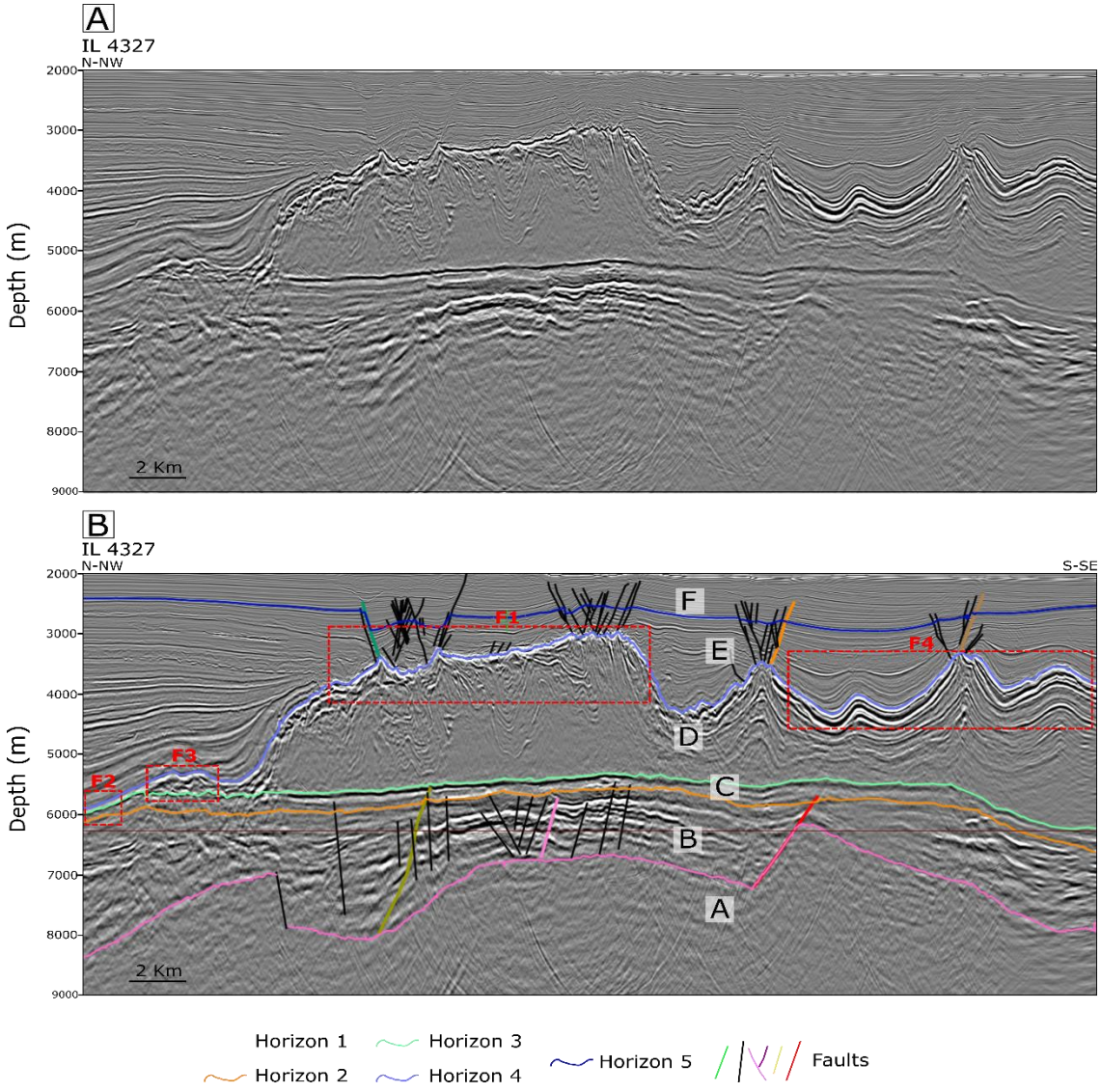

Figure 13 - A) Non-interpreted, and B) interpreted seismic line (IL 4327) showing the main structures observed along Unit D. The red dotted boxes highlight important features (F1 to F4) described in the text. Letters A, B, C, D, E, and F refer to the interpreted units.

Unit F is characterized by a relatively constant thickness of approximately 500 m (Fig. 12-E) with minor variations in proximity to fault zones. On the other hand, notable differences in thickness are observed along the Unit D lows, which host mini-basins of Unit E. When the Unit D lows overlap with fault zones, the thickness of this package usually increases significantly, reaching up to 1,800 m.

5.2.4.4 Well-log Analysis and Statistics

The analyzed log intervals of units B, C, D, E, and F are separated by the horizons 2, 3, 4, and 5, respectively. Figure 14 presents the location of 2-ANP-1-RJS, 3-BRSA-1053-RJS, 8-BUZ-20-RJS, 8-BUZ-26-RJS, and 8-BUZ-28DA-RJS wells in the seismic sections. The

gamma-rays (GAPI), density (g/cm^3), P-sonic (μs/ft), and resistivity (ohm.m) curves general behavior is described in the following paragraphs (Fig. 15).

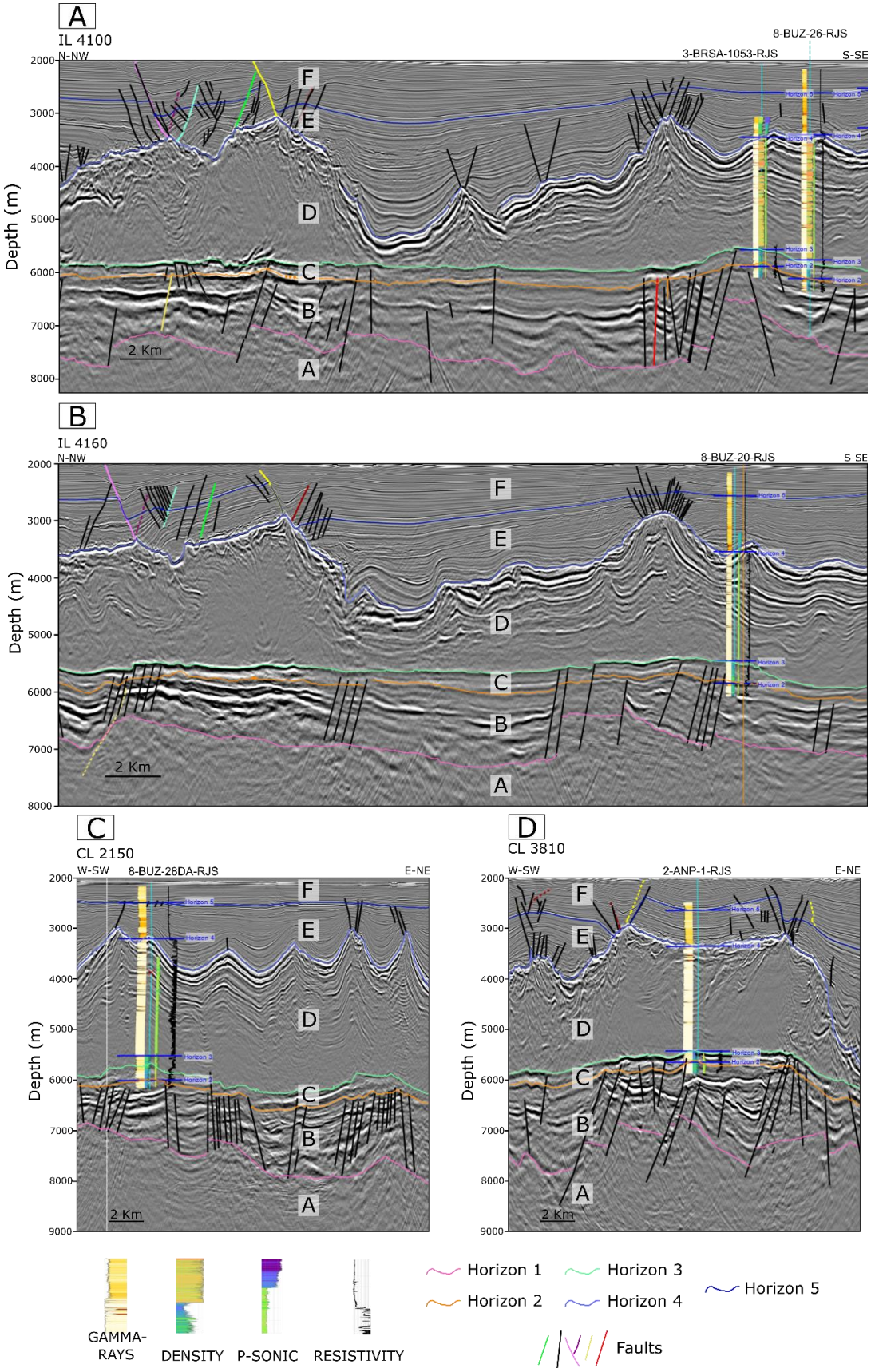

Figure 14 - Location of wells 2-ANP-1-RJS, 3-BRSA-1053-RJS, 8-BUZ-20-RJS, 8-BUZ-26-RJS, and 8-BUZ-28DA-RJS in the seismic sections: A) IL4100, B) IL4160, C) CL2150, and D) CL3810.

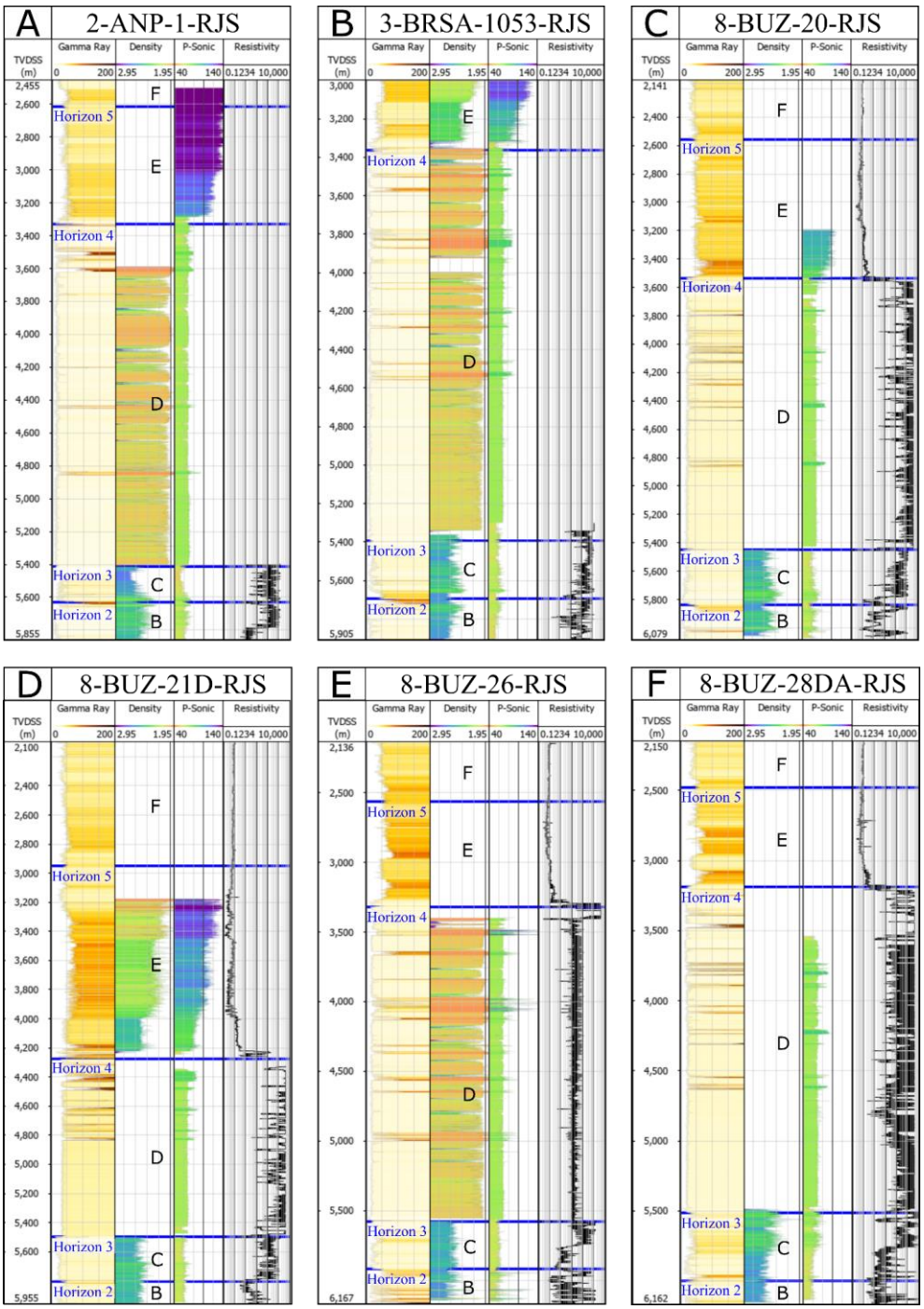

Figure 15 - Gamma-ray, density, P-Sonic, and Resistivity logs in A) 2-ANP-1-RJS, B) 3-BRSA-1053-RJS, C) 8-BUZ-20-RJS, D) 8-BUZ-21D-RJS, E) 8-BUZ-26-RJS, and F) 8-BUZ-28DA-RJS wells. Letters from B, C, D, E, and F refer to units B, C, D, E, and F, respectively.

Analyzing the behavior of the gamma-ray logs, units E and F exhibit the highest values, varying from 10 to 211 GAPI. Unit D shows the lowest values of GR, with expressive intercalations of peaks of high signal (up to 200 GAPI). Units B and C present low to intermediate values of gamma-ray, which range from 0 to 61 GAPI. Unit D has the lowest average density, varying from 2.06 to 2.17 g/cm^3, while units B and C exhibit the highest average mean (from 2.46 to 2.59 g/cm^3). The behavior of P-wave slowness curves discriminates

three major patterns from top to bottom units: high, intermediate, and low slowness. Unit E has the highest average slowness, ranging from 99 to 125 us/ft. Unit D presents the intermediate slowness pattern, with the average mean between 68 and 70 us/ft. Units B and C exhibit the lowest average P-Sonic values, varying from 57 to 64 us/ft. At last, resistivity curves provided abrupt changes between units D and E, and units C and D. The highest average mean is observed in Unit D (up to 2,590 ohm.m), while the lowest is presented by units E and F (from 1 to 42 ohm.m). At wells 8-BUZ-21D-RJS (Fig. 15-D) and 8-BUZ-26-RJS (Fig. 15-E), there is an important decrease in resistivity at approximately 5,800 m. All the results for minimum, maximum, average mean, and standard deviation are presented in Table 1.

Table 1 - Results for minimum, maximum, average mean, and standard deviation obtained for gamma-ray, density, P-sonic, and resistivity curves per unit.

UNIT		Gamma-Ray (GAPI)	Density (g/cm^3)	P-Sonic (us/ft)	Resistivity (Ohm.m)
	Filter	Trimmed mean 25%			
B (Syn-Rift II)	Min	6.9 - 15.1	2.06 - 2.44	49.2 - 57.3	0.7- 7.1
	Max	61.3 - 139.2	2.59- 2.71	65.7 - 120.4	128.0 - 1950.0
	Mean	20.1 - 40.5	2.47 - 2.57	57.8 - 63.4	19.6 - 435.2
	Std dev	9.6- 27.5	0.03 - 0.11	2.0 - 13.5	20.0 - 491.5
C (Post-Rift I)	Min	0 - 14.3	2.10 - 2.45	48.7 - 54.1	0.9 - 64.1
	Max	41.2 - 61.3	2.64 - 2.87	64.1 - 80.8	1331.7 - 10530.3
	Mean	17.8 - 30.9	2.46 - 2.59	57.1 - 64.2	246.5 - 1427.0
	Std dev	5.4 - 11.7	0.04 - 0.12	2.5 - 6.7	246.0 - 2225.8
D (Post-Rift II)	Min	0 - 13.7	1.52 - 1.62	51.2 - 55.4	0.9 - 24.3
	Max	108.4 - 208.4	2.90 - 4.63	86.4 - 154.2	5000.0 - 5012.4
	Mean	14.6 - 44.0	2.06 - 2.17	67.7 - 69.9	1.8 - 2590.0
	Std dev	10.7 - 25.3	0.20 - 0.50	3.4 - 7.2	899.6- 1979.4
E (Drift I)	Min	10.0 - 24.0	1.20 - 1.88	52.6 - 57.2	0.2 - 0.3
	Max	64.0 - 211.3	2.93- 2.96	107.8- 160.0	15.1 - 4995.3
	Mean	43.4 - 58.7	2.27 - 2.37	99.3 - 125.1	0.88 - 41.8
	Std dev	9.0 - 16.6	0.18 - 0.19	8.0 - 20.1	1.1 - 369.1
F (Drift II)	Min	11.7 - 31.9	–	–	0.5 - 0.7
	Max	57.9 - 77.9			0.8 - 0.9
	Mean	38.6 - 50.5			0.7 - 0.8
	Std dev	7.7 - 12.3			0 - 0.1

5.2.5 Discussions

5.2.5.1 Interpreted Units in the Context of a Marine Rift Basin and its Tectonic Components

To incorporate the interpreted seismic units into the geological history of the Santos Basin, it is necessary to correlate these units to the tectonic compartments of a marine rift basin. Firstly, it is necessary to comprehend some tectonic-stratigraphic models, particularly the ones presented in Bosence (1998). This model describes the term syn-rift as a period of basin evolution characterized by mechanical extension. It is also reflected in stratigraphic features that indicate syn-depositional fault movement. The post-rift term denotes any strata that form after the active extensional tectonics.

Based on the evidence of the initial stages of the rifting process, such as grabens and half-grabens, Unit A was classified as Syn-Rift I phase. It is important to note that volcanic rocks can also form part of a pre-rift stage, such as in the Southern Red Sea, Yemen, where an asthenospheric plume occurs (cf. Mitchell et al. 1992).

Unit B also displays seismic patterns consistent with syn-rift tectonics, as demonstrated by Prosser (1993, Fig. 16), and I interpreted it as a Syn-Rift II stage. In the study area, these features take the form of wedge-shaped geometry created by divergent reflectors with an oblique parallel configuration (Fig. 17). The combination of these characteristics indicates a progradational regime. Additionally, the portions of Unit B that exhibit the divergent and oblique parallel pattern with the classic wedge-shaped configuration may represent the initiation of the rift. The divergence of reflectors may be a consequence of syn-tectonic deposition (Kuchle, 2010). The chaotic pattern observed near the base of the footwall slope can be associated with the climax stage and suggests aggradation.

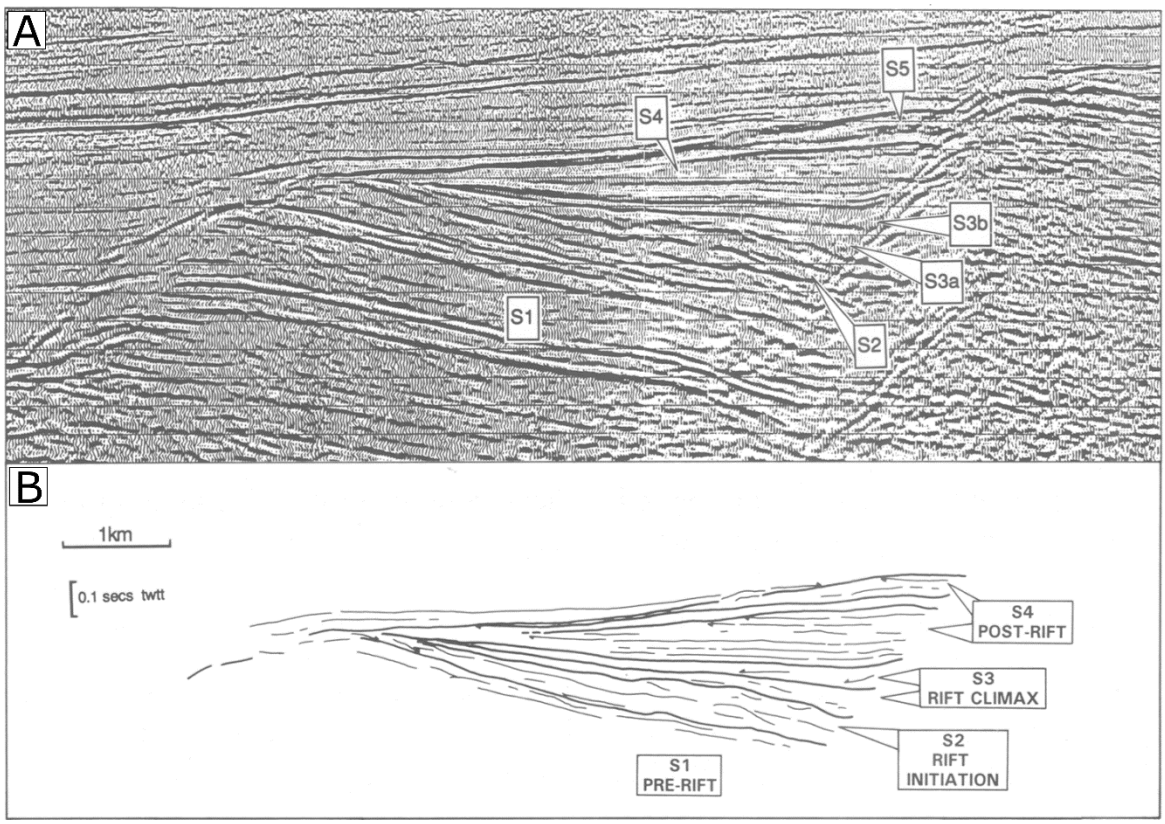

Figure 16 - A) Seismic section of a Barents Sea half-graben. B) Interpreted seismic section showing the stages of rift evolution on a half-graben. S1 is the pre-rift stage, S2 is the rift initiation stage, S3 is the rift climax, and S4 corresponds to the post-rift stage. S2 is characterized by wedge-shaped geometry created by divergent reflectors. S3 consists of the development of divergent forms related to continued tilting of the hangingwall during deposition. S4 is marked by a reflector package with a simple parallel infill (Prosser, 1993).

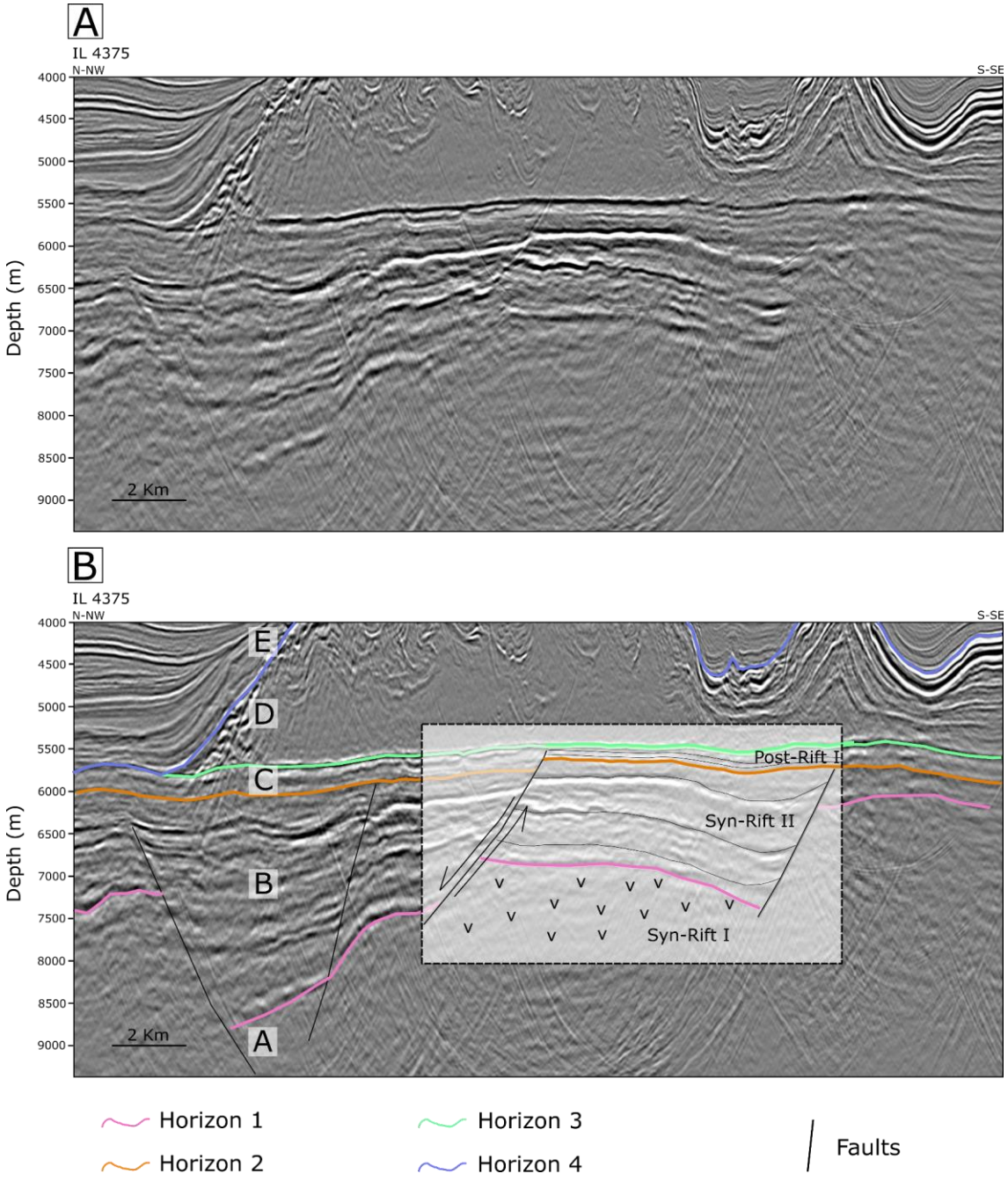

Figure 17 - Detailed view of inline 4375. A) Non-interpreted, and B) interpreted seismic profile. The dotted polygon highlights a half-graben exhibiting a wedge-shaped geometry, with oblique-parallel internal reflectors in Syn-Rift I unit and sub-parallel to plane-parallel reflectors in the Post-Rift I unit. Letters A, B, C, D, E, and F refer to units A, B, C, D, E, and F, respectively.

I interpreted Unit C as a Post-Rift I stage due to the change from the divergent to a plane-parallel pattern, indicating the transition from syn-rift to post-rift phase, according to Bosence (1998). In the post-rift phase, the filling of the basin is characterized by aggradational and progradational geometries, whose surfaces dip in the direction of the increase of the accommodation space in the center of the basin. The horizontal and plane parallel configuration of Unit C reflectors could represent a reflex of its deposition after intense tectonic activity

(Kuchle, 2010). Although the base of Unit C is affected by some of the normal faults, it was not interpreted as a part of the syn-rift section. This feature was considered a posterior reactivation of the syn-rift faulting. Macedo et al. (2021) argue the faults which affect the top of the post-rift (or sag) section indicates the tectonic activity is, at least locally, controlling the post-rift sedimentation in the Búzios Field area.

Unit D was interpreted as the saline section of the Santos Basin, representing a Post-Rift II stage. This unit was interpreted as post-rift once it was not affected by the normal faults associated with the rift phase. Mitchell et al. (1992) describe syn-rift evaporites Red Sea (Yemen), where the salt section is intensely controlled by the rift faults, contrary to what we observed in the study area. The domain without stratification of Unit D was interpreted as a halite-rich portion, with predominant massive composition, without pervasive structures such as bedding or foliation.

Unit E and F represents the establishment of the passive margin of the Santos Basin. Unit E is interpreted as synchronous with the beginning of continental drift, representing a Drift I phase, while Unit F is conceived as a posterior stage (Drift II). The major criterion for discriminating between units E and F is the amount of deformation since Unit E is intensely deformed by the upwards movement of the underlying package. Consequently, Unit E is understood as syn-halokinesis, while the F unit is interpreted as posterior, mainly affected by predominantly extensional tensions in the continental drift process. The instantaneous amplitude attribute reveals the existence of some expressive surfaces marked by the black color parallel to the unit stratification, which probably marks smaller cycles of stratification in the context of the basin opening.

5.2.5.2 Interpreted Units in the Stratigraphical Context of the Santos Basin

In the attempt to understand how the seismic expression of the interpreted unit is linked to the geological framework of the Santos Basin, the analysis of the selected well logs is the main tool to correlate the units with the regional and local stratigraphy. Here we present a description of the well registers from the lower (Unit B) to the upper unit (Unit F). As aforementioned, the rifting opening begins with the deposition of the basaltic economic basement of the Syn-Rift I stage, related to the Camboriú Formation between the end of Valanginian and Barremian (Moreira et al. 2007). Although this unit is not identified by any of the wells, this correlation was made exclusively by the seismic expression of the unit (chaotic

to absent reflections) and what is regionally known as the economic basement of the Santos Basin.

The Syn-Rift II unit was deposited as the extensional stresses continued to act on the basin. In this context, the basin infill consists of alluvial fan sediments in the proximal portions and lacustrine lithologies in the distal portion, deposited from the Barremian to the Eo-Aptian. Analyzing the behavior of the logs in the interval of Syn-Rift II unit (Unit B), the major difference consists of the gamma-ray and resistivity curves. The abrupt change in the pattern of these curves in the transition from the overlying Unit C and Unit B, especially in 8-BUZ-21D-RJS and 8-BUZ-26-RJS wells. Horizon 2 is marked by a peak in GR values (from 50 to 88 GAPI). The peaks with higher values of gamma-ray can be associated with the presence of shales with Mg-clays described in the Itapema Formation (Moreira et al. 2007). In some wells, significant increases in the GR values were identified during the transition from the Itapema Formation to the Barra Velha Formation. Castro (2019) also associates these peaks with shales of the Itapema Formation in some wells, while in others, they are associated with organic-rich mudstones or carbonates of the Barra Velha Formation. In this work, the entire Syn-Rift II unit is correlated to the Itapema/Piçarras interval (Moreira et al. 2007).

Assuming the Syn-Rift II unit represents Piçarras and Itapema formations, the overlying package (Post-Rift I unit) corresponds to the Barra Velha Formation (Moreira et al. 2007). This moment represents the beginning of the transition from a continental to a shallow marine environment. The Barra Velha carbonates are assumed to have been deposited in a shallow alkaline lake, from the hyperextension of the lithosphere and increased geothermal gradients to levels favorable for the generation of alkali-rich brines (Farias et al. 2019). In the transition between the Post-Rift I unit (Unit C) and the under and overlying units (Syn-Rift II and Post-Rift II, respectively), all the analyzed curves exhibit an abrupt change in the pattern. The major difference between Post-Rift I and the overlying Post-Rift II unit is the great increase in density and decrease of slowness in the former. The average mean of P-sonic calculated from the six selected wells yielded values from 57 to 64 us/ft (Vp = 4,750 m/s to 5,335 m/s). The controls on sonic velocity in carbonates presented in Anselmetti & Eberli (1993) depend on a series of parameters such as effective pressure, depositional environment, diagenetic alterations, and age of the sediment. According to Anselmetti & Eberli (1993), the carbonate rocks show a broad interval of P-velocities (from 2,000 m/s up to 6,000 m/s). Velocities of carbonates that were deposited on the shallower water platform have higher velocities than velocities from deeper water samples. Consequently, the velocities of this section in the study area (from 4,750 m/s to

5,335 m/s) corroborate the hypothesis of a shallow alkaline lacustrine origin. Moreover, 8-BUZ-26-RJS and 8-BUZ-28DA-RJS wells show an important decrease in resistivity at approximately 5,800 m. This behavior can be associated with the presence of a high-resistivity material in the upper portion of Unit C. Once the upper portion is covered by the base of the salt layer (horizon 3), it is reasonable to suggest the presence of oil at the top of the Barra Velha Formation at the locations of 8-BUZ-26-RJS and 8-BUZ-28DA-RJS wells.

According to Tavares da Silva & Gordon (2021), these carbonates display variable amplitude, and small-scale progradation, are rarely affected by faults, and exhibit common features such as carbonate ramps and mounds deposited preferentially onto preexisting basement highs. These features are consistent with the ones observed in the study area, such as sub-parallel to parallel reflectors with mound geometries at the top of Unit C. The sub-parallel to the parallel pattern can be associated with the aggradational flat-topped carbonate platform described in Buckley et al. (2015), while the mounds are associated with carbonate build-up facies (see Ferreira et al. 2021).

Note that all the analyzed curves exhibit an abrupt change in the pattern when passing from Post-Rift I to Post-Rift II units. Probably, this is a consequence of an abrupt change in the lithology. This is related to an unconformity that separates the carbonate sequence from the evaporitic one (Buckley et al. 2015). Therefore, the Post-Rift II unit represents the transition between the sag and marine environment, deposited within a high evaporation rate lake associated with periodic marine transgressions in the Neo-Aptian (Gamboa et al. 2008). The argument of a transition from carbonatic to evaporitic composition is consistent once there is a considerable decrease in density and a slight increase of the P-sonic values. This is an expected behavior since the mean P-wave velocity of halite, the major component of the saline section in the Búzios Field, is 4,549 m/s and its density is 2.03 g/cm^3 (Mohriak et al. 2008 apud Justen et al. 2013). Well-logs from the Post-Rift II unit provided values of density average mean from 2.06 to 2.17 g/cm^3 and the average mean of P-sonic next to 68 us/ft (Vp= 4,504 m/s). Regarding the gamma-ray logs, The Post-Rift II unit has the lowest values, however, it also exhibits some intercalated peaks of high signal. The intercalation of high-value peaks in the upper part of the Post-Rift II unit is ascribed to the stratification of different types of salt, similar to the Evident Stratification Domain (ESD) proposed by Maul et al. (2018a). The extremely high GR values (200 GAPI) are assigned to the presence of sylvite (due to the potassium concentration). Therefore, Unit D is equivalent to the Ariri Formation described in Moreira et al. (2007).

At the base of the Drift I unit (horizon 4), density is the highest and tends to decrease upwards, at the same time P-slowness increases. This abrupt change marks the implantation of a marine environment in the Santos Basin, with the deposition of the postbreakup sediment packages from the Late Cretaceous to the Neogene. Roughly, the lower portion of the Drift I unit can be associated with the limestones from the Guarujá Formation (Moreira et al. 2007). This portion represents the installation of a carbonate platform during the Albian. The overlying package with lower density and higher slowness is assigned to a coarsening-up sequence, once the coarser lithology tends to be more porous, which explains the decrease in density and increase of slowness (VP fluids < VP rock). Therefore, the aforementioned upper portion of the Drift I unit is associated with the intercalation of diamictites from the Itajaí-Açu Formation, deposited in the distal platform, slope, and basin environments. This interval represents a regression phase where the limit of the platform advanced up to 200 km offshore. (Moreira et al. 2007).

The interweaved mound-shaped feature observed at the top of the Drift I unit (Fig. 5) was also interpreted as gravitational flow deposits. At this depth (~3200 m), Moreira et al. (2007) describe the presence of strongly channelized sandstones resulting from dense turbidity currents (Ilhabela Member) related to significant excavations on the slope and platform.

Drift I and II units have the highest average mean of gamma-ray and the lowest resistivity, with the GR values being even higher for the Drift II unit. The gamma-ray log highlights the intercalation of portions with high and medium GR values. The high gamma-ray and low resistivity can be associated with the presence of the Marambaia Formation shales associated with marls, once the presence of clay, a highly radioactive material, accommodates large amounts of interstitial water (Girão, 2013). This also explains the low resistivity values, once water is a conductive material, having very low resistance to electrical current. Moreira et al. (2007) describe the expressive occurrence of dark and radioactive shales throughout the drift mega-sequence. The portions with medium gamma-ray values can be associated with the sandstone bodies intercalated with shales described by Moreira et al. (2007) in the Marambaia Fm. interval. In the context, of the Santos Basin evolution, the Drift II unit represents the moment when the carbonate platform reaches its greatest development in the Miocene. From the Lower Miocene onwards, lower-order sequences undergo transgressive development that reaches its peak in the Mid-Miocene (Serravallian). This interval marks the highest relative sea-level variation from the Miocene to the present, resulting in the deposition of a substantial volume of sediments (Moreira et al. 2007).

The interweaved mound-shaped feature (Fig. 5) observed at depths of about 2,500 m was associated with gravitational deposits of the Maresias Member (Moreira et al. 2007). The surface of erosion depicted in Figure 10 possibly represents canyons infilled with mudstones or sandstones described to occur at slope portions in the Marambaia Fm. shales and diamictites.

5.2.5.3 The Búzios Field in the Tectonic-Stratigraphic Evolution of the Santos Basin

5.2.5.3.1 Comparison with the Tupi Field

The Tupi Field, located approximately 50 kilometers southwestward of the Búzios Field, is another giant petroleum field of the Santos Basin (Fig. 1). A series of comparisons can be placed between the Tupi and Búzios fields, based on recent works (cf. Adriano et al. 2022). Compared to the Búzios Field, the Tupi Field exhibits an important NE-SW thinning of the Piçarras, Itapema, and Barra Velha formations, constrained by the Camboriú Formation high (the Tupi High) highlighted in Figure 18 (feature 1). Analyzing four seismic sections presented in Adriano et al. (2022), the Barra Velha Formation is thicker than we interpreted in the study area (Fig. 18).

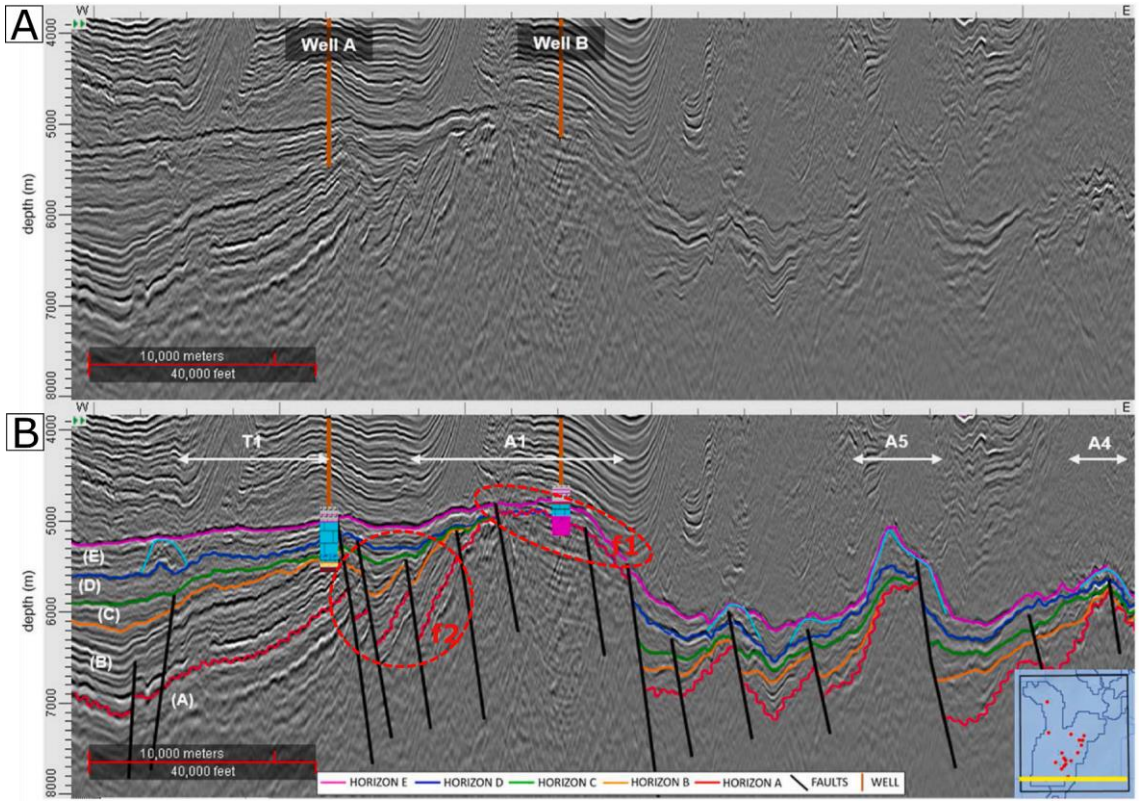

Figure 18 - Tupi Field seismic section presented in Adriano et al. (2021). A) Non-interpreted, and B) interpreted seismic profile. Horizon A (red), Horizon B (orange), Horizon C (green), Horizon D (blue), and Horizon E (pink) represent, respectively, the top of Camboriú, Piçarras, Itapema, Lower Barra Velha, and Upper Barra Velha Formations. Light blue represents mounded features. White double-arrowed lines represent the structural

compartmentalization of the Tupi Field area. Extracted from Adriano et al. (2021). The red dotted circles represent the features f1 and f2 mentioned in the text.

Regarding the structures, a remarkable difference is the rotation of the syn-rift blocks. The blocks of the Tupi Field are tilted at a higher angle, where the internal reflectors are more inclined than in my study area (feature 2 in Fig. 18). According to Adriano et al. (2021), there are three main sets of normal faults conditioning the rift phases. NE-SW and N-S trends faults control the Lower and Upper Rifts (Camboriú, Piçarras, Itapema, and Lower Barra Velha formations), while NW-SE trend conditions the Later Rift (Upper Barra Velha Formation). My work mapped four main trends: N-S direction west-dipping, NE-SW direction northwest-dipping, NE-SW direction southeast-dipping, and W-E trend dipping to north. In this, only the W-E trend (yellow fault) crosses the Barra Velha Formation (Unit C), while all the others are related to units A and B, coherent with the NE-SW and N-S trend faults in Adriano et al. (2021).

5.2.5.3.2 Comparison with the Sapinhoá and Lapa fields

The Sapinhoá and Lapa fields, located ca. 120 kilometers southwestward of the Búzios Field, also have an important role in the pre-salt exploration (Fig. 1). Ribeiro da Silva et al. (2021) present the tectonic-stratigraphic evolution of the Barra Velha Formation in the area of the Sapinhoá and Lapa fields. According to interpreted sections shown in Ribeiro da Silva et al. (2021), there are remarkable differences from what was observed in my study (Fig. 19). The first and most prominent one is the geometry of the evaporitic cover, the Ariri Formation. In the region of the Sapinhoá and Lapa, the salt section is predominantly thick, forming large salt walls (feature 1 in Fig. 19). There is a widespread occurrence of this unit across the mapped area, while in the northwest of the Búzios Fied, the salt section forms windows (or scars) due to the intense thinning or absence of this package. Besides, the salt in the area of Sapinhoá and Lapa fields is more stratified, the stratification is observed in variable depths (not restricted to the top of the unit as in the Búzios Field). In the interpreted NW-SE section from Ribeiro da Silva et al. (2021), tongues of the non-stratified salt are observed interfingered with stratified salt (feature 2 in Fig. 19).

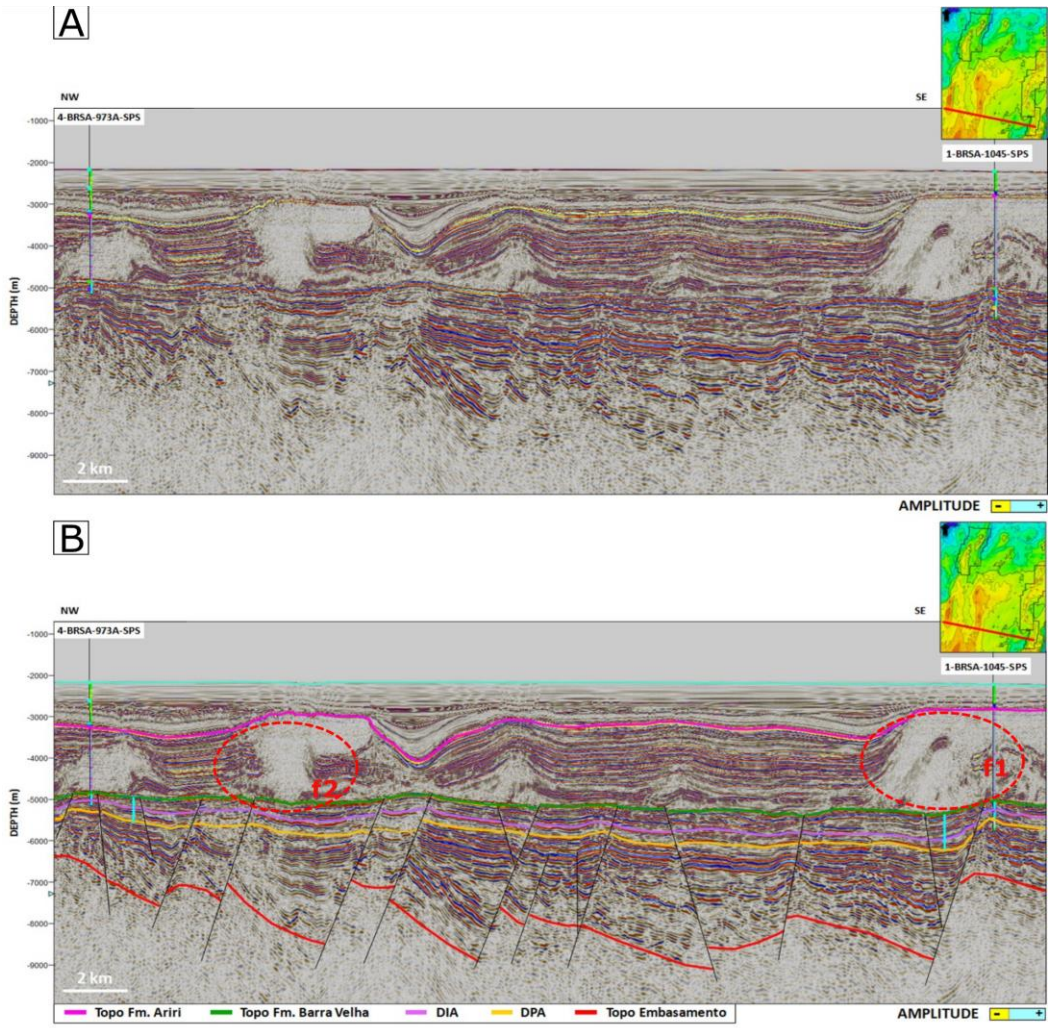

Figure 19 - Sapinhoá and Lapa fields seismic section presented in Ribeiro da Silva et al. (2021). A) Non-interpreted, and B) interpreted (bottom) seismic profile. The acronyms DIA and DPA stand for Intra-Alagoas Discordance and Pre-Alagoas Discordance, respectively. The seismic section location map displays the top map of the Barra Velha Formation. Extracted from Ribeiro da Silva et al. (2021). The red dotted circles represent the features f1 and f2 mentioned in the text.

5.2.5.3.3 Rifting Evolution in the Santos Basin

The next step of my research consists of investigating how the tectonic evolution of the Santos Basin is expressed within the area of the Búzios Field. To do this, it its crucial to understand how the Santos Basin was generated regarding the rifting mechanisms. A brief review of the main types of rifting proposed by Bosence (1998) is presented in Appendix A. Summarily, there are four main types and with especific relationship with the observed stratigraphic patterns at the basin scale. These mechanisms correspond to pure shear, simple shear, heterogeneous stretching, and mantle plume-related. McKenzie (1978) and Wernicke (1985) also discuss models of rifting and the development of rift basins (see Appendix A).

My research did not find sufficient evidence to determine which rifting mechanism was responsible for the opening of the Santos Basin. In the small mapped area, features suggestive of simple or pure shear were observed in the central portion of the basin, such as expressive and laterally continuous syn- and post-rift layers (red boxes in Appendix A. Fig. A1-A and B). However, the simple-shear model is predominantly characterized by differing distal and proximal regions. This argument is consistent with what was observed in the comparison of the Búzios (proximal), and Tupi, Sapinhoá, and Lapa (distal) fields.

In the Búzios Field area, the syn-rift section comprises the siliciclastic and carbonate rocks from Unit B (Piçarras/Itapema formations) and also comprises the basaltic economic basement from Unit A (Camboriú Formation). Since the plume-related model (Fig. A1-D; Bosence, 1998) suggests that the syn-rift section is entirely composed of a volcanic stratigraphy, this model is not preferred here, although the conceptual model for this Early Cretaceous phase admits a small asthenospheric uplift (Heilbron et al. 2000).

An important criterion that would support the distinction between pure and simple shear would be the presence of detachment surfaces associated with listric faults in the syn-rift stage, suggestive of simple shear. Although such structures were not observed, it is not possible to determine their existence or absence. The study scale (up to 9,000 m) and the seismic survey resolution could have masked their detection. Another important factor to consider is that both mechanisms can exist concomitantly and, locally, one or the other may predominate. Therefore, analyzing such a small area within an extensive regional context of the Santos Basin would not be sufficient to determine its opening mechanism, *i.e.,* the Santos Basin has features that suggest both pure and simple-shear mechanisms, with some uplift caused by asthenospheric plumes. However, pure-shear or simple-shear strains likely occur at the same extensional zone. Once the deformation is multiepisodic, each one tends to be heterogeneously distributed rather than coincident. Consequently, the two concepts are not mutually exclusive (Armstrong, 1982).

Although the rifting mechanism is not defined, Rabinowitz & LaBrecque (1979) reconstructed the South Atlantic Ocean opening by a clockwise rotation around a pole in the northeast of Brazil. Figure 20 presents a reconstruction of South Atlantic rifting by the late Aptian (107 M.y.) modified by Rabinowitz & LaBrecque (1979). After this model, Szatmari & Milani (2016) argue the rift was formed as a result of a southward increasing extension in the rear of South America's clockwise rotation over an upper mantle kept anomalously hot before rifting by being continuously covered by western Gondwana's lithosphere for 350-400 Ma and heated by upwelling plumes. The clockwise rotation of South America relative to Africa

opened the wedge-shaped, southward widening, NNE-SSW to N-S-trending South Atlantic rift, while it compressed most of the ENE-WSW to E-W-trending Equatorial margin. The rifting process both widened and deepened the South Atlantic basin towards the south. Rift faulting migrated diachronous toward the future spreading center (in South America from west to east).

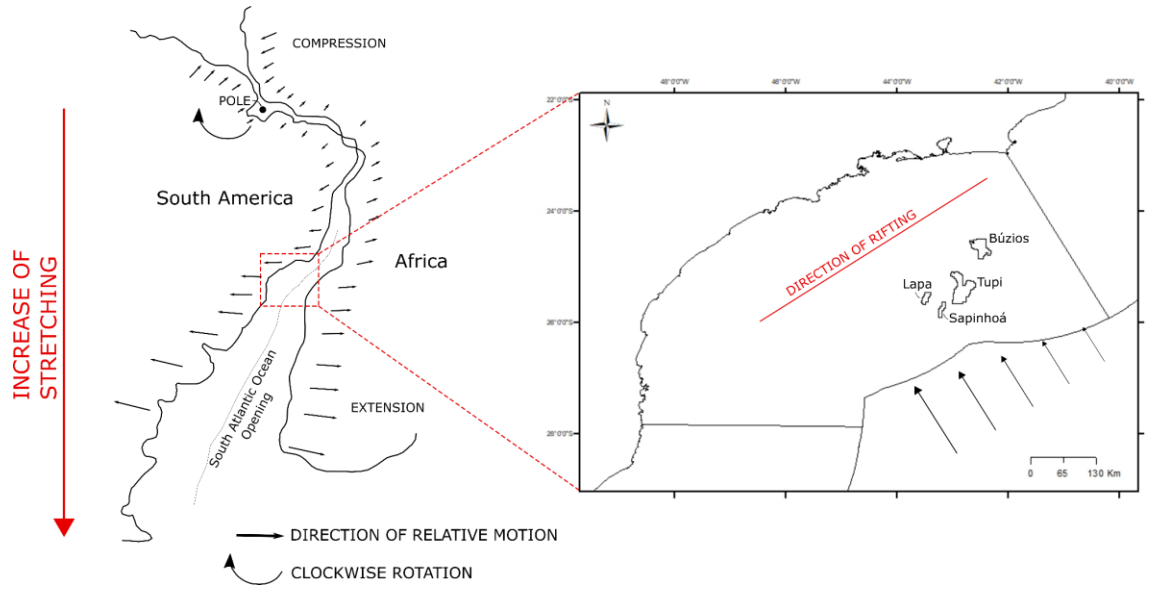

Figure 20 - Schematic figure of the reconstructed South Atlantic Rift by the late Aptian (107 M.y.) modified by Rabinowitz & LaBrecque (1979). On the right, the location of Búzios, Tupi, Sapinhoá, and Lapa fields within the Santos Basin. The relative displacement of Africa and South America is represented by the black arrows.

The most widely accepted model regarding the evolution of the South Atlantic Ocean is summarized and explained by Heilbron et al. (2000) after Cainelli e Mohriak (1998, 1999b). This model is based on the lithospheric stretching model proposed by McKenzie (1978). The first phase is characterized by the beginning of regional lithospheric extension, which eventually led to the separation of the South American and African continents. The next phase is marked by an increase in lithospheric stretching (cf. McKenzie, 1978), coinciding with the development of large faults affecting the continental crust, extrusion of continental flood basalts, and formation of half-grabens. After this early Cretaceous tectonic-magmatic episode, tectonic stresses were directed toward the present-day continental margin. These rifts, which were filled with Neocomian to Barremian volcanic and siliciclastic rocks, evolved into the present-day passive margin sedimentary basins.

Towards the end of the rifting phase, there was a further increase in lithospheric extension marked by large faults that rotated the rift blocks and the sedimentary layers previously deposited. The inception of the oceanic crust probably involved the focus of the lithospheric stretching that was previously distributed in a wider region. This phase is

associated with volcanism, reactivation of large faults, and erosion of rift blocks by a regional unconformity that levels the topography, separating continental from transitional to marine environments of deposition. Above this unconformity and below the evaporite transitional sequence, some sedimentary basins show a substantial thickness of Aptian siliciclastic and carbonate rocks. Following the deposition of salt in the Aptian, sedimentation became predominantly carbonatic. An increase in bathymetry led to the deepening of the environment of deposition by the end of the Albian, with the disappearance of the shallow-water carbonates.

Although Heilbron et al. (2000) do not define the mechanism for the opening of the basins on the Brazilian east margin, it can be concluded that it involves pure shear. This is inferred because it is based on the model of constant and uniform stretching controlled by asthenospheric uplift proposed by McKenzie (1978). Furthermore, the Brazilian passive margin and its African counterpart are portrayed as a large symmetrical basin.

Here, we consider four main postulates of the South Atlantic Ocean opening and related salt tectonics (after Heilbron et al. 2000; Szatmari & Milani, 2016): (1) the clockwise rotation of South America relative to Africa about a pole located offshore NE Brazil; (2) the rifting propagation from south to north; (3) rifting process widened and deepened the South Atlantic basin towards the south and (4) salt mobilization/maturity increases basinward. Once the rifting spreading was N-S, the extension was approximately west to east by the time the continents started to separate (Fig 20). With the clockwise rotation around a pole in NE Brazil, the N-S orientation was also rotated about the nowadays N-S position. In Figure 20, the direction of rifting highlighted in red corresponds to the N-S orientation by the time the rifting was opening.

Based on these premises and the fact that the Búzios Field occupies a position closer to the continental margin than Tupi and Sapinhoá/Lapa, we suggest that the displacement caused by rifting was smaller in the Búzios Field (Fig. 20). Therefore, it is reasonable that the syn-rift blocks are more rotated in the area of the Tupi Field, once it experimented with more displacement than the Búzios area.

Once the displacement increased from west to east and rifting process widened and deepened towards the south, the same argument counts for the intensely mobilized and thicker salt layer in Sapinhoá, Lapa, and Tupi fields area. These areas are located at greater distances from the continental margin than Búzios, thus experimenting with more displacement. A schematic diagram (Fig. 21, modified from Jackson & Talbot, 1991 in Gillhaus & Horvath, 2008) shows the relative positions of the Búzios, Tupi, and Sapinhoá/Lapa fields in the context

of salt maturity. The thick package of the evaporitic layer in Tupi and Sapinhoá/Lapa can be assigned to increased salt mobilization basinward due to the halokinesis.

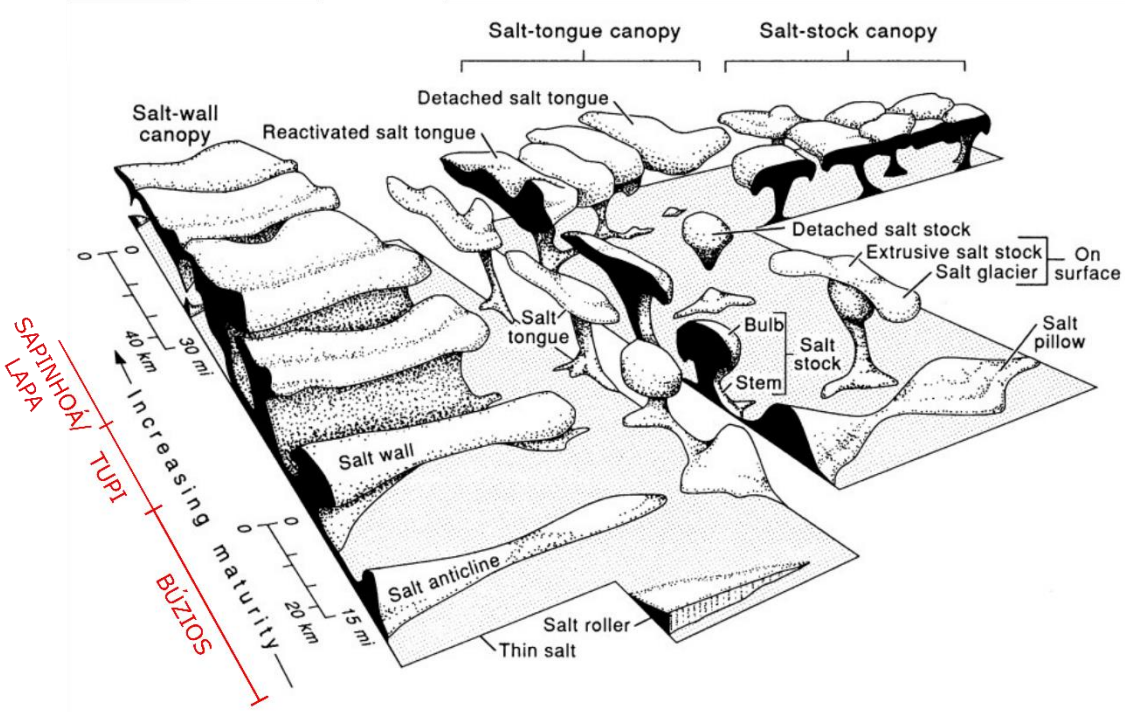

Figure 21 - Block diagram showing the relationship between salt structures and maturity. The relative position of Búzios, Tupi, and Sapinhoá/Lapa fields within the increasing salt maturity is presented in red. Modified from Jackson & Talbot (1991) in Gillhaus & Horvath (2008).

Firstly, it is essential to consider that the driving force for the rise of evaporitic rocks through the non-saline cover rock is gravity combined with density differences between the less dense salt deep underground and its more dense cover rock. The autonomous vertical movement of salt is predicated upon the progressive compaction and cementation of the overlying sand, clay, and carbonate layers in the cover rock as a result of basin subsidence until their density is as high or higher than the density of the salt layers. Local uplift of the salt mainly begins in locations where there are already significant horizontal lithostatic pressure gradients above or within the salt. Regional lithostatic pressure gradients exist in areas such as the transition zones between shelves and continental slopes where the bathymetry leads to a reduction in cover rock thickness towards the center of the basin (Eisbacher, 1996; Langer & Schütte, 2002; Gillhaus & Horvath, 2008). Therefore, it is expected that the proximal portion of the extensional basin experiments a less intense salt mobilization, once the overburden package is thinner and, consequently, the lithostatic pressure is smaller. Due to the basinward deepening, the opposite behavior occurs in the distal portion. In this case, the Búzios Field is

more proximal to the coastline and exhibits a thinner and less mobilized salt package than occurs in Tupi and Sapinhoá/Lapa areas.

Despite the continued efforts acting on the basin during continental drift, in the study area, the major factor influencing the deformation of the post-salt package is the salt tectonics. This is concluded from the analysis of the observed structures and deformation patterns. Figure 7 clearly shows the outline of salt domes and diapirs by post-salt faults. Although halokinesis ceased during the Eo-Oligocene (Corrêa, 2009), most of the deformation of the post-salt package was conditioned by salt tectonics, even though there might be a component of deformation associated with the reactivation of syn-rift faults. The major difference between units Drift I and II is the amount of deformation. Once Drift I unit is greatly affected by the halokinesis, Drift II unit is a predominantly regular package, mostly affected by extensional efforts. Horizon 5, which separates Drift I and II units may mark the Late Cretaceous and Tertiary tectonic reactivation, which has resulted in increased salt tectonics (Meisling et al. 2001; Cobbold et al. 2011). This reactivation could explain the extensional faults in the throughout Drift II package since the halokinesis ceased during Eo-Oligocene in the Santos Basin (Corrêa, 2009).

Regarding the pre-salt section in the Sapinhoá/Lapa fields, the rifting faults intensely affect the Barra Velha Formation. In the Búzios Field region, only one of the main mapped faults affects this unit, while in the Sapinhoá Field, a great part of the interpreted faults crosses the entire Barra Velha package, reaching out to the base of the salt. The higher angle tilting of the syn-rift blocks observed in the Tupi area is also explained by its position within the tectonic components of the Santos Basin. The Tupi Field is located more distal from the continental margin than the Búzios area. Regarding the unit's thickness, the thicker Barra Velha Formation package observed in the Tupi Field may be a consequence of the southward widening of the rift, where great space of accommodation was generated by the time de post-rift sequence was deposited. However, it is important to highlight that besides de accommodation space, many parameters conditionate the carbonate precipitation, such as climate, Ph, base level, composition, and solubility of the lake. Besides that, only a few sections were analyzed for this comparison, thus the thickening of the Barra Velha Formation can be local and only a result of spots with a higher deposition rate.

By the same logic, it is reasonable to infer that the Sapinhoá/Lapa area also presents a thickening of the post-rift sequence, once it is also located eastwards of the Búzios Field. In the sections shown in Ribeiro da Silva et al. (2021), the salt package and the Barra Velha

Formation are thicker than in the Búzios Field area. However, it is important to highlight that besides de accommodation space, many parameters conditionate the salt precipitation, such as climate, Ph, base level, composition, and solubility (among others) of the evaporitic lake.

In the study area, four main sets of normal faults were mapped throughout the pre-salt section: N-S direction west-dipping, NE-SW direction northwest-dipping, NE-SW direction southeast-dipping, and W-E trend dipping to north. The NE-SW faults are probably related to the main fracturing trend of the South Atlantic rift, inherited from crystalline basement (Ribeira Belt) structures (Stanton et al. 2014), which generates the east-west displacement.

The W-S fault (yellow, Fig. 6) can be associated with a secondary (and posterior) trend caused by transfer zones. Mohriak & Fainstein (2012) after Asmus and Ferrari (1978) and Meisling et al. (2001) point out the W-E general trend suggests an oblique rift system marked by transfer zones, some of which were reactivated during the formation of oceanic fracture zones. At the eastern limit of continental crust, transfer zones become aligned with ocean ridge transform faults, which trend W-E across the South Atlantic (Meisling et al. 2001). Stanton et al. (2014) describe the presence of structural W-S trends predominant at the distal domain of the Santos Basin, with orientation subparallel to the South Atlantic fracture zones. This association is also made by Souza et al. (2007). This argument supports the hypothesis of the N-S faults being posterior to the rifting fault since it affects the post-rift I (Barra Velha Fm.) reaching out the base of salt.

One of the N-S fault sets (pink, Fig. 6) is deflected to NE. This deflection can be associated with the ENE to NE-trending deflection of about 1000 km long described by (Dehler et al. 2016; Szatmari & Milani, 2016). The aforementioned feature is produced by left-lateral transtensional tectonics in the rift, with a strong strike-slip component along NE-trending faults.

The occurrence of volcanic intrusions in the Santos Basin has been locally described. Fornero et al. (2019) describe the occurrence of approximately 400 meters of basaltic subaerial flows in the SE deepwater portion of Santos Basin, Brazil, at about 300 km from the coast. These flows were deposited during the post-rift phase and were covered by the evaporitic sequence of the Ariri Formation. Moreover, a thick and vertically-oriented intracrustal structure observed in the proximal portion of the Santos Basin is suggested as swarms of dikes with associated plugs, controlled by the NE-SW structures of the rift (Ferraz et al. 2018).

However, these volcanic flows were not mapped in the study area. At the research scale (2000m x 2000m), no features suggestive of volcanic intrusions were detected, but this does

not necessarily mean they are absent. Zálan et al. (2011) point out the Santos, Campos, and Espírito Santo basins as a typical example of a magma-poor passive margin. In sharp contrast, the Pelotas Basin situated in the south of the Florianópolis High is the classic example of a volcanic margin, with huge rifts filled mostly by volcanic material.

5.2.5.3.4 Sismostratigraphy and tectonic implications

In my research, I used 3D seismic, seismic attributes, and well-log data to characterize the Búzios Field in three dimensions. The major findings consist of the identification of six seismic units (A, B, C, D, E, and F), which correspond to the tectonic stages Syn-Rift I, Syn-Rift II, Post-Rift I, Post-Rift II, Drift I, and Drift II, respectively. Based on well data, units B, C, D, E, and F were correlated with the stratigraphy of the Santos Basin. Unit B corresponds to the Piçarras/Itapema interval, while unit C is associated with the Barra Velha Formation. Unit D represents the Ariri Fm, and unit E is related to the Guarujá and Itajaí-Açu formations, as well as the turbidites of the Ilhabela Member. Finally, unit F is associated with the Marambaia Formation shales and the turbidity flows of the Maresias Member.

To generate a 3D model, I interpolated five horizons (1, 2, 3, 4, and 5) and the main faults. From this model, important features were observed. For instance, the Syn-Rift I unit (economic basement) is deeper towards N-NW, whereas it is shallower towards S-SE. It occurs due to the presence of a half-grabens system of regional expression. This half-graben system is responsible for conditioning the entire pre-salt geometry and thickness, as the structural highs and lows generate more or less space for sediment accommodation. Although the Post-Rift I unit has a predominantly regular geometry and constant thickness, I noticed a tendency to thicken towards the S-SE and a slight downward flexure towards the NE in the southeast of the Búzios Field in the 3D model.

An important observation from the 3D model is the complex morphology of the Post-Rift II unit. The unit's thickness varies from zero in the NW part of the study area to 3,300 meters below the steep and thick domes and diapirs. Moving towards the SE, the unit's topography becomes more irregular, where thick anticlinal and synclinal features alternate. Towards the S-SE, the salt layer is thicker, and the domes are less steep.

The thickness of the Drift I unit is highly influenced by the salt morphology. In areas where the salt package is thin (in the north), the Drift I unit is thicker, reaching up to 3,600 meters. The top surface of this unit (horizon 5) is primarily flat but discontinuous due to the

presence of dip-slip faults. Lastly, the Drift II unit is characterized by a relatively constant thickness of about 500 meters, with minor variations in proximity to fault zones.

The 3D modeling of these units allowed the observation of many features that researchers often disregarded in studies conducted in the Santos Basin. Since most of these studies focus on characterizing the pre-salt reservoirs, many morphological and structural aspects are not investigated within the rest of the basin. Comparing my study area with the Tupi and Sapinhoá/Lapa fields, three important differences were found: the Post-Rift I layer (Barra Velha Fm.) and the Post-Rift II package (Ariri Fm.) are thicker and more mobilized than in the Búzios Field. In the Tupi Field, the pre-salt blocks are more rotated, and the internal reflectors have a higher inclination than in my study area. The evaporitic package seems less mobilized and thinner in the Búzios Field area than in Sapinhoá/Lapa and Tupi fields.

Four postulates were crucial to understanding the rifting mechanism responsible for the formation of the South Atlantic Ocean and the eastern Brazilian basins: (1) the clockwise rotation of South America relative to Africa about a pole located offshore NE Brazil; (2) the propagation of rifting from south to north; (3) the rifting process widened and deepened the South Atlantic basin towards the south, and (4) salt mobilization/maturity increases basinward. Based on these premises, I concluded that the increased mobilization of salt, higher post-rift package thickness, and increased syn-rift block rotation are associated with the relative distance from the continental margin and, consequently, with the amount of displacement generated by the South Atlantic Rift.

Since my work modeled a unit that spatially corresponds to the Barra Velha Formation, this opens up opportunities for future studies with greater detail focused on reservoir characterization. With a detailed interpretation grid, it is possible to model the carbonate mounds located right below the salt layer, which are known to be important traps for oil accumulation. Also, future works can be implemented in investigating the African counterpart of the Santos Basin to search for clues that determine which rifting mechanism was responsible for the opening of the basin.

5.2.6 Conclusions

In this study, I have characterized the Búzios Field in three dimensions using 3D seismic data, seismic attributes, and well-log data. The combined use of these tools enabled the understanding of important parameters within the tectonostratigraphic evolution of the Santos Basin. Specifically, I examined how the relative position of the study area concerning the

continental margin influences the amount of displacement observed in the region and how this positioning affects the mobilization and thickness of the salt package.

While most recent studies have focused on the reservoir characterization of the Búzios Field, my research aimed to understand how this area fits into the broader context of the evolution of the Santos Basin. Through the 3D model, I connected the observed features with the tectonic-stratigraphic evolution of the Búzios Field area, attempting to investigate how the opening of the rift and halokinesis impacted the current geometric and stratigraphic arrangement.

In an attempt to reconstruct the tectonic evolution of the Santos Basin in a regional approach, the mapped units were compared to their analogs within other oil fields situated in different positions within the basin. Comparing the study area with the Tupi and Sapinhoá/Lapa fields, three significant features were crucial to comprehend the rifting evolution within the Santos Basin. These features consist of thinner Post-Rift I (Barra Velha Fm.) and Post-Rift II (Ariri Fm.) layers and less mobilization in the Búzios Field. Additionally, the pre-salt blocks display minor rotation, and the internal reflectors demonstrate a smoother inclination in the study area when contrasted with these other fields. Considering the rift mechanisms and the most widely accepted models for the opening of the South Atlantic Rift, this research concludes that the reduced salt mobilization, post-rift package thickness, and rotation of the syn-rift blocks in the Búzios Field are associated with the relative distance from the continental margin and, thus, the magnitude of displacement caused by the South Atlantic Rift. In this context, the Búzios Field is positioned in closer proximity to the continental margin than the Tupi and Sapinhoá/Lapa fields, suggesting a lower level of displacement.

DECLARATION OF COMPETING INTEREST

The author declares to have no known competing financial interests or personal relationships that could have appeared to influence the work reported in this paper.

ACKNOWLEDGEMENTS

This article is part of the results of master research of Fernanda Moura Costa and is funded by Petrobras master's grant through the P&D project entitled "Inteligência artificial aplicada à exploração de petróleo na camada pré-sal" (n° 28184). This work was undertaken at the Federal University of Minas Gerais, Post-Graduation Program, Institute of Geosciences, Department of Geology (CPMTC-IGC-UFMG). The author specially thanks ANP for providing the data used in this study, and the DUG company for providing the DUG Insight

academic license used for seismic visualization, interpretation, and analysis. The author also thanks the SÍSMICA research group, especially Wagner Meira Teixeira, Jéssica Lia Santos da Costa, Tobias Fonte-Boa, Caique Pinheiro Carvalho, and Mariana Leite for all the support and discussions. Finally, the author thank Thiago Toríbio, Felipe Farias, and Andrea Damasceno from Petrobras for their support and constructive suggestions and ideas.

APPENDIX A - Models of Rifting Mechanisms

According to Bosence (1998), the four main types of rifting correspond to pure shear (Fig. A1-A), simple shear (Fig. A1-B), heterogeneous stretching (Fig. A1-C), and mantle plume-related (Fig. A1-D).

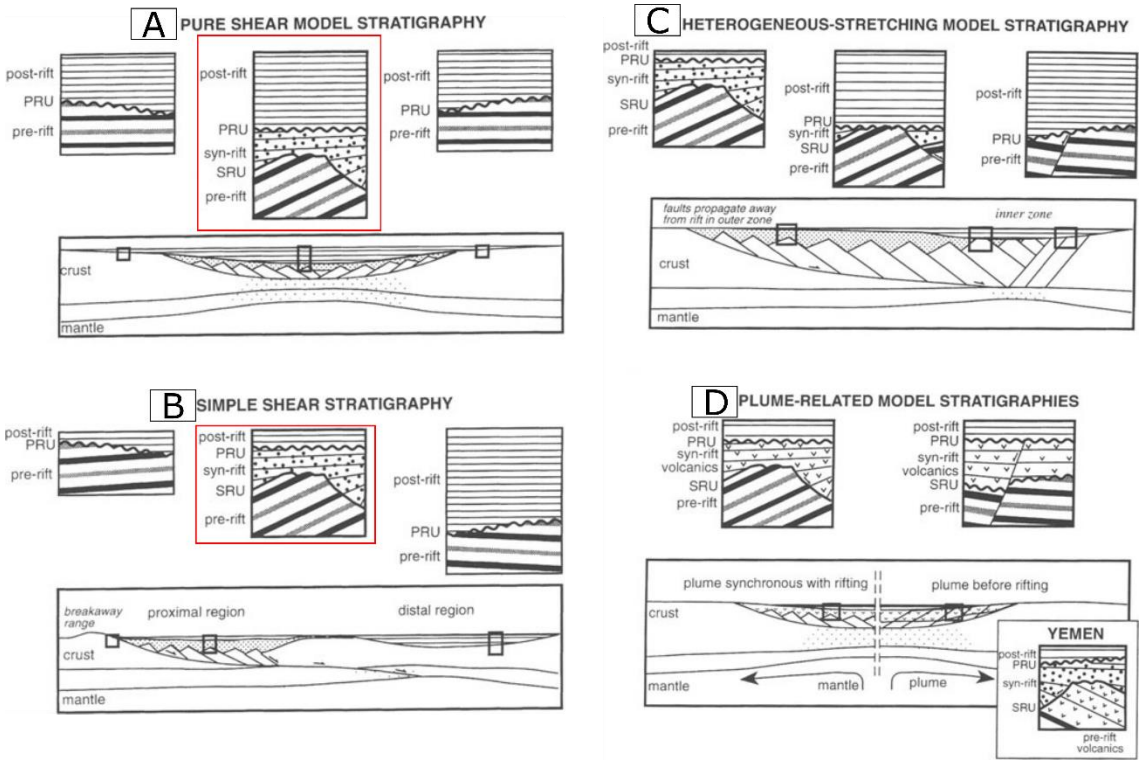

Figure A1 - Models of rifting and predicted nature of stratigraphic fills in rift basins resulting from pure shear (A), simple shear (B), heterogeneous stretching (E), and mantle plume (B). Extracted from Bosence (1998). The red dotted polygons suggest the infill configuration observed in the study area.

The model of development and evolution of rift basins of McKenzie (1978) defines three major stages. The first consists of a rapid stretching of continental lithosphere, which produces thinning and passive upwelling of hot asthenosphere, with block faulting and subsidence. Then the lithosphere thickens and subsidence turns slower. The author considers the stretching continuous and uniform during the rifting.

Wernicke (1985) proposes an alternative model of stretching the lithosphere by simple shear, in which the rifting starts from a shallowly inclined fault (or shear zone at depth). The

base of this theory is the occurrence of extensional allochthons zones with large displacement, which exhibit east-dipping, east-directed, low-angle normal faults, and wide shear zones gently. This model proposes that the crust's large-scale, uniform-sense, and normal simple shear is a reflex of what occurs with the entire lithosphere. Also, it predicts major lithospheric thinning without crustal thinning in plateau areas in the direction of crustal shear. The main trace of the simple-shear mechanism is the absence of evidence of extension in the lower lithosphere, but the presence in the upper and middle crust. The upper and middle-crustal extension is registered by regional low-angle detachments beneath normal fault systems and a subjacent zone of ductile deformation. The main clue of a simple-shear mechanism is pointed out as the detachment surfaces associated with the brittle-ductile transition.

APPENDIX B

Supplementary data to this article are presented in the attached files.

Declaration of Generative AI in scientific writing

During the preparation of this work, the author used GPT chat in order to improve language and vocabulary. After using this tool/service, the author(s) reviewed and edited the content as needed and take full responsibility for the content of the publication.

References

Abdullah, A.B., Murti, B.S., Sismanto. (2005). Karakterisasi Reservoar Menggunakan Analisis Atribut Seismik Di Lapangan Abas Cekungan Kutai Kalimantan Timur. Jurnal Fisika Indonesia N°.28 Vol.IX Edition. P. 127-140. In: Pamungkas, T.D., Nandi, Ridwana, R. (2021). Conceptual interpretation seismic 3d using rms amplitude and dip-azimuth attribute analysis for identification structure and facies model in physical geographic. International Geography Seminar 2019. IOP Conf. Series: Earth and Environmental Science 683 (2021) 012055.

Adriano, M.S., Figueiredo, J.P., Coelho, P.H.G.R., Borghi, L. (2022). Tectonic and stratigraphic evolution of the Santos Basin rift phase: New insights from seismic interpretation on Tupi oil field area. Journal of South American Earth Sciences 116 (2022) 103842.

Anselmetti, F.S., Eberli, G.P. (1993). Controls on Sonic Velocity in Carbonates. Pure and Applied Geophysics, Vol. 141, No. 2/3/4.

Arai, M., Viviers, M.C. (2013). Dinoflagellate cyst superdominance assemblages from the Upper Cretaceous of the Santos Basin, offshore SE Brazil, and their palaeoecological significance. In: Lewis, J. M., Marret, F., Bradley, L. (2013). Biological and Geological Perspectives of Dinoflagellates. The Micropalaeontological Society, Special Publications. Geological Society, London, 285–292.

Armstrong, R.L. (1982). Cordilleran metamorphic core complexes from Arizona to southern Canada. Annual Review of Earth and Planetary Sciences, 10, p. 129-154.

Asmus, H.E., Ferrari, A.L. (1978). Hipótese sobre a causa do tectonismo cenozo´ico na regia˜o sudeste do Brasil. Se´rie Projeto Remac 4, 75–88.

Assine, M.L., Corrêa, F.S., Chang, H.K. (2008). Migração de depocentros na Bacia de Santos: importância na exploração de hidrocarbonetos. Revista Brasileira de Geociências. 38 (2 - suplemento): 111-127.

Bosence, D.W.J. (1998). “Stratigraphic and sedimentological models of rift basins”. Sedimentation and Tectonics of Rift Basins: Red Sea-Gulf of Aden. Edited by B.H. Purser and D.W.J. Bosencc. Published in 1998 by Chapman & Hall, London.

Brown, A. (2011). Interpretation of Three-Dimensional Seismic Data. 7th Edition, APG Memoir 42 SEG Investigations in Geophysics, N°. 9.

Buckley, J. D.; Bosence, D. W.; Elders, C. F. (2015). Tectonic setting and stratigraphic architecture of an Early Cretaceous lacustrine carbonate platform, Sugar Loaf High, Santos Basin, Brazil. Geological Society, London, Special Publications, 418, p 1–17, 2015.

Cainelli, C., Mohriak, W.U. (1998). Geology of Atlantic Eastern Brazilian basins. 1998. In: AAPG, International Conference & Exhibition Short Course – Brazilian Geology Part II, Rio de Janeiro, Brazil, 67 p.

Cainelli, C.C., Mohriak, W.U. (1999b). Some remarks on the evolution of sedimentary basins along the Eastern Brazilian continental margin. Episodes, 22:206-216.

Castro, T. M., Lupinacci, W. M. (2019). Evaluation of fine grains in pre-salt reservoirs. Sixteenth International Congress of the Brazilian Geophysical Society. Rio de Janeiro, Brazil, August 2019.

Castro, T.M. (2019). Avaliação dos reservatórios carbonáticos do pré-sal no Campo de Búzios, Bacia de Santos. Dissertação de Mestrado em Geologia e Geofísica. Universidade Federal Fluminense, Niterói. 183p.

Chang, H.K., Assine, M.L., Corrêa, F.S., Tinen, J.S., Vidal, A.C., Koike, L. (2008). Sistemas petrolíferos e modelos de acumulação de hidrocarbonetos na Bacia de Santos. Revista Brasileira de Geociências, 38(2 - suplemento): 29-46.

Chopra, S., Marfurt, K.J. (2007). Seismic Attributes for Prospect Identification and Reservoir Characterization. 1. ed. Tulsa: Society of Exploration Geophysicists, v. 2.

Cobbold, P. R., Meisling, K.E.M, Mount, V.S. (2001). Reactivation of an obliquely-rifted margin, Campos and Santos basins, southeastern Brazil: AAPG Bulletin, v. 85, no. 11, p. 1925–1944.

Corrêa, F.S. (2009). Evolução halocinética da região centro-norte da Bacia de Santos, Brasil. Dissertação de Doutorado em Geociências e Meio Ambiente. Instituto de Geociências e Ciências Exatas, Universidade Estadual Paulista, 308p.

Dehler, N.M., Magnavita, L.P., Gomes, L.C., Rigoti, C.A., Bach de Oliveira, J.A., Sant’Anna, M.V. (2016). The “Helmut” geophysical anomaly: a regional left lateral transtensional shear zone system connecting Santos and Campos basins, southeastern Brazil. Mar. Pet. Geol. 72, 412-422.

Dias, A.L.L., Lima, M.V.A.G., Frigo, E. (2019). Análise e interpretação de atributos sísmicos instantâneos: uma contribuição ao estudo do arcabouço tectônico-estrutural da Bacia de Pelotas. 16th International Congress of the Brazilian Geophysical Society, Rio de Janeiro, Brazil,

Dias, R.M., Castro, T.M., Lupinacci, W. M., Santos, M.A.C. (2019). Understanding the relationship between acoustic impedance and porosity in the presalt of the Buzios Field Santos Basin. First EAGE Workshop on Pre-Salt Reservoir. December 2019, Rio de Janeiro, Brazil.

DUG Insight (version 4.7). (2020). Windows/Linux/Mac. Perth, Western Australia: DUG Technology Ltd.

Eisbacher, G.H. (1996): Einführung in die Tektonik: 374 S., Stuttgart. In: Gillhaus, A., Horvath, P.L. (2008). Compilation of geological and geotechnical data of worldwide domal salt deposits and domal salt cavern fields. Research Project Report N°. 2007-1-SMRI. KBB Underground Technologies GmbH, Hannover.

Farias, F., Szatmari, P., Bahniuk, A., França, A.B. (2019). Evaporitic carbonates in the pre-salt of Santos Basin – Genesis and tectonic implications. Marine and Petroleum Geology. 105 (2019) 251–272.

Ferraz, A.E.P.P.D., Ferrari, A.L., Aristizábal, C., Guimarães, P.B.M. (2018). Estrutura magnética crustal sob os campos petrolíferos do pré-sal ee sua relação com o magmatismo – Bacia De Santos. 49º Congresso Brasileiro de Geologia, 20 a 24 de agosto de 2018 – Rio de Janeiro.

Ferreira, D.J.A. (2022). Advanced Techniques for 3D Reservoir Characterization: Models for the Buios Field, Santos Basin. Dissertação de Doutorado. Universidade Federal Fluminense, Niterói. 117p.

Ferreira, D.J.A., Dias, R.M., Lupinacci, W.M. (2021). Seismic pattern classification integrated with permeability-porosity evaluation for reservoir characterization of salt carbonates in the Buzios Field, Brazil. Journal of Petroleum Science and Engineering 201-108441.

Fornero, S.A., Marins, G.M., Lobo, J.T., Freire, A.F.M., de Lima, E.F. (2019). Characterization of subaerial volcanic facies using acoustic image logs: Lithofacies and log-facies of a lava-flow deposit in the Brazilian pre-salt, deepwater of Santos Basin. Marine and Petroleum Geology.

Gambôa, L., Machado, M., Silveira, De Freitas, J., Da Silva, S. (2008). Evaporitos estratificados no Atlantico Sul: Interpretação sísmica e controle tectono-estratigráfico na Bacia de Santos, in Mohriak, W., et al., eds., Sal: Geologia e Tectonica, Exemplos nas Basicas Brasileiras: São Paulo, Brasil, Beca Edições Ltd., p. 340–359.

Gillhaus, A., Horvath, P.L. (2008). Compilation of geological and geotechnical data of worldwide domal salt deposits and domal salt cavern fields. Research Project Report N°. 2007-1-SMRI. KBB Underground Technologies GmbH, Hannover.

Girão, G. (2013). Perfilagem Geofísica em Poço Aberto: Fundamentos básicos com ênfase em petróleo. Sociedade Brasileira de Geofísica – SBGf Rio de Janeiro. 222p.

Guerra, M. C. M., & Underhill, J. R. (2012). Role of halokinesis in controlling structural styles and sediment dispersal in the Santos Basin, offshore Brazil. Geological Society Special Publications, 363(1), 175-206.

Heilbron, M., Mohriak, W., Valeriano, C.M., Milani, E., Almeida, J.C.A., Tupinamba, M.. (2000). From collision to extension: the roots of the southeastern continental margin of Brazil. In: Mohriak, W.U., Talwani, M. (Eds.), Atlantic rifts and Continental Margins, American Geophysical Union Geophysical Monograph 115, pp. 1-32.

Jackson, M.P.A, Talbot, C.J. (1991). A Glossary of Salt Tectonics, by M. P.A. Jackson and C. J. Talbot. 44p. In: Gillhaus, A., Horvath, P.L. (2008). Compilation of geological and geotechnical data of worldwide domal salt deposits and domal salt cavern fields. Solution Mining Research Institute Report, Clarks Summit, PA, USA. 100p.

Kuchle, J. (2010). Análise tectono-estratigráfica de bacias rifte. Dissertação de Doutorado. Programa de Pós-Graduação em Geociências, Instituto de Geociências, Universidade Federal do Rio Grande do Sul. 198p.

Langer, A., Schütte, H. (2002): Geologie norddeutscher Salinare. – Veröffentl. Akad. Geowiss. Hannover, 20: 63-69, Hannover. In: Gillhaus, A., Horvath, P.L. (2008). Compilation of geological and geotechnical data of worldwide domal salt deposits and domal salt cavern fields. Research Project Report N°. 2007-1-SMRI. KBB Underground Technologies GmbH, Hannover.

Macedo, P.H.C., Barretto, D.R., Neves, I.A., Abrantes Junior, F.R., Lupinacci, W.M. (2021). Seismic Interpretation of presalt carbonate reservoirs of the Búzios Field, Santos Basin. 17th International Congress of the Brazilian Geophysical Society held in Rio de Janeiro, Brazil, 16-19August 2021.

Marfurt, K.J., Kirlin, R.L., Farmer, S.L., Bahorich, M.S. (1998). 3-D seismic attributes using a semblance-based coherency algorithm. GEOPHYSICS, Vol. 63, N°. 4 - P. 1150-116.

Maul, A., Fonseca, J., Teixeira, L., Barros, P., Boechat, J., Nunes, J.P., Yamamoto, T., González, M., González, G. (2018a). Modelling intra-salt layers when building velocity models for depth migration Examples of the Santos Basins, Brazilian offshore. In: 88th Annual Meeting. Anaheim – CA, USA. SEG Technical Program Expanded Abstracts 2018. Society of Exploration Geophysicists, p. 3764–3767.

Mckenzie, D. (1978). Some remarks on the development of sedimentary basins. Earth Planet Sci Lett, v. 40, p. 25–32.

Meisling, K.E., Cobbold, P.R., Mount, V.S. (2001). Segmentation of an obliquely rifted margin, Campos and Santos basins, southeastern Brazil. AAPG Bull. 85 (11), 1903–1924.

Mesquita, F.C., Santos, M.A.C., Maul, A.R., Bordignon, A.L. (2021). New method of seismofacies identification using machine learning over seismic attributes applied to salt stratifications. Brazilian Journal of Geophysics, 39(1).

Milani, E.J., Brandão, J.A.S.L, Zalán, P.V., Gamboa, L.A.P. (2000). Petróleo Na Margem Continental Brasileira: Geologia, Exploração, Resultados e Perspectivas. Brazilian Journal of Geophysics, Vol. 18(3).

Mio, E. de; Chang, H. K.; Corrêa, F. S. (2005). Integração de métodos geofísicos na modelagem crustal da Bacia de Santos. Revista Brasileira de Geofísica, v. 23, n. 3, p. 275-284.

Mitchell, D.J.W., Allen, R.B., Salama, W., Abouzakm, A. (1992). tectonostratigraphic framework and hydrocarbon potential of the Red Sea. Journal of Petroleum Geology, Vol. 15 (2), p.187-210.

Mohriak, W.U. and Fainstein, R. (2012) Phanerozoic Regional Geology of the Eastern Continental Margin of Brazil. In: Roberts, D.G. and Bally, A.W. (Eds.) Regional Geology and Tectonics: Phanerozoic Passive Margins, Cratonic Basins and Global Tectonic Maps. The Netherlands, 1 Amsterdam, The Netherlands: Elsevier, 222–283.

Mohriak, W.U., Szatmari, P., Anjos, S. (2008). "Sal Geologia e Tectônica. Exemplos nas Bacias Brasileiras"; Beca Edições Ltda. In: Justen, J.R.C, Vargas Jr., E.A., Alves, I., Souza, A.L.S. (2013). Análise das propriedades elásticas de rochas e minerais evaporíticos. 13th International Congress of the Brazilian Geophysical Society held in Rio de Janeiro, Brazil, August 26-29, 2013.

Moreira, J.L.P., Madeira, C. V., Gil, J. A., Machado, M. A. P. (2007). Bacia de Santos. Boletim de Geociências da Petrobras, v. 15, n. 2, p. 531-549.

Neves, I.A., Lupinacci, W.M., Ferreira, D.F.A., Zambrini, J.P.R., Oliveira, L.O.A., Olho-Azul, M., Ferrari, A.L., Gamboa, L.A.P. (2019). Presalt reservoirs of the Santos Basin: cyclicity, electrofacies and tectonic-sedimentary evolution. Interpretation, 7(4):1-37.

Obafemi, S., Oyedele, K.F., Omeru, T., Bankole, S.I. (2020). Characterization of deep water turbidite channels and submarine fan lobes using artificial intelligence; Case study of Frem Field deep offshore Niger Delta, Journal of African Earth Sciences.

Oliveros, R.B., Radovich, B.J. (1997). Image-processing display techniques applied to seismic instantaneous attributes over the Gorgon gas field, North West Shelf, Australia. SEG Technical Program Expanded Abstracts: 2064-2067.

Papaterra, G.E.Z. (2010). Pre-salt: geological concepts on a new exploratory frontier in Brazil. Dissertação de Mestrado em Geologia. Programa de Pós-Graduação em Geologia, Instituto de Geociências, Universidade Federal do Rio de Janeiro. 81p.

Pereira, M.J., Macedo, J.M. (1990). A Bacia de Santos: perspectivas de uma nova província petrolífera na plataforma continental sudeste brasileira. Boletim de Geociências da Petrobras, 4(1), 3-11.

Prosser, S. (1993). Rift-related linked depositional systems and their seismic expression. Geological Society, London, Special Publications 1993, v.71; p35-66.

Rabinowitz, P.D., Labrecque, J. (1979). The Mesozoic South Atlantic Ocean and the evolution of its continental margins. Journal of Geophysical Research: Solid Earth, v. 84, n. B11, p. 5973-6002.

Ribeiro da Silva, S.F.C., Figueiredo, J.J.P., Coelho, P.H., Borghi, L. (2021). Evolução tectonoestratigráfica da Formação Barra Velha na área dos campos de Lapa e Sapinhoá, Bacia de Santos – Brasil. São Paulo, UNESP, Geociências, v. 40, n. 1, p. 55 – 69.

Schmidt, R.O.R. (2013). Análise das respostas de atributos sísmicos dos carbonatos Barremiano, Albiano e Neógeno no Campo de Bonito, Bacia de Campos- RJ. Trabalho de Conclusão de Curso. Universidade Estadual Paulista. 81p.

Silva, H.P.N. (2012). Caracterização e Delimitação de Reservatórios Usando Atributos Sísmicos. Dissertação de Mestrado. Universidade de Aveiro, Portugal. 114p.

Souza, B.P.E. (2021). Estudo de alguns atributos sísmicos para a caracterização estrutural: Aplicação na bacia de Taranaki, Nova Zelândia. Trabalho de Conclusão de Curso. Universidade Federal Fluminense, Niterói. 59p.

Souza, I.A., Ebert. H.D., Castro, J.C., Silva, G.H.T. (2007). A influência das falhas de transferência na porção norte da Bacia de Santos na formação de armadilhas capazes de conter hidrocarbonetos. 4° PDPETRO, Campinas, SP. 1.1.0063-1 – 2.

Souza, L.S., Sgarbi, G.N.C. (2016). Bacia de Santos: de promissora a principal bacia produtora de hidrocarbonetos do Brasil. XLVIII Congresso Brasileiro de Geologia. Porto Alegre, Brasil.

Souza, L.S., Sgarbi, G.N.C. (2019). Bacia de Santos no Brasil: geologia, exploração e produção de petróleo e gás natural. Boletín de Geología, 41(1), 175-195.

Stanton, N., Ponte-Neto, C., Bijani, R., Masini, E., Fontes, S., Flexor, J.M. (2014). A geophysical view of the Southeastern Brazilian margin at Santos Basin: insights into rifting evolution. J. S. Am. Earth Sci. 55, 141–154.

Szatmari, P., Milani, E.J. (2016). Tectonic control of the oil-rich large igneous-carbonate-salt province of the South Atlantic rift. Marine and Petroleum Geology 77 (2016) 567-596.

Taner, M.T. (2001). Seismic Attributes. Recorder, Canadian Society of Exploration Geophysicists, 26(7): 48-56.

Taner, M.T., Koehler, F., Sherié, R.E. (1979). Complex seismic trace analysis: Geophysics, 44, 1041-1063.

Tavares dos Santos, P., Gordon, A. C. (2021). Búzios field: Geological setting of the largest pre-salt field, Santos Basin, Brazil, in Marcio R. Mello, Pinar O. Yilmaz, and Barry J. Katz, eds., The supergiant Lower Cretaceous pre-salt petroleum systems of the Santos Basin, Brazil: AAPG Memoir 124, p. 375–394.

Wernicke, B. (1985). Uniform sense normal simple shear of the continental lithosphere. Can. J. Earth Sci. 22 (1), 108-125.

Zalán, P.V., Severino, M.D.C. G., Rigoti, C.A., Magnavita, L.P., Oliveira, J.A.B., Vianna, A.R. (2011). An entirely new 3D-view of the crustal and mantle structure of a South Atlantic passive margin–Santos, Campos and Espírito Santo basins, Brazil. In: AAPG Annual Conference And Exhibition, 2011. Houston. Actas....Houston: AAPG, v. 10, n. 13.

6 CONCLUSÕES E RECOMENDAÇÕES FUTURAS

Neste estudo, caracterizei o Campo de Búzios em três dimensões usando dados sísmicos 3D, atributos sísmicos e dados de poços. O uso combinado dessas ferramentas possibilitou a compreensão de parâmetros importantes dentro da evolução tectonoestratigráfica da Bacia de Santos. Tais parâmetros revelam como a posição da área de estudo em relação à margem continental brasileira influencia a quantidade de deslocamento observada na região e como esse posicionamento afeta a mobilização e espessura do pacote de sal.

Para gerar um modelo 3D, foram interpolados cinco horizontes (1, 2, 3, 4 e 5) e as principais falhas. A partir desse modelo, puderam ser observadas características importantes. Por exemplo, a unidade Sin-Rifte I (embasamento econômico) apresenta maior profundidade em direção a N-NW, enquanto é mais rasa em direção a S-SE. Isso ocorre devido à presença de um sistema de semi-grabens de expressão regional, limitado por falhas que mergulham para N-NW. Esse sistema de semi-grabens é responsável por influenciar toda a geometria e espessura do pré-sal, uma vez que as elevações e depressões estruturais criam mais ou menos espaço para a acomodação de sedimentos. Embora a unidade Pós-Rifte I tenha uma geometria predominantemente regular e espessura constante, pôde-se observar uma tendência de aumento de espessura em direção a S-SE e uma leve flexão descendente em direção a NE, no sudeste do Campo de Búzios.

Uma observação importante do modelo 3D é a morfologia complexa da unidade Pós-Rifte II (sal). A espessura dessa unidade varia de zero na parte NW da área de estudo a 3300 metros abaixo de domos íngremes e diápiros espessos. Conforme se avança em direção ao sudeste, a topografia dessa unidade torna-se mais irregular, alternando entre anticlinais e sinclinais espessos. Em direção a S-SE, a camada de sal é mais espessa e os domos são menos íngremes.

A espessura da unidade Drifte I é altamente influenciada pela morfologia do sal. Em áreas onde o pacote de sal é fino (no norte), a unidade Drifte I é mais espessa, chegando a atingir 3600 metros. A superfície superior dessa unidade (horizonte 5) é predominantemente plana, mas apresenta descontinuidades devido à presença de falhas normais. Por fim, a unidade Drifte II é caracterizada por uma espessura relativamente constante de cerca de 500 metros, com pequenas variações nas proximidades de zonas de falha.

A modelagem 3D dessas unidades permitiu a observação de muitas características que geralmente são negligenciadas em estudos realizados na Bacia de Santos. Como a maioria desses estudos se concentra na caracterização dos reservatórios pré-sal, muitos aspectos

morfológicos e estruturais não são investigados nas demais regiões da bacia. Ao comparar a área de estudo com os campos de Tupi e Sapinhoá/Lapa, foram identificadas três diferenças importantes: a camada Pós-Rifte I (Formação Barra Velha) e o pacote Pós-Rifte II (Formação Ariri) são mais espessos e mais mobilizados que no Campo de Búzios. No Campo de Tupi, os blocos pré-sal estão mais rotacionados e os refletores internos apresentam maior inclinação em comparação com a área de estudo. O pacote evaporítico parece ser menos mobilizado e mais fino na área do Campo de Búzios em relação aos campos de Sapinhoá/Lapa e Tupi.

Quatro pressupostos foram fundamentais para compreender o mecanismo de rifte responsável pela formação do Oceano Atlântico Sul e das bacias da margem leste brasileira: (1) a rotação no sentido horário da América do Sul em relação à África, em torno de um polo localizado offshore no nordeste do Brasil; (2) a propagação do rifte de sul para norte; (3) o processo de rifte alargou e aprofundou a bacia do Atlântico Sul em direção ao sul e (4) a mobilização/maturação do sal aumenta em direção à bacia. Com base nesses pressupostos, conclui-se que a maior mobilização do sal, maior espessura do pacote pós-rifte e aumento da rotação dos blocos syn-rift estão associados à distância relativa da margem continental e, consequentemente, à quantidade de deslocamento gerada pelo Rifte do Atlântico Sul.

Uma vez que meu trabalho modelou espacialmente a Formação Barra Velha, isso abre oportunidades para estudos futuros com maior detalhamento, focados na caracterização do reservatório. Com uma interpretação de maior detalhe, é possível modelar os *mounds* carbonáticos localizados logo abaixo da camada de sal, que são conhecidos por serem armadilhas importantes para a acumulação de petróleo. Além disso, futuros trabalhos podem ser implementados para investigar a contraparte africana da Bacia de Santos, em busca de pistas que determinem qual mecanismo de rifte foi responsável pela abertura da bacia.

Enquanto a maioria dos estudos recentes tem se concentrado na caracterização do reservatório do Campo de Búzios, minha pesquisa teve como objetivo entender como essa área se encaixa no contexto mais amplo da evolução da Bacia de Santos. Através do modelo 3D, características observadas foram relacionadas à evolução tectonoestratigráfica da área do Campo de Búzios, buscando investigar como a abertura do rifte e a halocinese impactaram a disposição geométrica e estratigráfica atual.

REFERÊNCIAS

Almeida, F.F.M., Hasui, Y. (1984). O Pré-Cambriano do Brasil. Edgard Blucher, 378 p.

ANP (2016). Plano de Desenvolvimento Aprovado Reunião de Diretoria nº 832 de 18/02/2016 – Resolução nº 093/2016.

ANP (2017). Bacia de Santos: Sumário Geológico e Setores em Oferta. Rodada 15, Agência Nacional do Petróleo, Gás Natural e Biocombustíveis.

ANP (2019). Oil and Natural Gas Production Bulletin. Production Development Superintendence.

Barbosa, M.R.S. (2022). Análise de agrupamentos de dados sísmicos 3D para detecção de indicadores diretos de hidrocarbonetos. Trabalho de Graduação em Geofísica. Instituto de Geociências, Universidade Federal da Bahia, Bahia. 80p.

Brown, A. (2011). Interpretation of Three-Dimensional Seismic Data. 7th Edition, APG Memoir 42 SEG Investigations in Geophysics, N°. 9.

Buckley, J. D.; Bosence, D. W.; Elders, C. F. (2015). Tectonic setting and stratigraphic architecture of an Early Cretaceous lacustrine carbonate platform, Sugar Loaf High, Santos Basin, Brazil. Geological Society, London, Special Publications, 418, p 1–17, 2015.

Campos Neto, M.C., Figueiredo, M.C.H. (1995). The Rio Doce Orogeny, Southeastern Brazil. Journal of South American Earth Sciences, 8, 2, 143-162.

Castro, T.M. (2019). Avaliação dos reservatórios carbonáticos do pré-sal no Campo de Búzios, Bacia de Santos. Dissertação de Mestrado em Geologia e Geofísica. Universidade Federal Fluminense, Nitetói. 183p.

Chang, H.K., Assine, M.L., Corrêa, F.S., Tinen, J.S., Vidal, A.C., Koike, L. (2008). Sistemas petrolíferos e modelos de acumulação de hidrocarbonetos na Bacia de Santos. Revista Brasileira de Geociências, 38(2 - suplemento): 29-46.

Chopra, S., Marfurt, K.J. (2007). Seismic Attributes for Prospect Identification and Reservoir Characterization. 1. ed. Tulsa: Society of Exploration Geophysicists, v. 2.

DUG Insight (version 4.7). (2020). Windows/Linux/Mac. Perth, Western Australia: DUG Technology Ltd.

Ferreira, D.J.A. (2022). Advanced Techniques for 3D Reservoir Characterization: Models for the Buios Field, Santos Basin. Dissertação de Doutorado. Universidade Federal Fluminense, Niterói. 117p.

Heilbron, M., Mohriak, W., Valeriano, C.M., Milani, E., Almeida, J.C.A., Tupinamba, M.. (2000). From collision to extension: the roots of the southeastern continental margin of Brazil. In: Mohriak, W.U., Talwani, M. (Eds.), Atlantic rifts and Continental Margins, American Geophysical Union Geophysical Monograph 115, p. 1-32.

Heilbron, M., Valeriano, C.M., Valladares, C.S., Machado, N. (1995). A orogênese brasiliana no segmento central da Faixa Ribeira, Brasil. Revista Brasileira de Geociências, 25, 4, 249-266.

Milani, E.J., Brandão, J.A.S.L, Zalán, P.V., Gamboa, L.A.P. (2000). Petróleo Na Margem Continental Brasileira: Geologia, Exploração, Resultados e Perspectivas. Brazilian Journal of Geophysics, Vol. 18(3).

Mio, E. de; Chang, H. K.; Corrêa, F. S. (2005). Integração de métodos geofísicos na modelagem crustal da Bacia de Santos. Revista Brasileira de Geofísica, v. 23, n. 3, p. 275-284.

Mohriak, W.U. (2003). Bacias Sedimentares da Margem Continental Brasileira. In: Geologia, tectônica e recursos minerais do Brasil: texto, mapas & SIG organizadores, Luiz Augusto Bizzi, Carlos Schobbenhaus, Roberta Mary Vidotti, João Henrique Gonçalves – Brasília : CPRM – Serviço Geológico do Brasi, 2003. 692 p.

Mohriak, W.U. and Fainstein, R. (2012) Phanerozoic Regional Geology of the Eastern Continental Margin of Brazil. In: Roberts, D.G. and Bally, A.W. (Eds.) Regional Geology and Tectonics: Phanerozoic Passive Margins, Cratonic Basins and Global Tectonic Maps. The Netherlands, 1 Amsterdam, The Netherlands: Elsevier, 222–283.

Moreira, J.L.P., Madeira, C. V., Gil, J. A., Machado, M. A. P. (2007). Bacia de Santos. Boletim de Geociências da Petrobras, v. 15, n. 2, p. 531-549.

Oliveros, R.B., Radovich, B.J. (1997). Image-processing display techniques applied to seismic instantaneous attributes over the Gorgon gas field, North West Shelf, Australia. SEG Technical Program Expanded Abstracts: 2064-2067.

Papaterra, G.E.Z. (2010). Pre-salt: geological concepts on a new exploratory frontier in Brazil. Dissertação de Mestrado em Geologia. Programa de Pós-Graduação em Geologia, Instituto de Geociências, Universidade Federal do Rio de Janeiro. 81p.

Rigoti, C. A. (2015). Evolução tectônica da Bacia de Santos com ênfase na geometria crustal: Interpretação integrada de dados de sísmica de reflexão e refração, gravimetria e magnetometria. Dissertação de Mestrado em Geologia. Programa de PósGraduação em Análise de Bacias e Faixas Móveis, Centro de Tecnologia e Ciências, Faculdade de Geologia, Universidade do Estado do Rio de Janeiro, Rio de Janeiro. 135p.

Sheriff, R.E. (2002). Encyclopedic Dictionary of Applied Geophysics. 4th Edition, Geophysical references, v. 13.

Sibson, R. (1981). A brief description of natural neighbor interpolation (Chapter 2). In V. Barnett (ed.). Interpreting Multivariate Data. Chichester: John Wiley. p. 21–36.

Souza, L.S., Sgarbi, G.N.C. (2019). Bacia de Santos no Brasil: geologia, exploração e produção de petróleo e gás natural. Boletín de Geología, 41(1), 175-195.

Szatmari, P., Milani, E.J. (2016). Tectonic control of the oil-rich large igneous-carbonate-salt province of the South Atlantic rift. Marine and Petroleum Geology 77 (2016) 567-596.

Taner, M.T. (2001). Seismic Attributes. Recorder, Canadian Society of Exploration Geophysicists, 26(7): 48-56.

Taner, M.T., Koehler, F., Sherié, R.E. (1979). Complex seismic trace analysis: Geophysics, 44, 1041-1063.

Tavares dos Santos, P., Gordon, A. C. (2021). Búzios field: Geological setting of the largest pre-salt field, Santos Basin, Brazil, in Marcio R. Mello, Pinar O. Yilmaz, and Barry J. Katz, eds., The supergiant Lower Cretaceous pre-salt petroleum systems of the Santos Basin, Brazil: AAPG Memoir 124, p. 375–394.

Toolbox 2.3. (1999-2007). Schlumberger Technology Corporation.

Trompette, R. (1994). Geology of Western Gondwana (2000-500 Ma). A. A. Balkema,Rotterdam, 350 p.

APÊNDICES

Apêndice A – Tabela Suplementar 1: Resultado Estatística do poço 2-ANP-1-RJS

WELL	UNIT		Gamma-Ray (GAPI)	Density (g/cm^3)	P-Sonic (us/ft)	Resistivity (Ohm*m)
		Filter	Trimmed mean 25%			
2-ANP-1-RJS	B (Syn-Rift II)	Min	7,0252	2,2747	56,9805	3,6253
		Max	118,4600	2,6157	72,9812	1761,3000
		Mean	20,1180	2,4696	63,3061	435,1950
		Std dev	23,7102	0,0648	3,9064	417,5930
	C (Post-Rift I)	Min	0	2,2830	48,7279	64,1255
		Max	59,1938	2,7268	73,3901	1331,7400
		Mean	23,3872	2,5870	57,1368	405,1530
		Std dev	9,4011	0,1098	6,5318	246,0150
	D (Post-Rift II)	Min	0	1,6183	51,9219	–
		Max	129,1600	4,6288	91,8937	
		Mean	17,8008	2,1529	67,6862	
		Std dev	16,0095	0,3923	3,3650	
	E (Drift I)	Min	9,9918	–	53,1278	–
		Max	64,0438		160,021	
		Mean	43,5808		125,121	
		Std dev	9,0162		20,1439	
	F (Drift II)	Min	20,5473	–	–	–
		Max	57,9520			
		Mean	38,5900			
		Std dev	12,2577			

Apêndice B – Tabela Suplementar 2: Resultado Estatística do poço 3-BRSA-1053-RJS

WELL	UNIT		Gamma-Ray (GAPI)	Density (g/cm^3)	P-Sonic (us/ft)	Resistivity (Ohm*m)
		Filter	Trimmed mean 25%			
8-BUZ-20-RJS	B (Syn-Rift II)	Min	8,8522	2,2751	50,2789	0,7400
		Max	99,7198	2,6989	77,9641	1154,5700
		Mean	25,0484	2,5176	62,2728	127,7250
		Std dev	19,9676	0,0918	5,6079	265,7230
	C (Post-Rift I)	Min	9,4623	2,0988	52,7409	0.9307
		Max	41,2175	2,6516	75,1289	1904,5800
		Mean	17,7954	2,4959	62,4661	649,4110
		Std dev	5,3792	0,0818	5,1455	530,9180
	D (Post-Rift II)	Min	8,2761	–	53,8903	0,9426
		Max	191,8390		88,0562	5010,9500
		Mean	27,7429		68,6486	3841,7200
		Std dev	17,4453		4,5604	1768,6300
	E (Drift I)	Min	21,1253	–	57,1587	0,3149
		Max	102,2000		107,766	29,2680
		Mean	53,8759		94,4055	0,8761
		Std dev	11,0604		8,0473	1,0969
	F (Drift II)	Min	31,9157	–	–	0,6922
		Max	66,9203			0,8260
		Mean	50,3074			0,7596
		Std dev	7,6621			0,0373

Apêndice C – Tabela Suplementar 3: Resultado Estatística do poço 8-BUZ-20-RJS

WELL	UNIT		Gamma-Ray (GAPI)	Density (g/cm^3)	P-Sonic (us/ft)	Resistivity (Ohm*m)
		Filter	Trimmed mean 25%			
8-BUZ-20-RJS	B (Syn-Rift II)	Min	8,8522	2,2751	50,2789	0,7400
		Max	99,7198	2,6989	77,9641	1154,5700
		Mean	25,0484	2,5176	62,2728	127,7250
		Std dev	19,9676	0,0918	5,6079	265,7230
	C (Post-Rift I)	Min	9,4623	2,0988	52,7409	0.9307
		Max	41,2175	2,6516	75,1289	1904,5800
		Mean	17,7954	2,4959	62,4661	649,4110
		Std dev	5,3792	0,0818	5,1455	530,9180
	D (Post-Rift II)	Min	8,2761	–	53,8903	0,9426
		Max	191,8390		88,0562	5010,9500
		Mean	27,7429		68,6486	3841,7200
		Std dev	17,4453		4,5604	1768,6300
	E (Drift I)	Min	21,1253	–	57,1587	0,3149
		Max	102,2000		107,766	29,2680
		Mean	53,8759		94,4055	0,8761
		Std dev	11,0604		8,0473	1,0969
	F (Drift II)	Min	31,9157	–	–	0,6922
		Max	66,9203			0,8260
		Mean	50,3074			0,7596
		Std dev	7,6621			0,0373

Apêndice D – Tabela Suplementar 4: Resultado Estatística do poço 8-BUZ-21D-RJS

WELL	UNIT		Gamma-Ray (GAPI)	Density (g/cm^3)	P-Sonic (us/ft)	Resistivity (Ohm*m)
		Filter	Trimmed mean 25%			
8-BUZ-21D-RJS	B (Syn-Rift II)	Min	15,1071	2,4440	57,2634	2,1599
		Max	61,2642	2,5873	65,7402	128,0090
		Mean	30,7633	2,5147	60,8594	19,5669
		Std dev	9,5977	0,0318	1,9534	19,9986
	C (Post-Rift I)	Min	10,4345	2,3191	54,0686	2,4033
		Max	47,8234	2,6422	71,7955	1999,8200
		Mean	22,5383	2,5097	61,1077	546,1330
		Std dev	6,6570	0,0607	3,4170	438,4270
	D (Post-Rift II)	Min	12,0267	–	54,6236	24,2942
		Max	208,3670		86,4203	5000,0000
		Mean	43,9743		68,5435	3485,0600
		Std dev	25,2753		5,2359	1762,8000
	E (Drift I)	Min	17,4939	1,1994	52,6205	0,1869
		Max	211,291	2,9331	144,5510	306,3150
		Mean	57,9046	2,2736	103,0600	3,2133
		Std dev	16,6159	0,1761	17,1998	21,7453
	F (Drift II)	Min	19,1307	–	–	0,5174
		Max	69,9236			0,8181
		Mean	43,9771			0,6750
		Std dev	7,73162			0,0716

Apêndice E – Tabela Suplementar 5: Resultado Estatística do poço 8-BUZ-26-RJS

WELL	UNIT		Gamma-Ray (GAPI)	Density (g/cm^3)	P-Sonic (us/ft)	Resistivity (Ohm*m)
		Filter	Trimmed mean 25%			
8-BUZ-26-RJS	B (Syn-Rift II)	Min	10,2531	2,0610	49,2089	0,8813
		Max	139,2450	2,7068	120,3990	1950,0000
		Mean	40,5176	2,5707	63,3782	242,3430
		Std dev	27,4568	0,1059	13,5067	491,5050
	C (Post-Rift I)	Min	14,2835	2,4475	52,5857	1,9984
		Max	56,1826	2,6533	64,0834	1686,9000
		Mean	25,4519	2,5484	59,3479	246,4780
		Std dev	9,3281	0,0380	2,4758	371,2100
	D (Post-Rift II)	Min	9,5232	1,5235	51,1629	0,3729
		Max	115,3250	2,8991	154,1620	5000,0000
		Mean	22,8483	2,0644	69,1468	229,7120
		Std dev	15,1961	0,1978	7,1742	899,6120
	E (Drift I)	Min	12,8510	–	–	0,2805
		Max	89,3647			4995,3200
		Mean	58,7038			41,7514
		Std dev	14,2670			369,0810
	F (Drift II)	Min	19,0360	–	–	0,5182
		Max	77,8911			0,8816
		Mean	50,4954			0,7252
		Std dev	9,4441			0,0568

Apêndice F – Tabela Suplementar 6: Resultado Estatística do poço 8-BUZ-28DA-RJS

WELL	UNIT		Gamma-Ray (GAPI)	Density (g/cm^3)	P-Sonic (us/ft)	Resistivity (Ohm*m)
		Filter	Trimmed mean 25%			
8-BUZ-28DA-RJS	B (Syn-Rift II)	Min	11,9671	2,3262	51,9994	2,1018
		Max	79,0463	2,7069	67,5770	1768,3200
		Mean	30,0783	2,5324	58,0714	68,2834
		Std dev	16,2558	0,0852	3,0988	239,2160
	C (Post-Rift I)	Min	7,8321	2,2919	50,7231	5,4044
		Max	61,3053	2,8729	80,7780	10530,3000
		Mean	30,9742	2,4563	64,1751	1427,0200
		Std dev	11,5707	0,1191	6,6989	2225,7900
	D (Post-Rift II)	Min	13,6671	–	55,4099	1,2760
		Max	187,0090		94,6052	5012,4300
		Mean	26,2749		69,6966	2589,9900
		Std dev	19,8772		4,6870	1979,3900
	E (Drift I)	Min	23,9967	–	–	0,3434
		Max	96,1977			15,0740
		Mean	52,7258			0,8302
		Std dev	14,5655			1,0732
	F (Drift II)	Min	11,7301	–	–	0,6100
		Max	63,7462			0,9176
		Mean	41,0466			0,7489
		Std dev	8,5637			0,0560

Apêndice G – Tabela Suplementar 7: Resultado Estatística Geral dos poços 2-ANP-1-RJS, 3-BRSA-1053-RJS, 8-BUZ-20-RJS, 8-BUZ-21D-RJS, 8-BUZ-26-RJS e 8-BUZ-28DA-RJS

UNIT		Gamma-Ray (GAPI)	Density (g/cm3)	P-Sonic (us/ft)	Resistivity (Ohm*m)
B (Syn-Rift II)	Min	6.9 - 15.1	2.06 - 2.44	49.2 - 57.3	0.7- 7.1
	Max	61.3 - 139.2	2.59- 2.71	65.7 - 120.4	128.0 - 1950.0
	Mean	20.1 - 40.5	2.47 - 2.57	57.8 - 63.4	19.6 - 435.2
	Std dev	9.6- 27.5	0.03 - 0.11	2.0 - 13.5	20.0 - 491.5
C (Post-Rift I)	Min	0 - 14.3	2.10 - 2.45	48.7 - 54.1	0.9 - 64.1
	Max	41.2 - 61.3	2.64 - 2.87	64.1 - 80.8	1331.7 - 10530.3
	Mean	17.8 - 30.9	2.46 - 2.59	57.1 - 64.2	246.5 - 1427.0
	Std dev	5.4 - 11.7	0.04 - 0.12	2.5 - 6.7	246.0 - 2225.8
D (Post-Rift II)	Min	0 - 13.7	1.52 - 1.62	51.2 - 55.4	0.9 - 24.3
	Max	108.4 - 208.4	2.90 - 4.63	86.4 - 154.2	5000.0 - 5012.4
	Mean	14.6 - 44.0	2.06 - 2.17	67.7 - 69.9	1.8 - 2590.0
	Std dev	10.7 - 25.3	0.20 - 0.50	3.4 - 7.2	899.6- 1979.4
E (Drift I)	Min	10.0 - 24.0	1.20 - 1.88	52.6 - 57.2	0.2 - 0.3
	Max	64.0 - 211.3	2.93- 2.96	107.8- 160.0	15.1 - 4995.3
	Mean	43.4 - 58.7	2.27 - 2.37	99.3 - 125.1	0.88 - 41.8
	Std dev	9.0 - 16.6	0.18 - 0.19	8.0 - 20.1	1.1 - 369.1
F (Drift II)	Min	11.7 - 31.9	–	–	0.5 - 0.7
	Max	57.9 - 77.9			0.8 - 0.9
	Mean	38.6 - 50.5			0.7 - 0.8
	Std dev	7.7 - 12.3			0 - 0.1

ANEXOS

ANEXO A – POÇO 1-BRSA-137-RJS

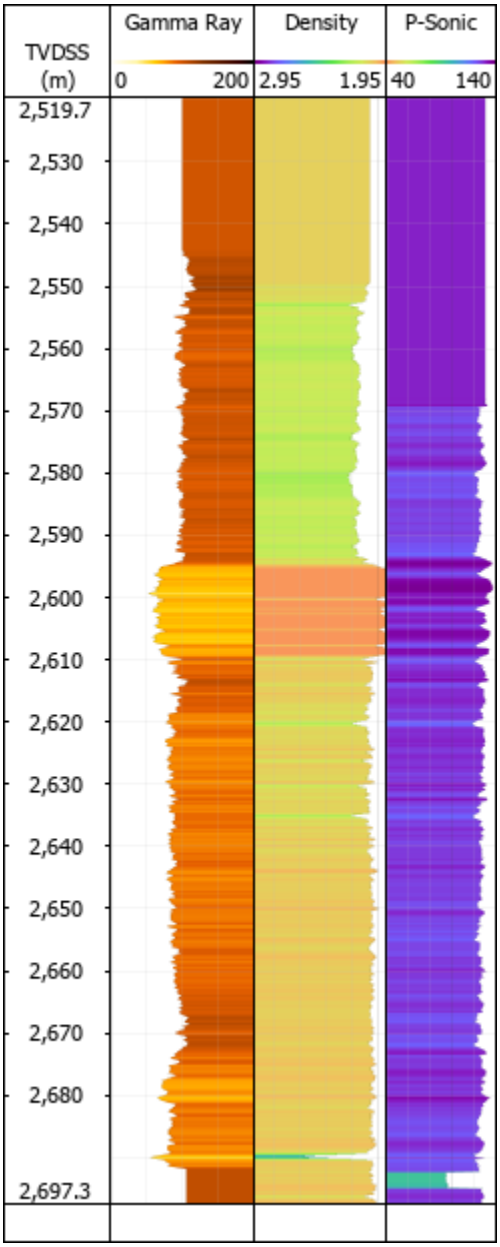

ANEXO B – POÇO 2-ANP-1-RJS

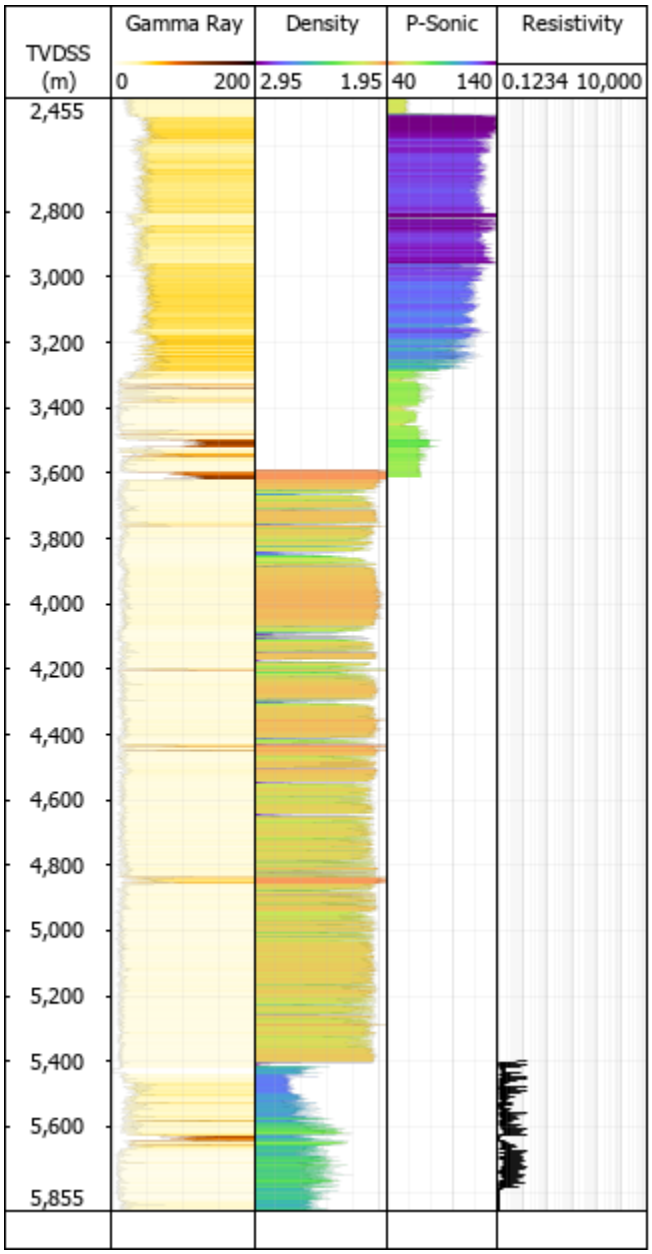

ANEXO C – POÇO 3-BRSA-944A-RJS

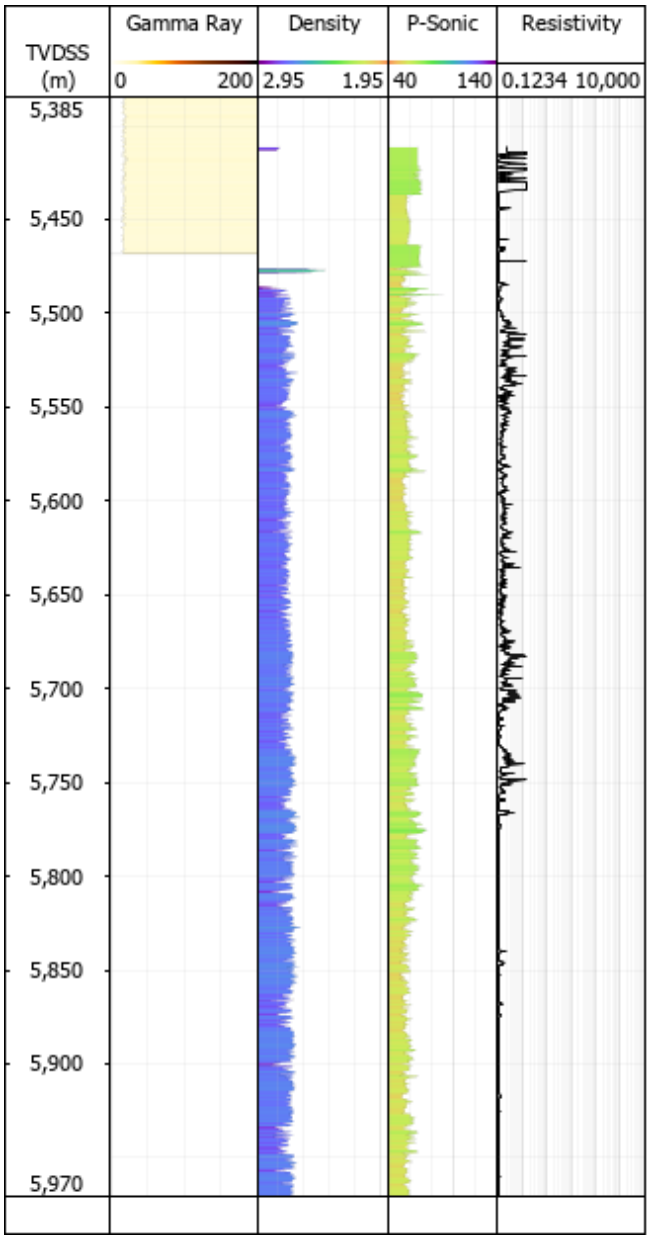

ANEXO D – POÇO 3-BRSA-1053-RJS

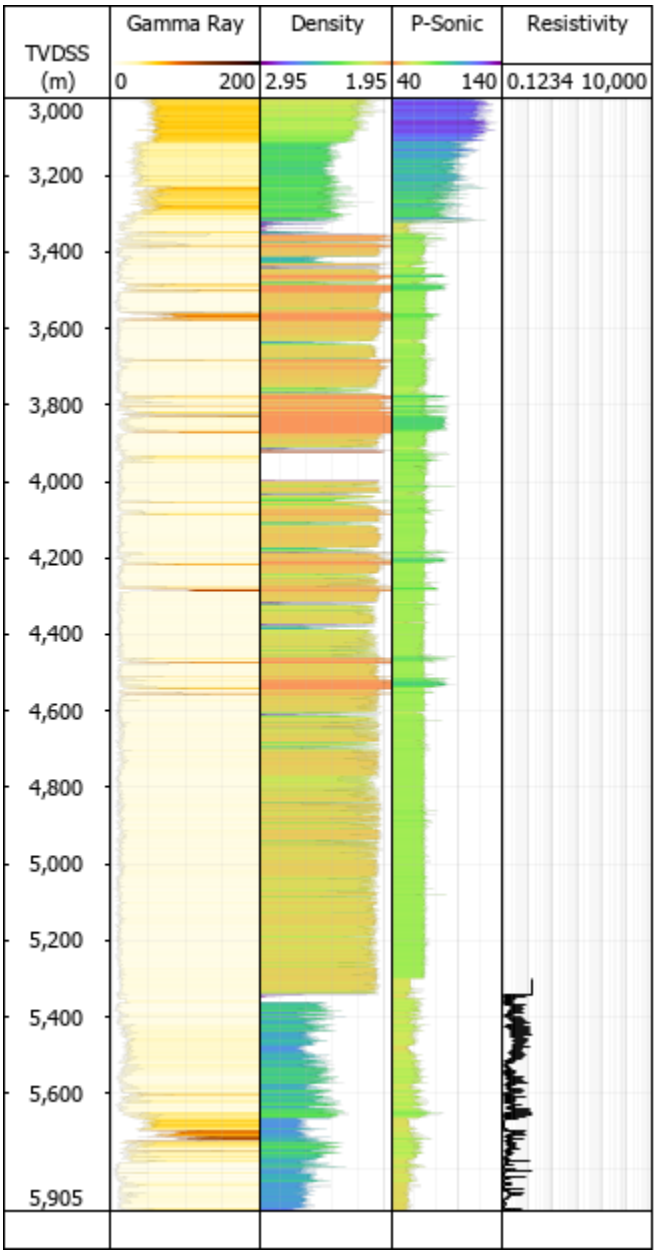

ANEXO E – POÇO 3-BRSA-1064-RJS

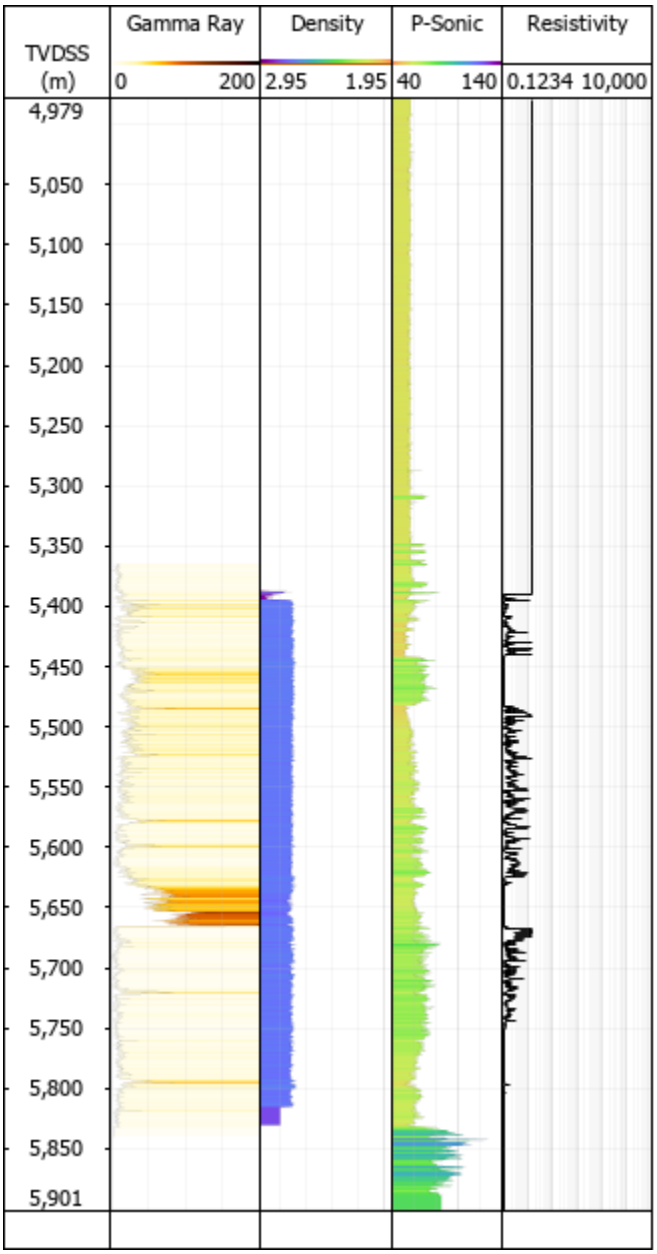

ANEXO F – POÇO 3-BRSA-1184-RJS

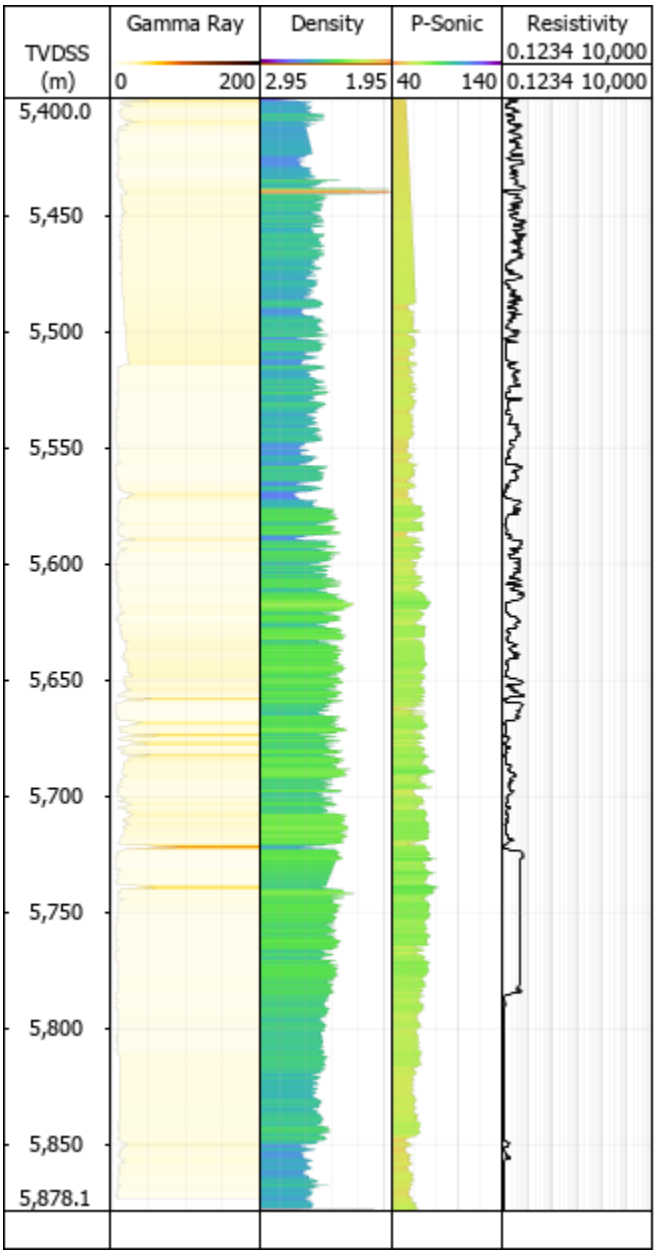

ANEXO G – POÇO 3-BRSA-1195-RJS

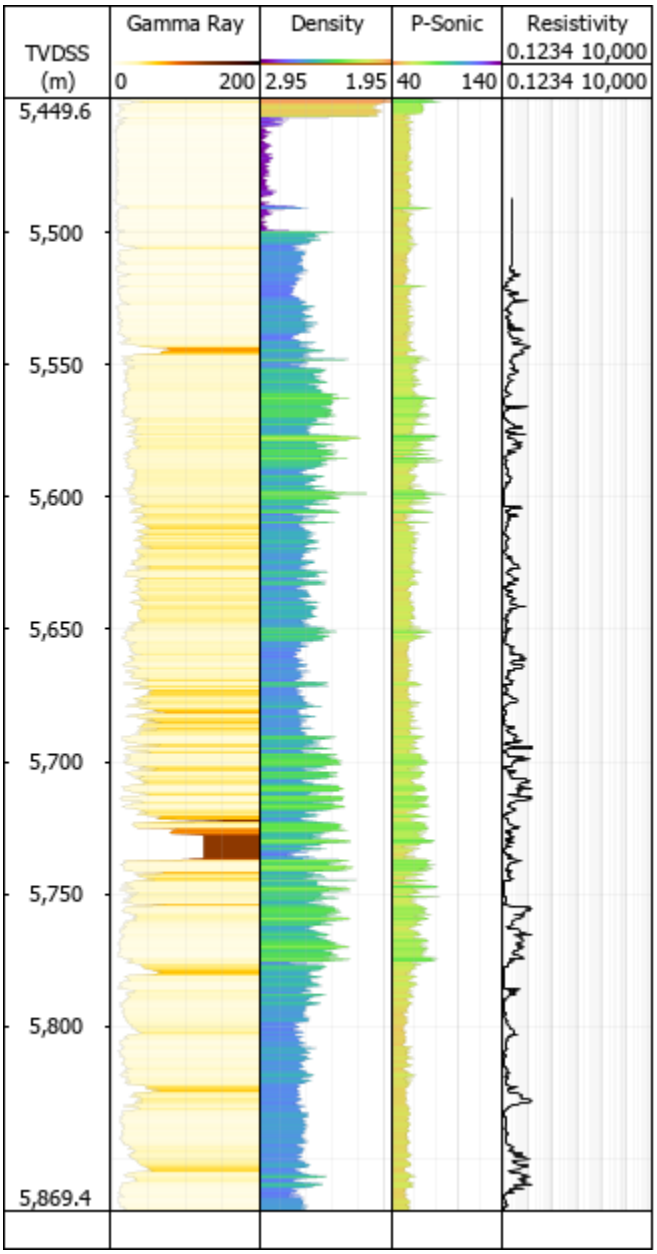

ANEXO H – POÇO 7-BUZ-6-RJS

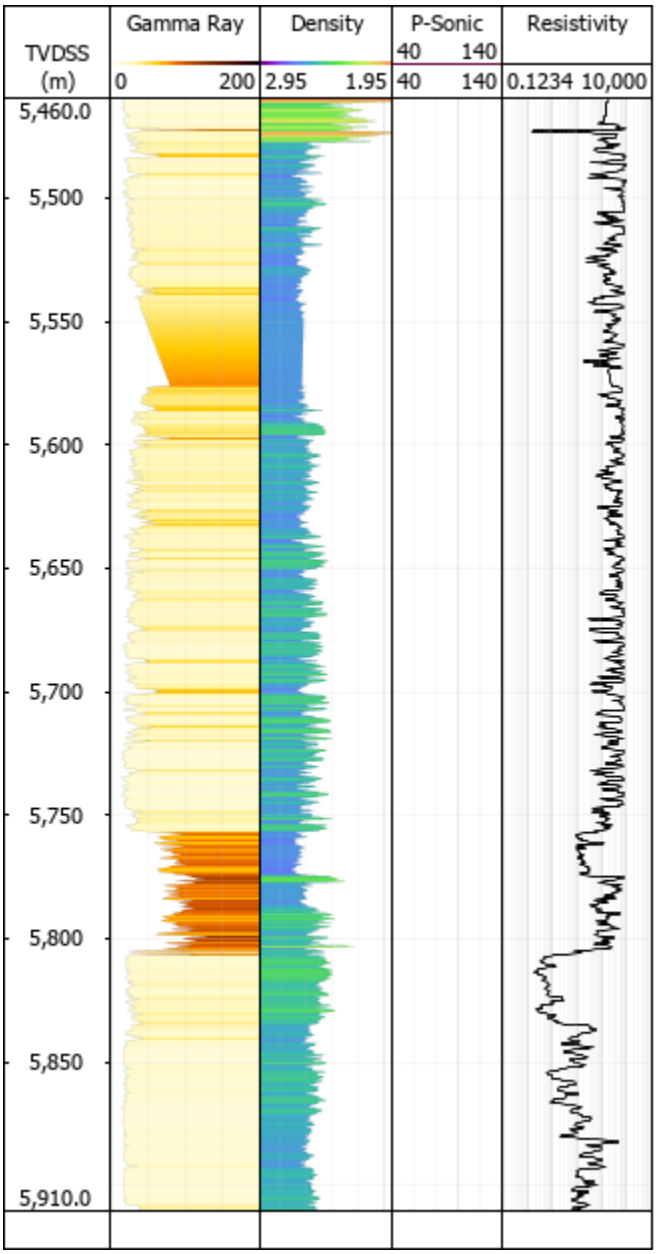

ANEXO I – POÇO 7-BUZ-10-RJS

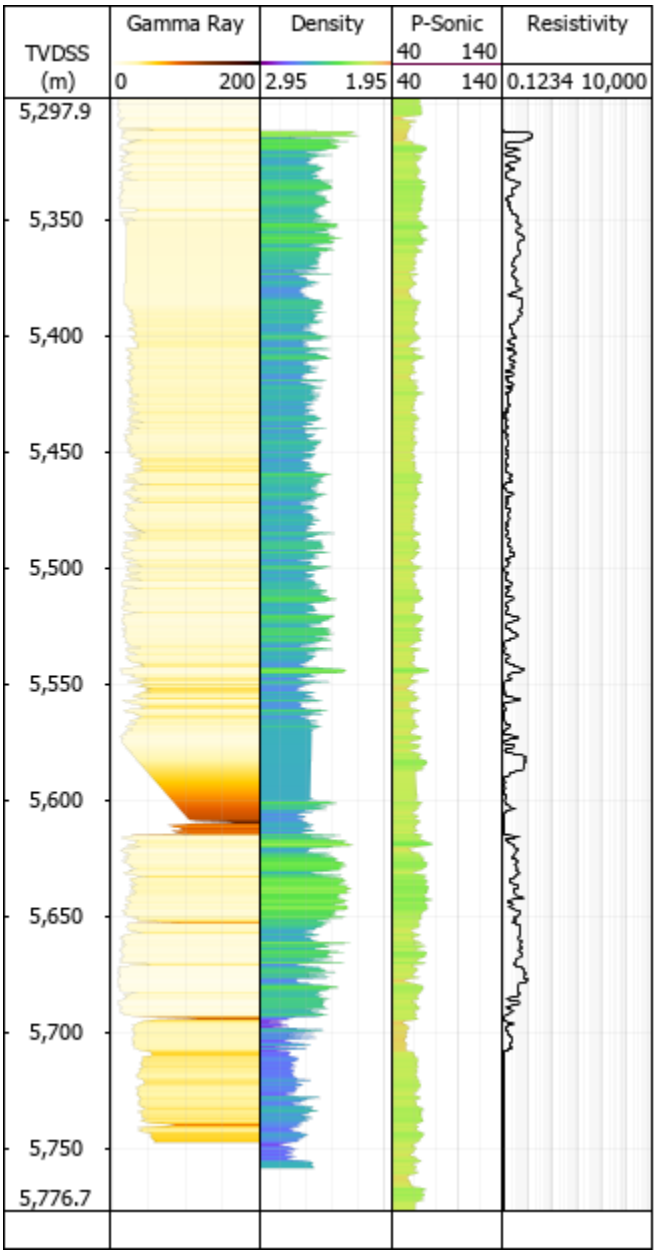

ANEXO J – POÇO 7-BUZ-12-RJS

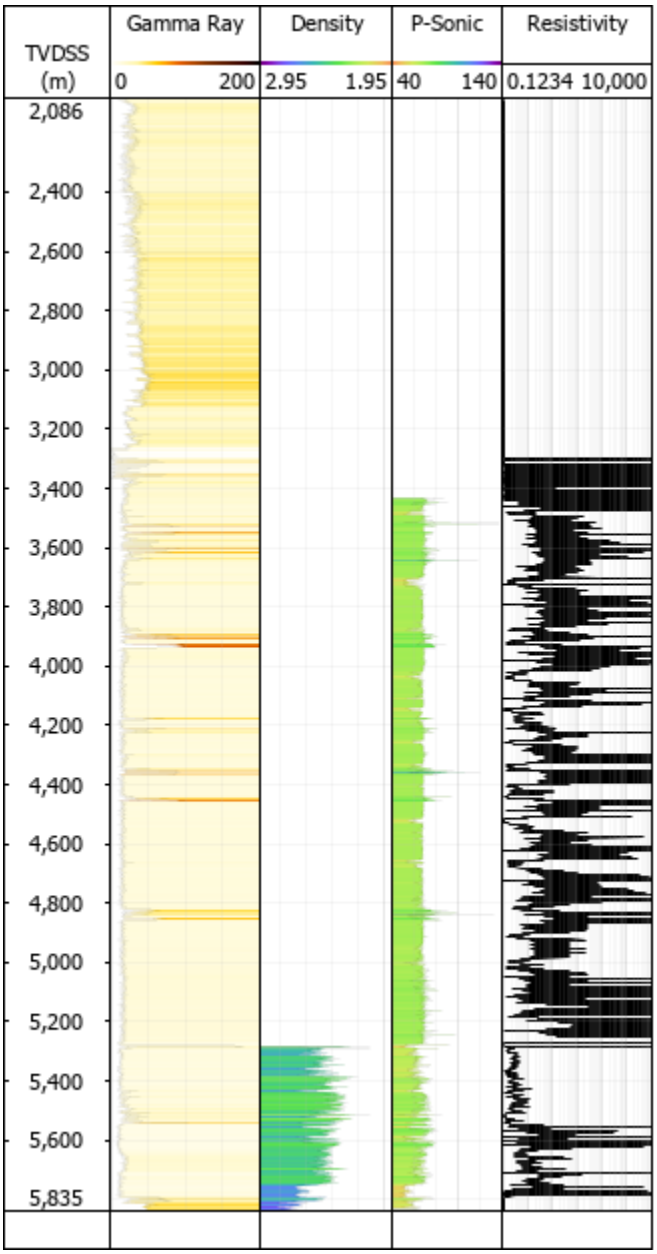

ANEXO K – POÇO 7-BUZ-13DA-RJS

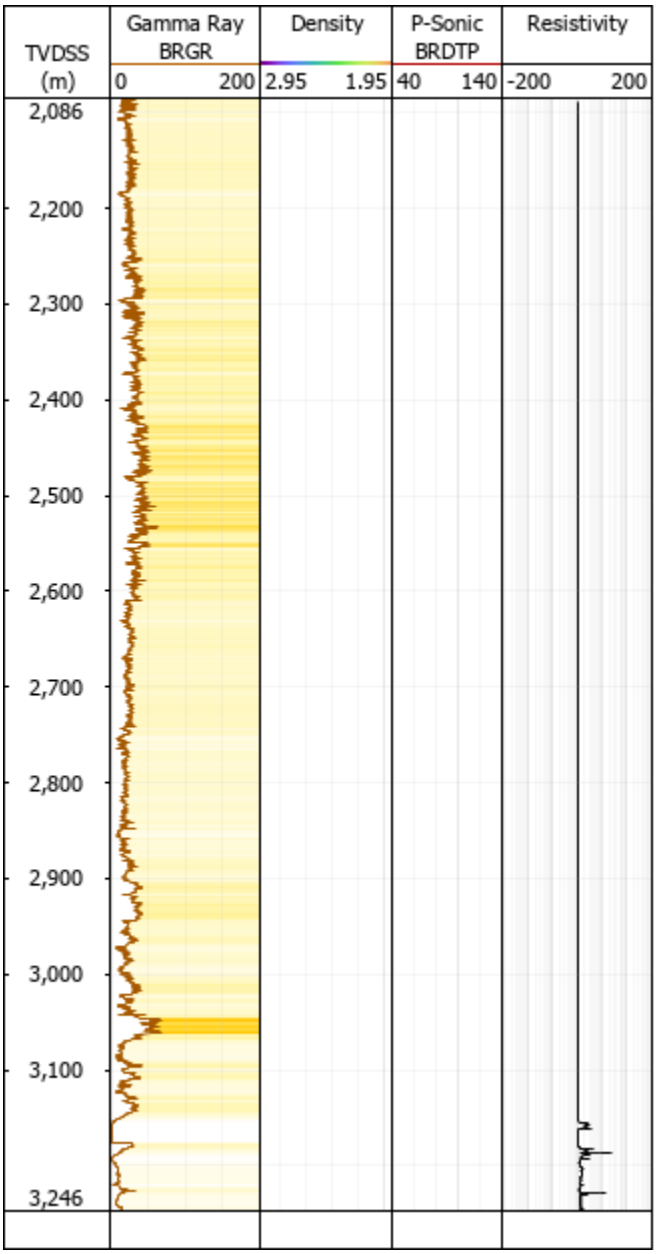

ANEXO L – POÇO 7-BUZ-14DA-RJS

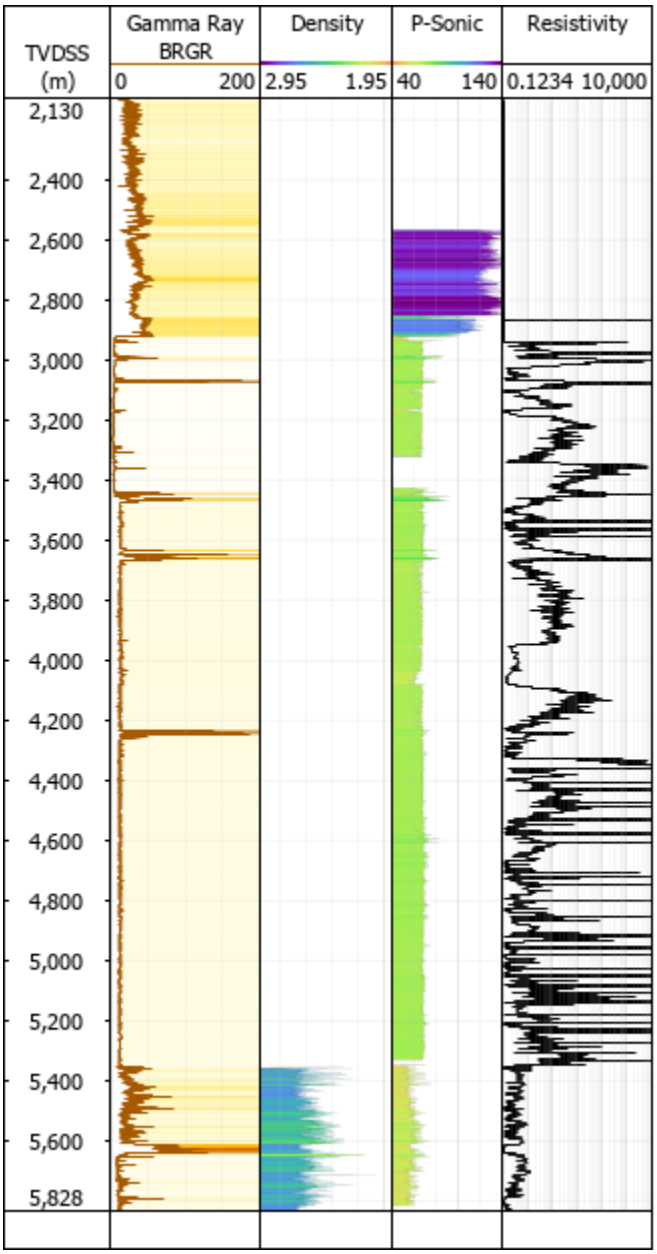

ANEXO M – POÇO 7-BUZ-14-RJS

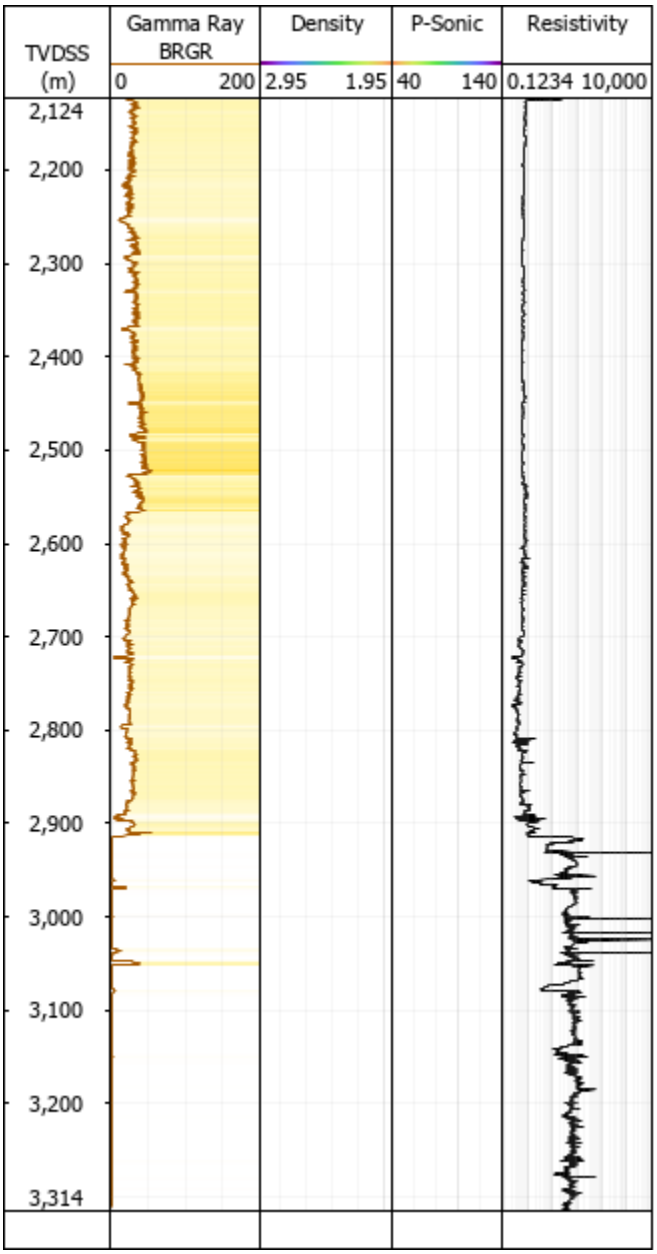

ANEXO N – POÇO 7-BUZ-17-RJS

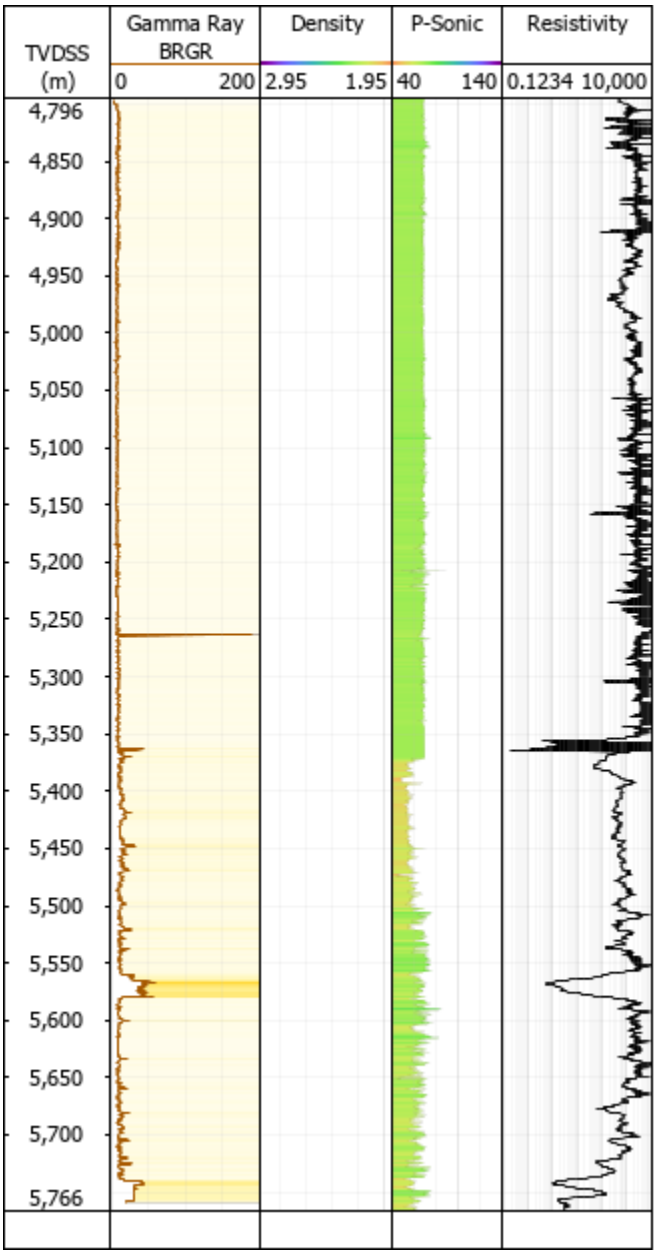

ANEXO O – POÇO 7-BUZ-23-RJS

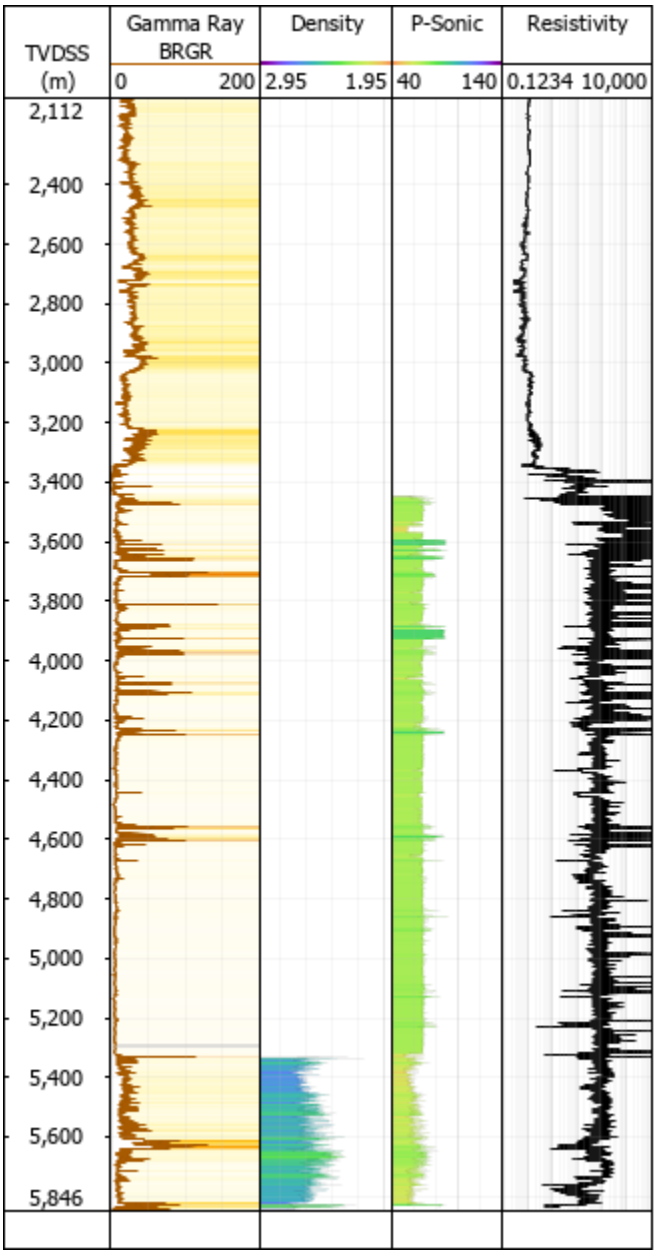

ANEXO P – POÇO 7-BUZ-25-RJS

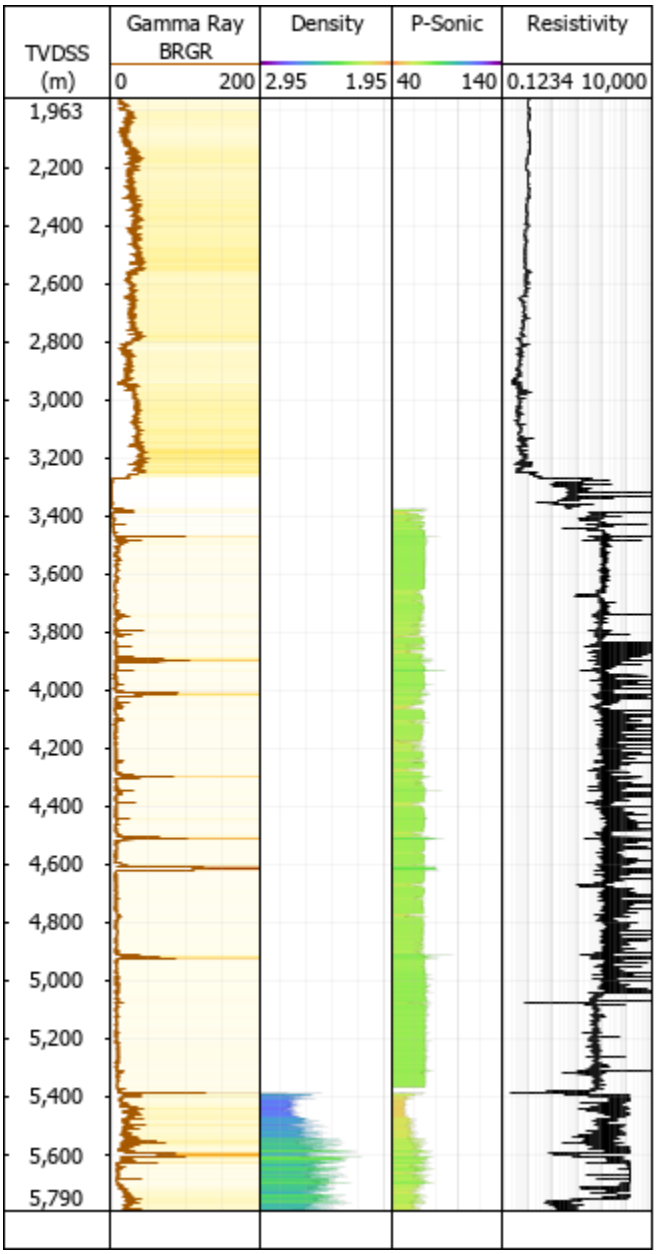

ANEXO Q – POÇO 7-BUZ-29D-RJS

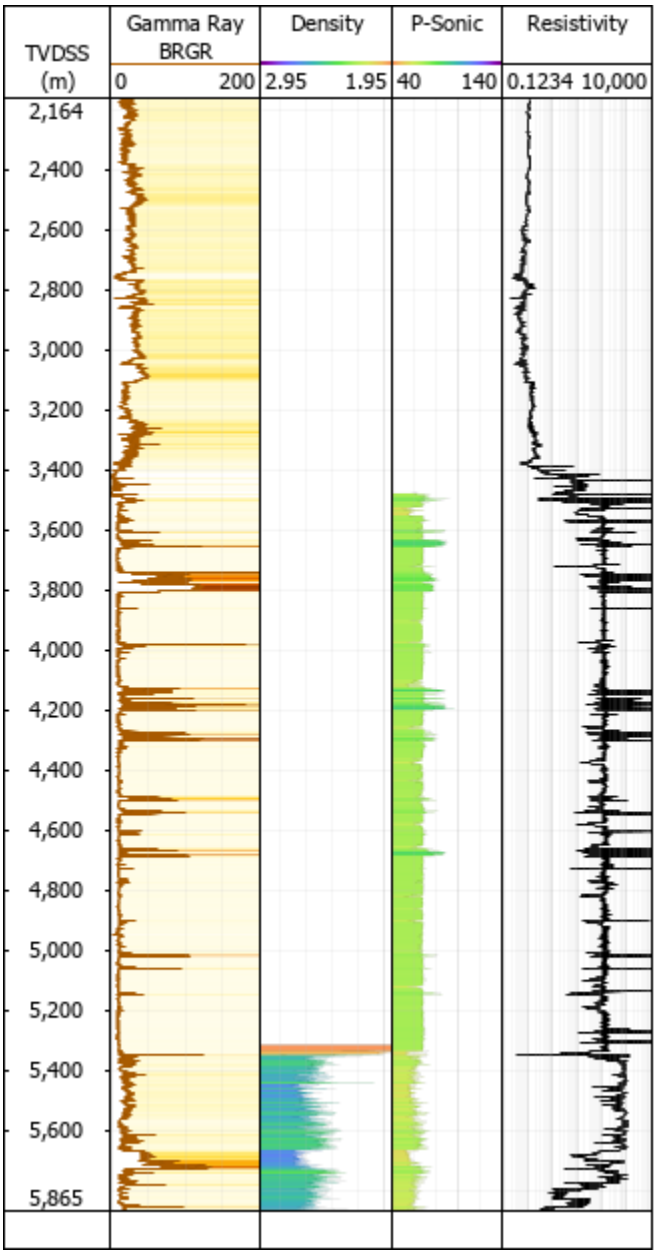

ANEXO R – POÇO 7-BUZ-30-RJS

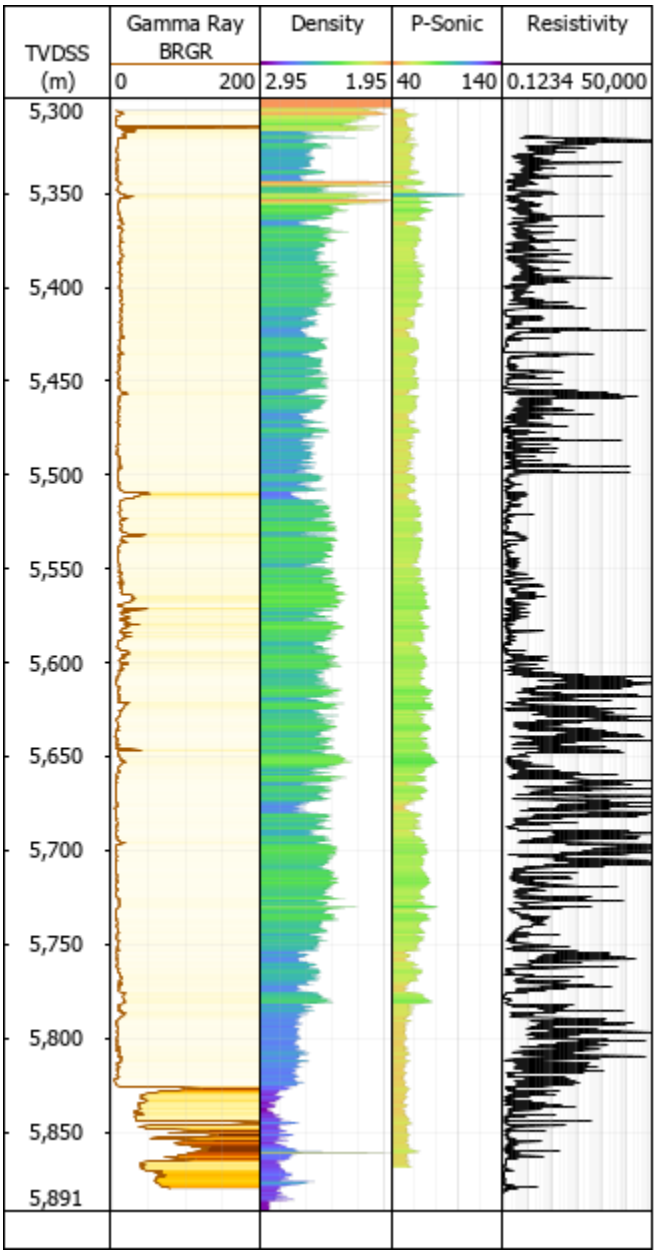

ANEXO S – POÇO 7-BUZ-31D-RJS

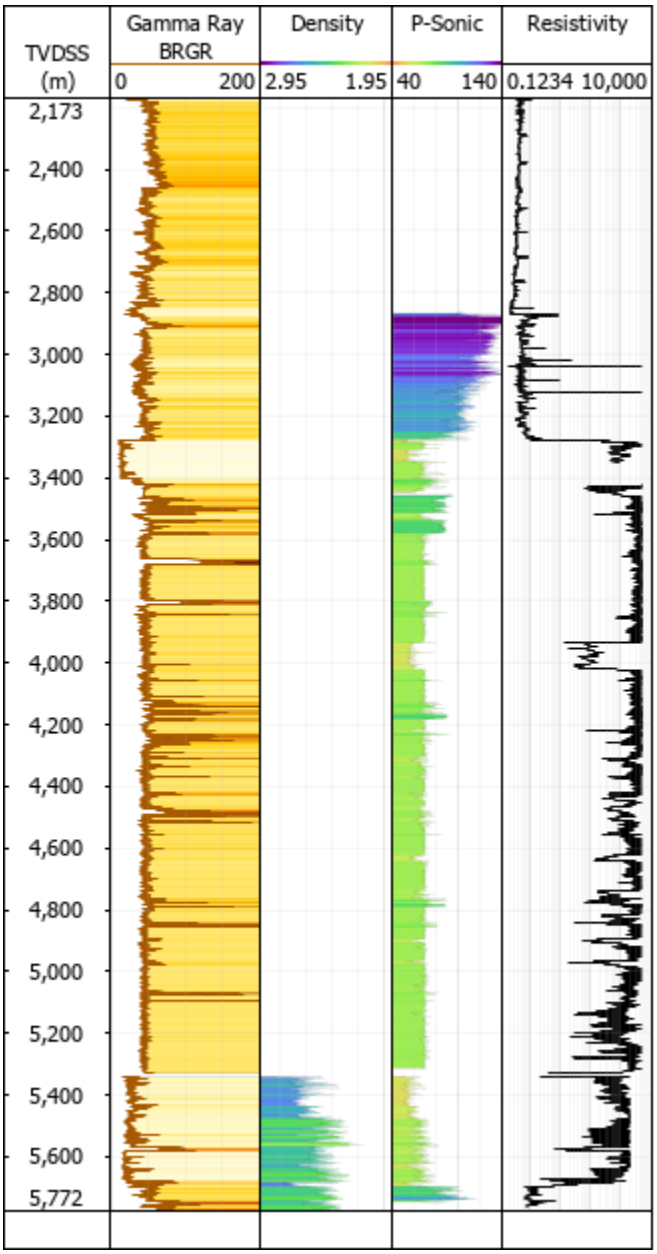

ANEXO T – POÇO 8-BUZ-5-RJS

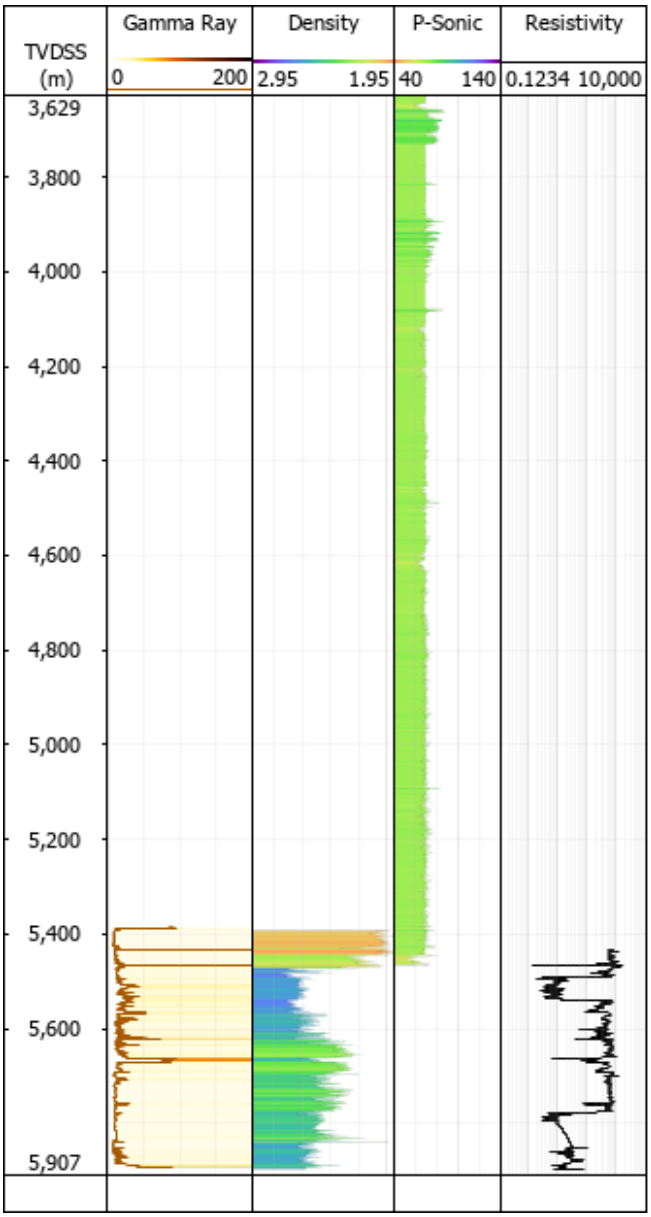

ANEXO U – POÇO 8-BUZ-9-RJS

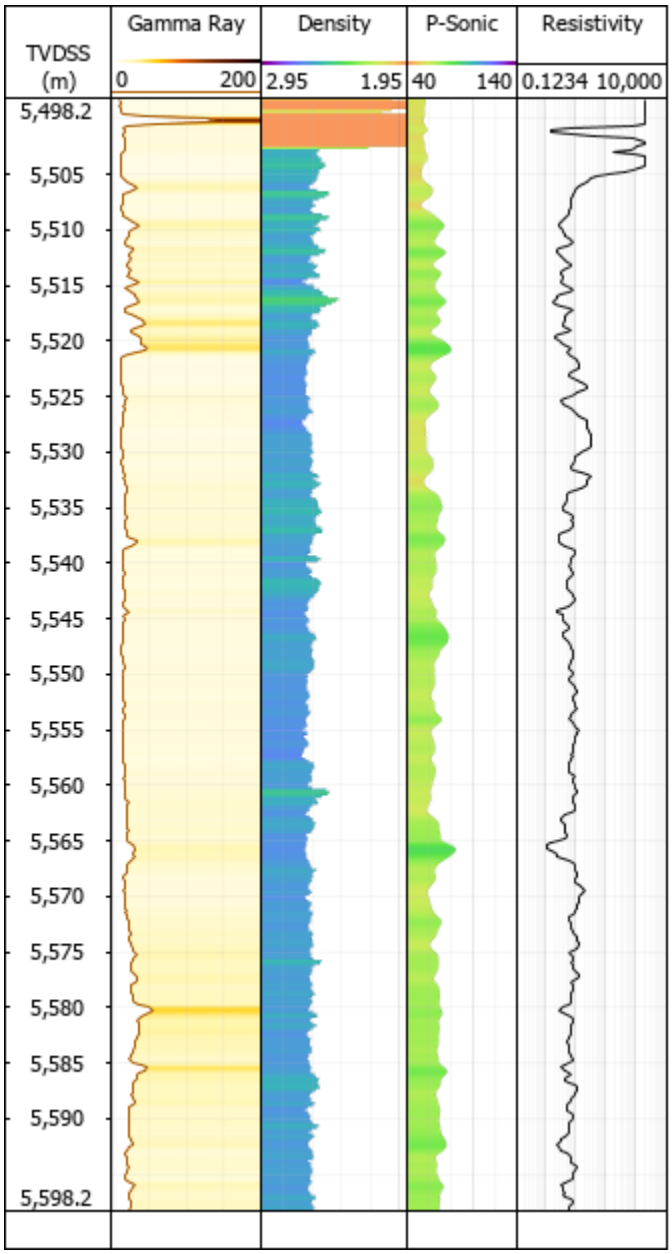

ANEXO V – POÇO 8-BUZ-15-RJS

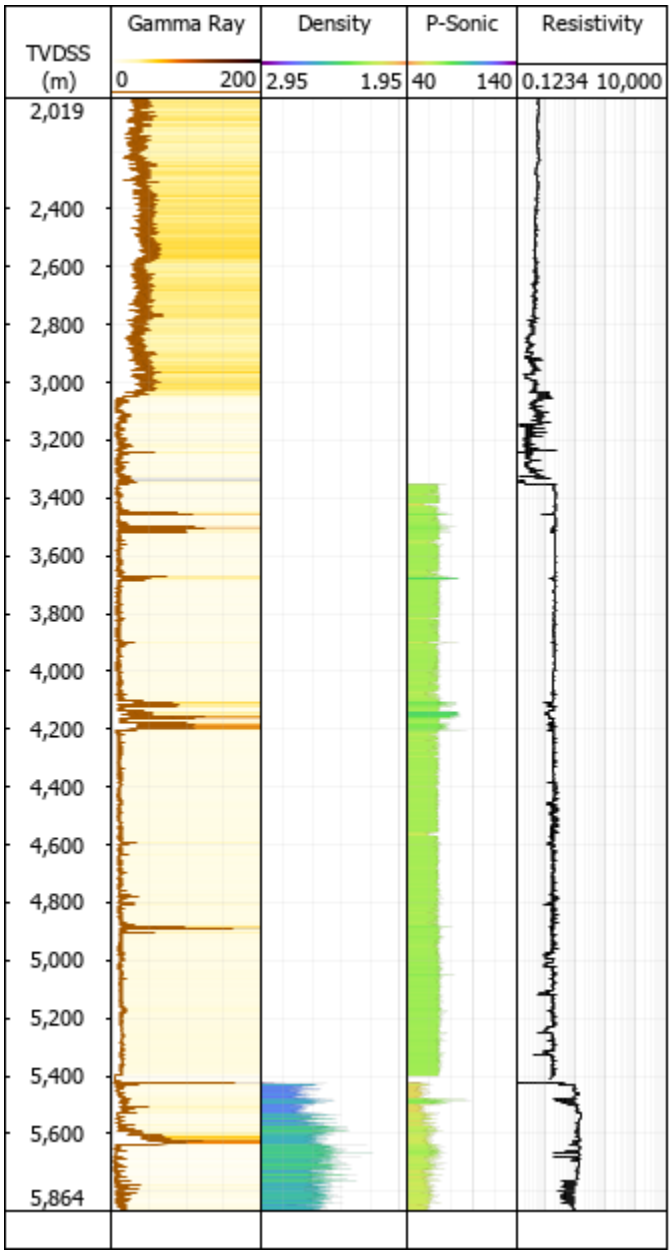

ANEXO X – POÇO 8-BUZ-20-RJS

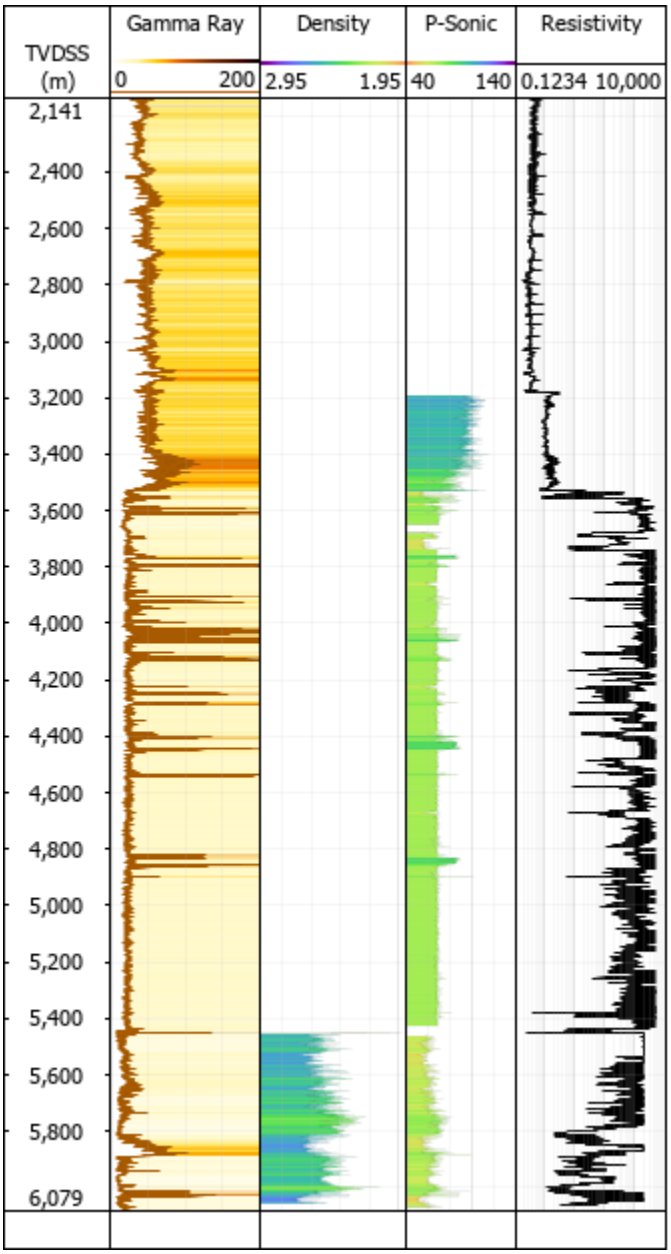

ANEXO W – POÇO 8-BUZ-21D-RJS

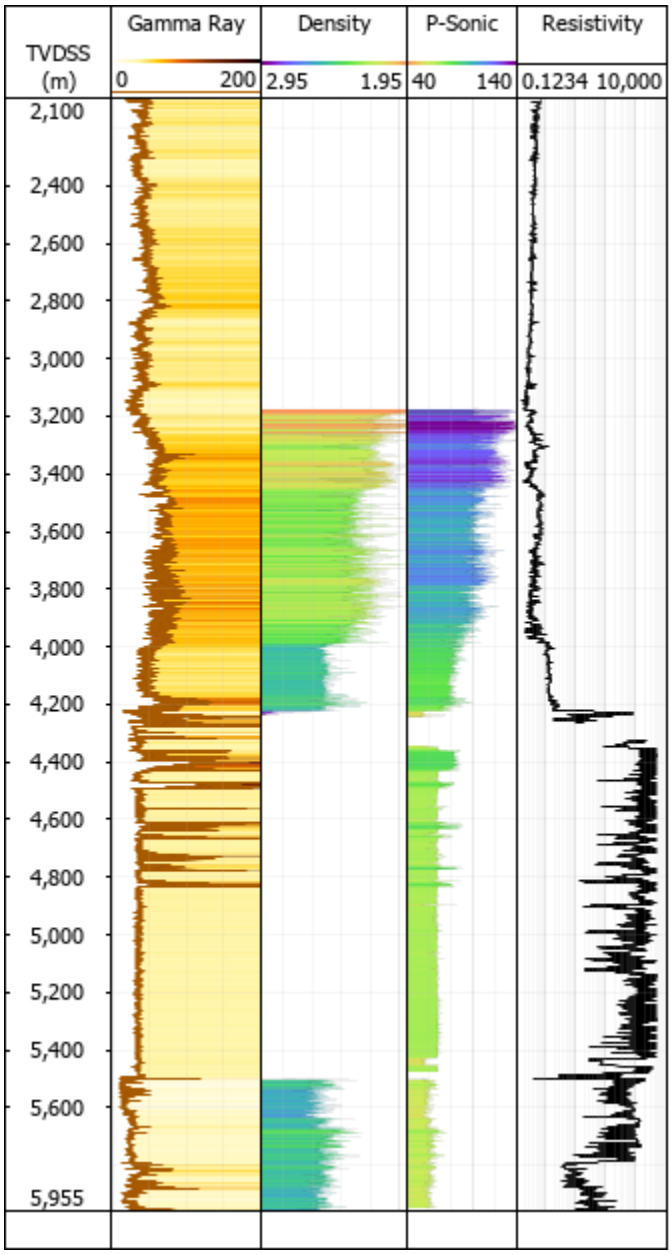

ANEXO Y– POÇO 8-BUZ-22D-RJS

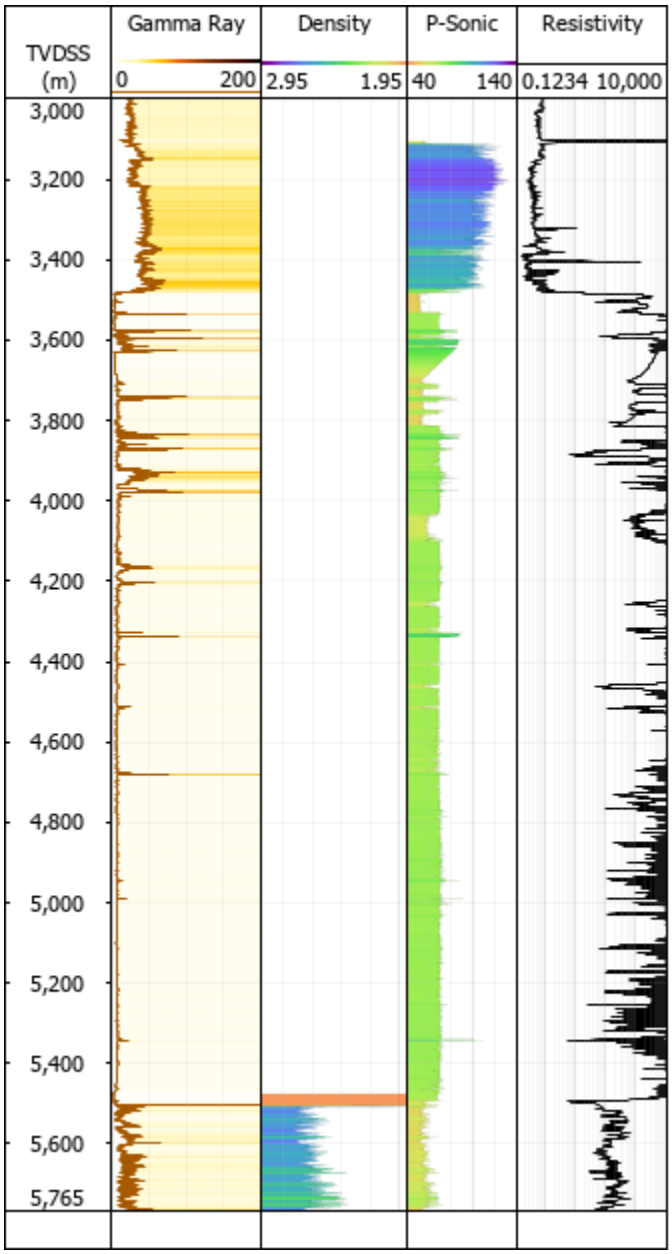

ANEXO Z – POÇO 8-BUZ-26-RJS

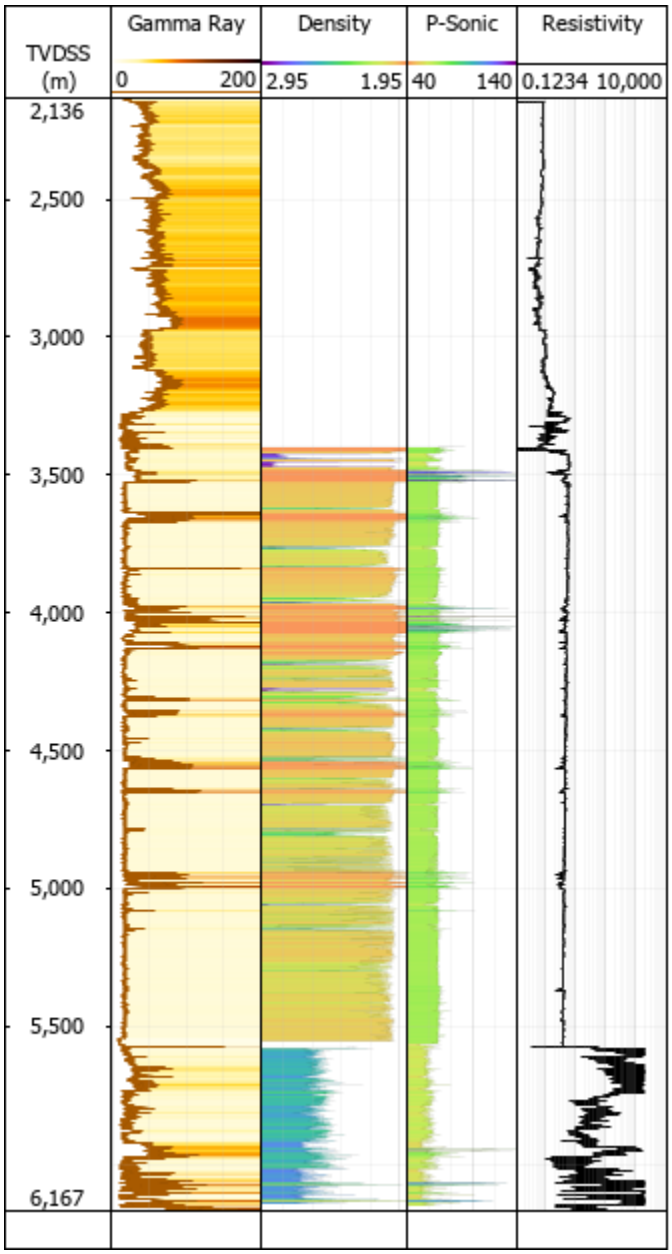

ANEXO AA – POÇO 8-BUZ-27D-RJS

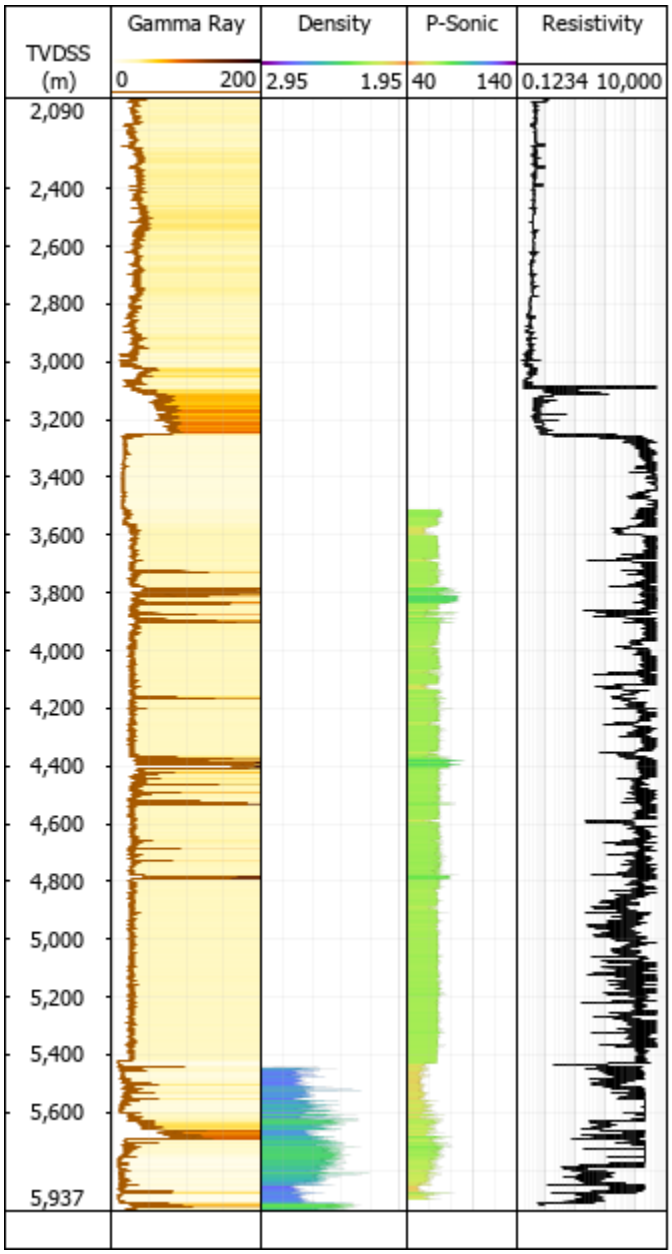

ANEXO BB – POÇO 8-BUZ-28DA-RJS

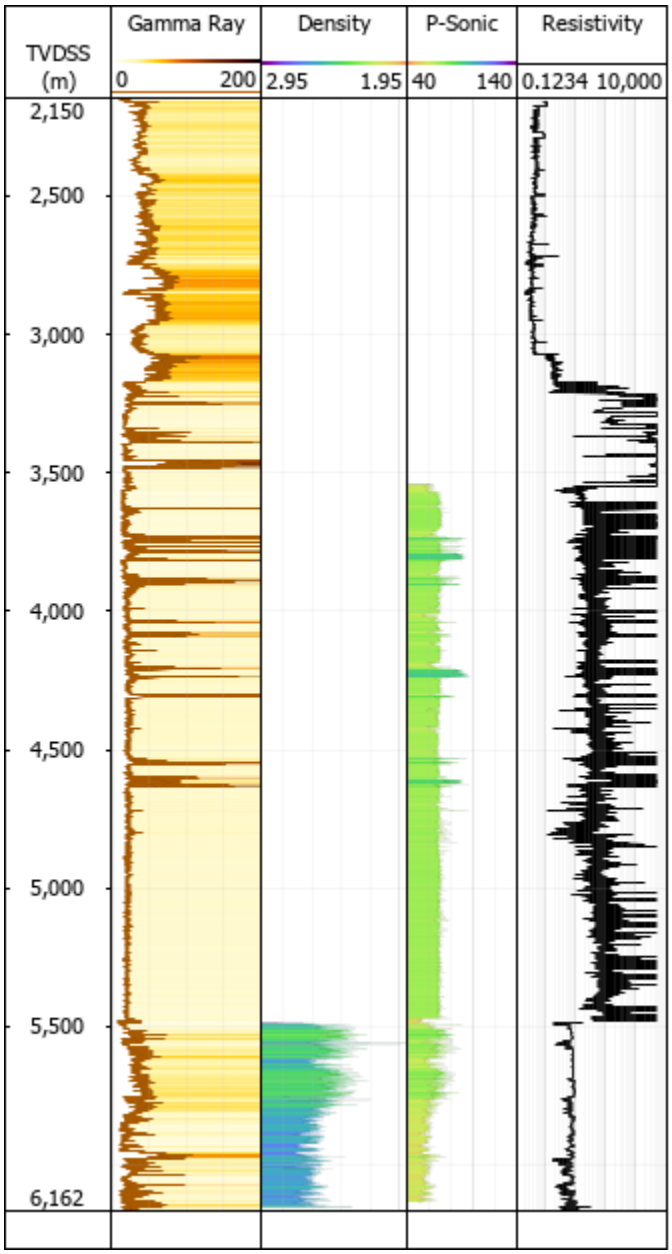

ANEXO CC – POÇO 8-BUZ-28D-RJS

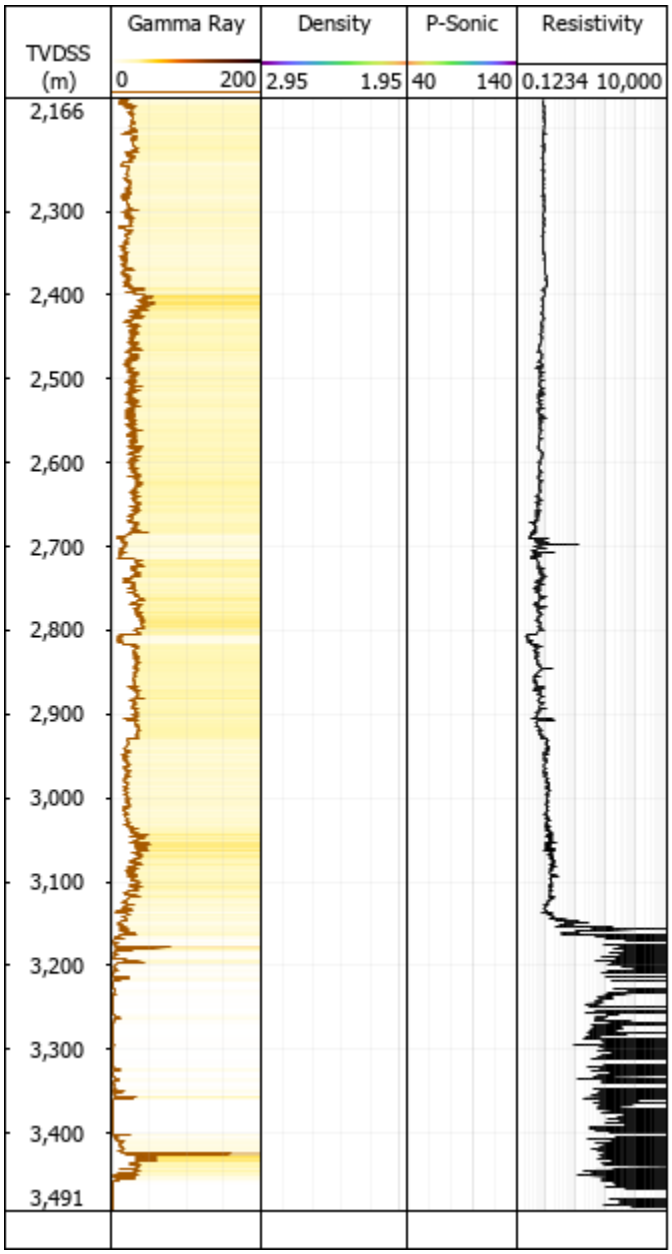

ANEXO DD – POÇO 8-BUZ-32DA-RJS

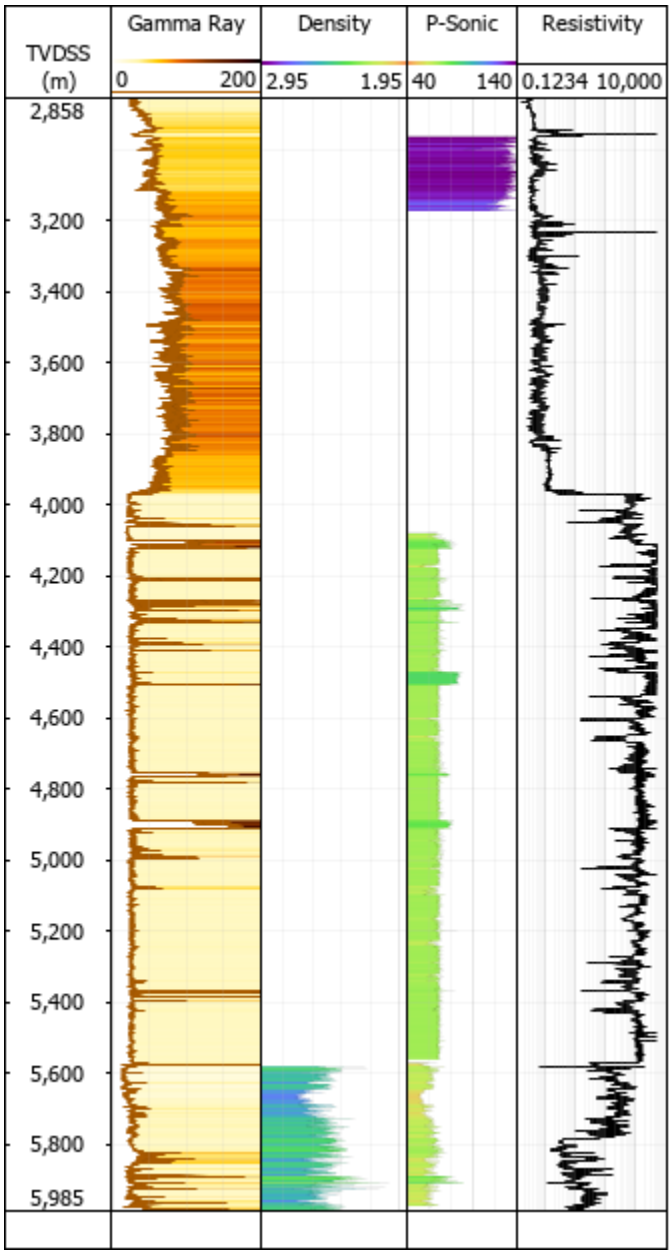

ANEXO EE – POÇO 8-BUZ-32D-RJS

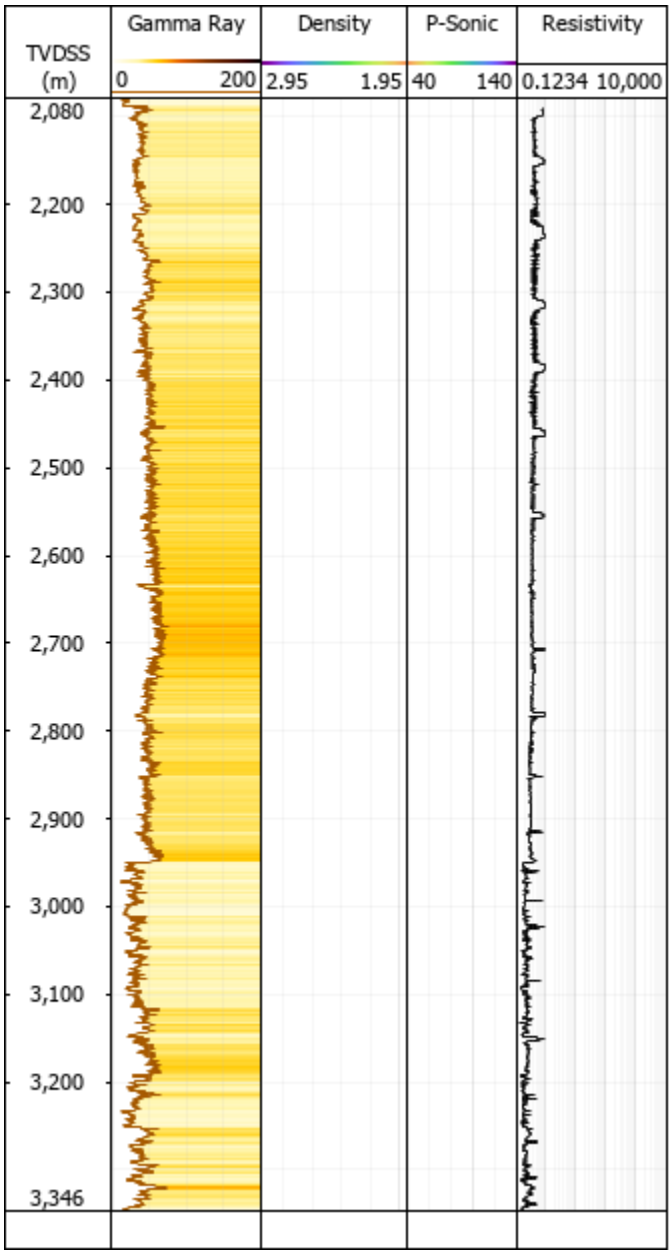

ANEXO FF – POÇO 9-BRSA-1159-RJS

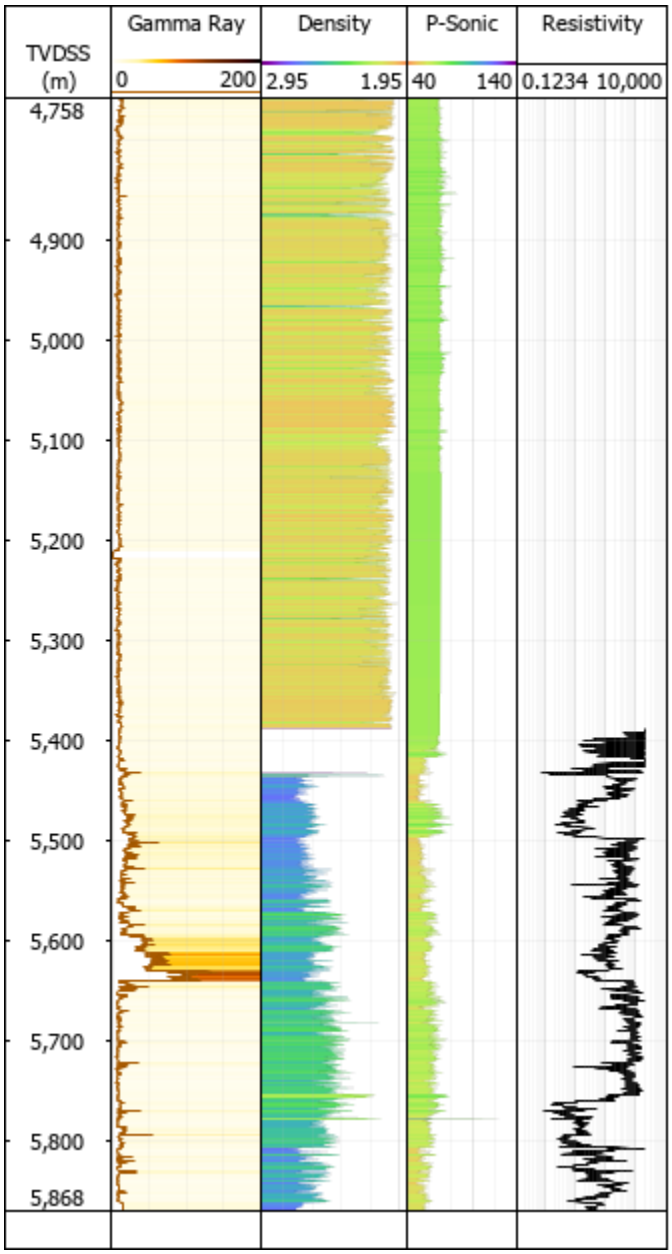

ANEXO GG – POÇO 9-BRSA-1191-RJS

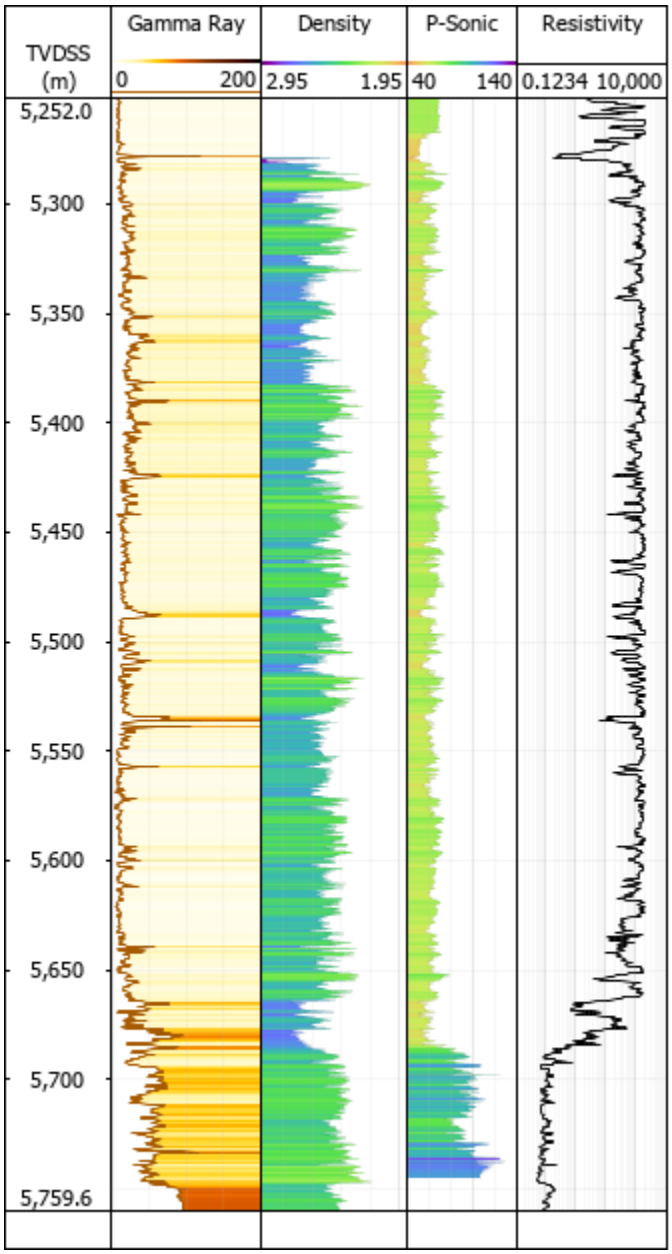

ANEXO HH – POÇO 9-BRSA-1197-RJS

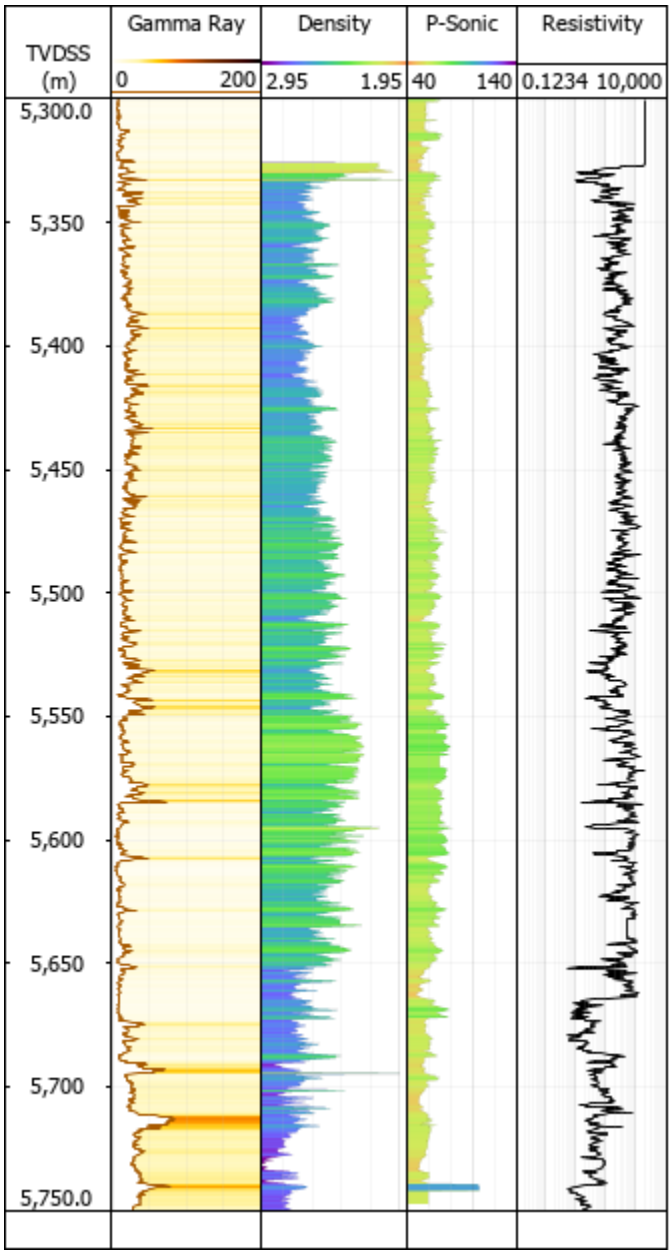

ANEXO II – POÇO 9-BUZ-1-RJS

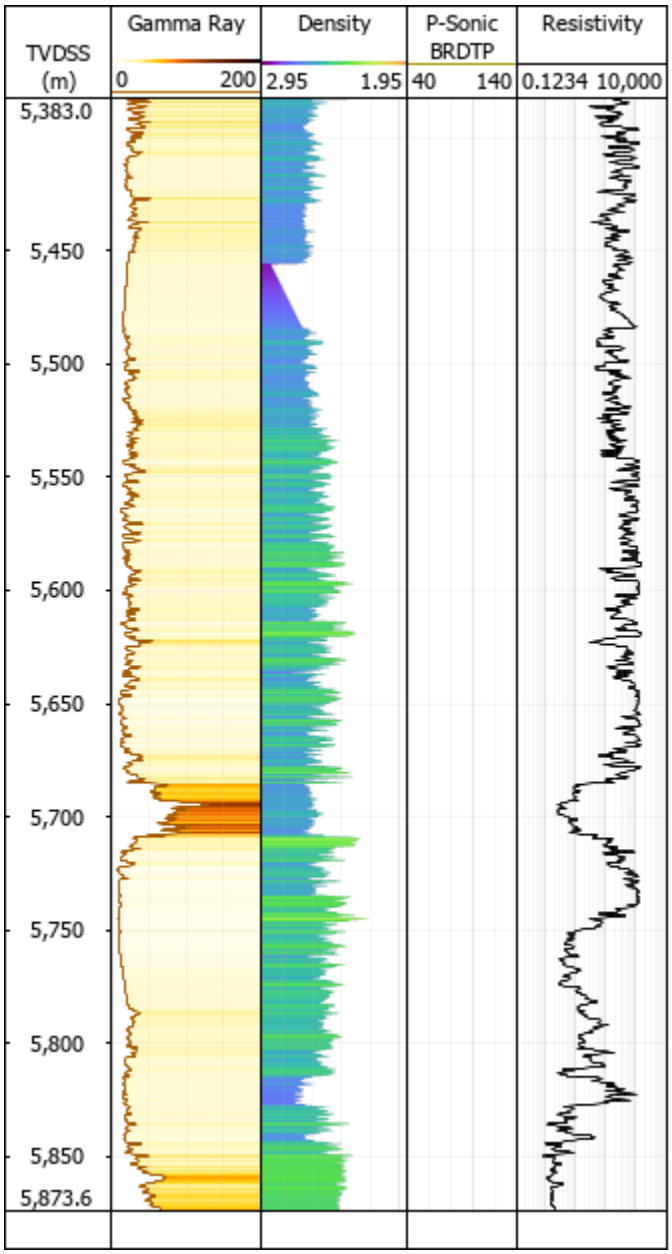

ANEXO JJ – POÇO 9-BUZ-2-RJS

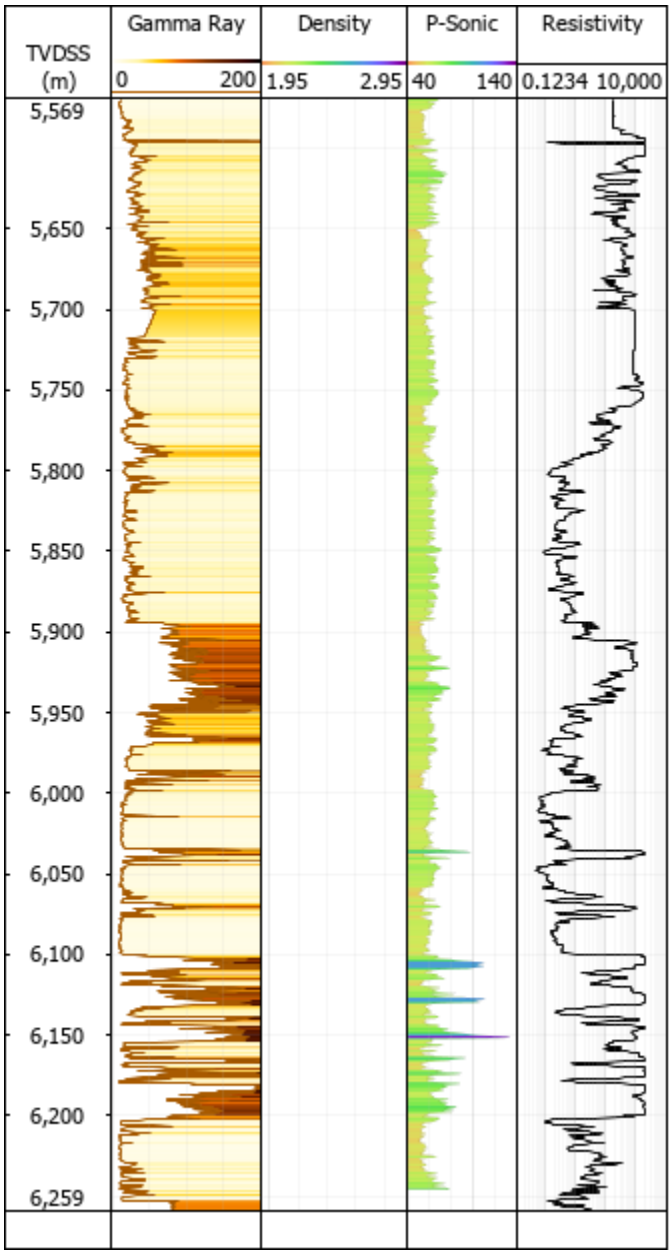

ANEXO KK – POÇO 9-BUZ-3-RJS

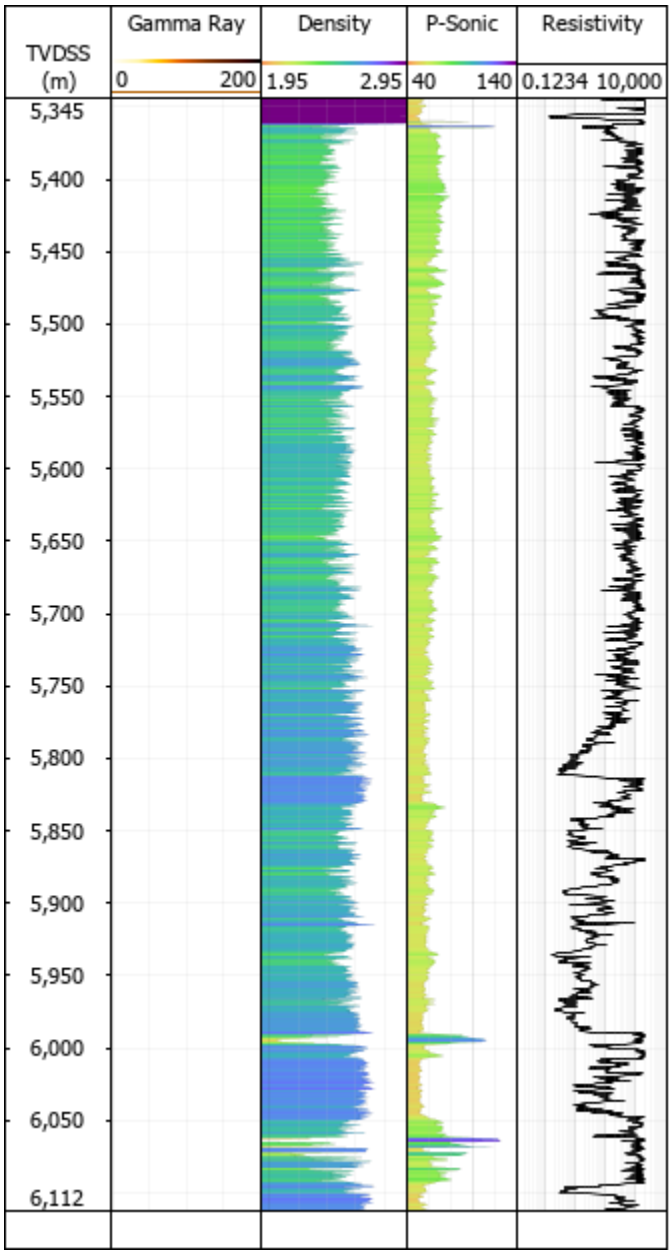

ANEXO LL – POÇO 9-BUZ-4-RJS

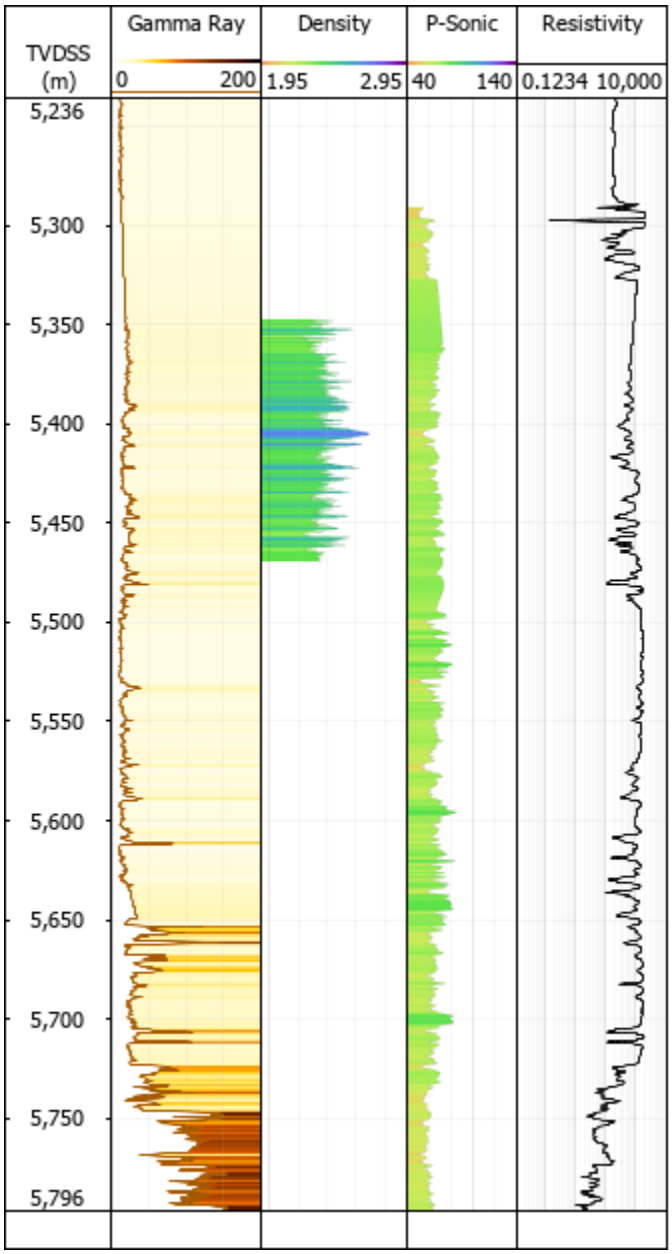

ANEXO MM – POÇO 9-BUZ-7-RJS

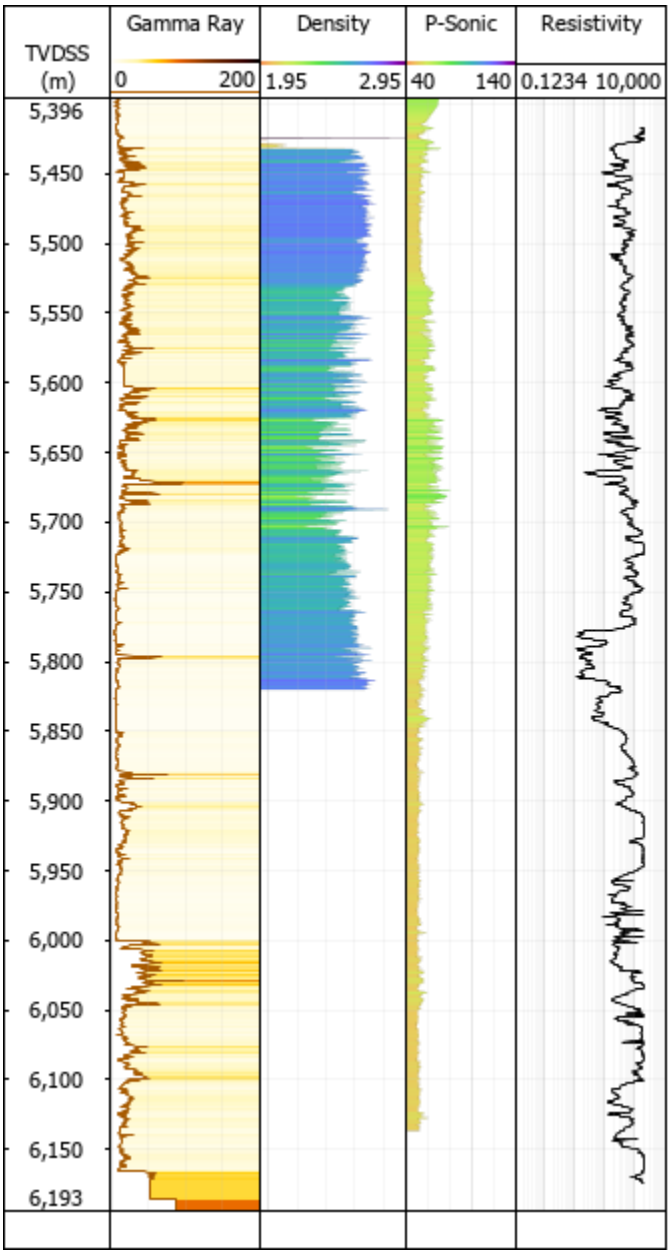

ANEXO NN– POÇO 9-BUZ-8-RJS